R

RADIOACTIVE ISOTOPES, THEIR DECAY IN MANTLE AND CORE

Introduction

The Earth is a thermal engine driven largely by heat produced from the decay of naturally occurring radioactive isotopes in its interior. At present, the main radioactive isotopes are ^{40}K, ^{235}U, ^{238}U, and ^{232}Th, whose atomic percentages, radioactive decay constants, half-life, and the heat production characteristics are given in Table R1. ^{26}Al, an extinct radioactive isotope may have been an important heat source in the early history of the Earth. Many other radioactive isotopes are also present in the Earth but they play a negligible role in heat production, either because of their low abundance or their low heat producing capacity.

The abundances of K, U, and Th in common rocks from the crust and some upper mantle materials are available from direct measurements. The compilation by Van Schmus (1995) lists their abundances and also shows some primitive mantle (present mantle + crust) estimates. Since then, new estimates of these elements in the primitive mantle (bulk silicate Earth—BSE) and the Earth have appeared, as also new experimental and theoretical studies bearing on radioactivity in the core.

Radioactivity of the mantle

Direct measurements of the radioactivity of rocks from the mantle are limited to its outermost layers just a few hundred kilometers deep in the upper mantle. Much of the lower mantle is not accessible for direct measurements and geophysical parameters such as seismic velocities and mineral physics data cannot provide strong constraints to its composition (Mattern *et al*., 2005). Current estimates of the abundances of K, U, and Th in BSE, and the Earth as a whole, are derived from several geochemical models. These combine cosmochemical considerations and composition of meteorites with some coherent trace element ratios observed in upper mantle samples and meteorites. The composition of volatile-rich C1 carbonaceous chondrites (a primitive class of meteorites with elemental abundances that closely match the composition of the solar photosphere) is used as a reference to compare the terrestrial abundances and deduce chemical fractionation patterns in the Earth (C1 models). The most comprehensive modeling of this type by McDonough and Sun (1995) provides a complete description of the methods and references to prior work. The abundance data of K, U, and Th in the primitive mantle from some of these studies (Table R2) are now included in the GERM database (GERM-A Geochemical Earth Reference Model at http://earthref.org/GERM/index.html). Implicit in these models is the assumption that the lower mantle is compositionally similar to the upper mantle and that the Fe-metallic core of the Earth has no radioactivity. Whether or not the mantle is compositionally layered is still unresolved (see for example, Anderson, 1989a,b). The K/U ratio in rocks from the crust and upper mantle is $\sim 1 \times 10^4$ but in chondrite meteorites is $\sim 8 \times 10^4$ (see Lassiter, 2004 for an up-to-date discussion of K/U ratios in terrestrial materials and meteorites). In the geochemical models, the low K/U ratio in the Earth, and the estimated low K abundance in the Earth relative to meteorites is attributed to the loss of moderately volatile K from the Earth.

Some recent experiments have raised questions about the C1-chondrite comparisons and the postulated loss due to volatility. Oxygen, the most abundant major element in the Earth (>30% by mass) has a different isotopic composition from that in carbonaceous and ordinary chondrites (Clayton, 1993) casting doubt on their suitability for the precursor Earth material. The identical K isotopic composition of terrestrial and meteoritic material indicates that the loss of K could not be due to partial vaporization from the Earth but must have preceded the process of planetary formation (Humayun and Clayton, 1995). Furthermore, C1 meteorites cannot provide for the ~30% Fe abundance in the Earth (Javoy, 1995).

Table R1 Important heat producing radioactive isotopes in the Earth: their decay constants, half-lives and heat production values (Van Schmus, 1995)

Isotope	Atomic percentage	Decay constant, λ (yr^{-1})	Half-life (yr)	Specific isotopic heat production ($\mu W kg^{-1}$)
^{40}K	0.01167	5.54×10^{-10}	1.251×10^9	29.17
^{235}U	0.7200	9.85×10^{-10}	7.038×10^8	568.7
^{238}U	99.2743	1.551×10^{-10}	4.468×10^9	94.65
^{232}Th	100.00	4.95×10^{-11}	1.401×10^{10}	26.38

Table R2 Some geochemical estimates of K, U, and Th in Earth's primitive mantle (mantle plus crust or bulk silicate Earth (BSE))

K	U	Th	References
231	0.021	–	Wanke *et al*. (1984)
180	0.018	0.064	Taylor and McClennan (1985)
266	0.0208	–	Hart and Zindler (1986)
258	0.0203	0.0813	Hofmann (1988)
240	0.0203	0.0795	McDonough and Sun (1995)
235	0.0202	0.0764	Van Schmus (1995)[a]

All values are in parts per million.
[a]Suggested average values.

Drake and Righter (2002) have discussed the general difficulty of using chondritic meteorites for the initial starting composition of the Earth. Given these considerations, and the debate about whether the mantle is compositionally layered, the geochemical estimates of K, U, and Th in Table R2 seem not well constrained.

Geophysical models use terrestrial heat-flow data or other aspects of geodynamics and plate tectonics to constrain the radioactivity of the mantle. Global average heat-flow estimates range from 30 to 44 TW (TW = 10^{12} W). The higher value (Pollack *et al*., 1993; Stein, 1995) is greater than twice the radiogenic heat production of various C1 models (see compilation by Lodders and Fegley, 1998). Even at the recently suggested heat flux of 31 ± 1 TW (Hofmeister and Criss, 2005), the C1 models fall short by about 10–12 TW. This short-fall may be satisfied by considering a significant secular cooling delay of >1–2 Ga (Ga = 10^9 years) where the surface heat flux represents radiogenic heat produced in the past, or by including residual primordial heat from the time of accretion. Definitive conclusions about either of these possibilities cannot be reached at present. Alternatively, additional radioactive heat sources in the interior can also meet the global surface heat flux requirement.

The only meteorite materials with O-isotopic composition similar to the Earth (and the Moon) are the enstatite chondrites (EH, EL) and the enstatite achondrites (aubrites). Models of the Earth with EH chondrites as precursor materials have been considered in some recent studies (Javoy, 1995; Lodders, 1995, 2000; Hofmeister and Criss, 2005). These models have the advantage of simultaneously satisfying the stringent requirement of the O-isotopic composition, the high iron content of the Earth, and the global heat-flow data. Models of this type result in a BSE with higher radioactive contents than those listed in Table R2. For example, Hofmeister and Criss (2005) find that suitable BSE compositions that satisfy the surface heat flux of 31 TW can be represented by compositions or mixtures with EH meteorites as one end member. If the terrestrial K/U of 10^4 is a constraint, for no secular cooling delay or delay of <1 Ga, a BSE composition with 300–350 ppm K, about 30–35 ppb U, and 110–130 ppb Th is required. Higher heat fluxes lead to even higher K, U, and Th contents. Using essentially EH chondrites as precursor materials, Lodders (1995) estimated the model BSE to contain over 1000 ppm K. It thus appears that estimates of the radioactivity of the silicate portion on the Earth (~68% by mass of the planet) cannot be uniquely constrained at present; rather, we have some model-dependent estimates that need further evaluation.

Radioactivity of the core

Radioactivity in the core has been a controversial topic for a long time. The traditional view is that there is no radioactivity in the core (see for example, McDonough, 1999). In contrast, some recent developments in experiments and theory suggest the possible presence of radioactivity in the core. Of the radioactive elements discussed here, K is the only element for which there is some basis both in theory and experiment (Murthy *et al*., 2003; Lee *et al*., 2004 and the references cited in the papers). Table R3 summarizes the theoretical and experimental estimates of K from these studies and the corresponding radiogenic heat production in the core. U and Th have been hypothesized to be in the core (Herndon, 1980), but the experimental investigations so far are inconclusive or contradictory.

The estimated core-mantle boundary (CMB) heat flux ranges from 2 to 12 TW (Labrosse and Macouin, 2003 and references cited therein). The CMB heat flux controls the rate of core cooling. Nimmo *et al*. (2004) have studied the question of how best to reconcile the CMB heat flux with the small size of inner core together and the >3.5 Ga age of the magnetic field. These authors note that the presence of K in the core at about 400 ppm is in best accord with the present size of the inner core and the power needs of a geomagnetic dynamo for the past 3.5 Ga. Using somewhat different parameters, similar conclusions have been reached by others (Labrosse, 2003 and the references cited therein). Purely thermal models of the core call for an additional heat source in the core and in view of the recent experimental data, it is reasonable to attribute this to the radioactivity of K in the core.

Table R3 Estimates of potassium abundance in the core from geochemical models, theoretical calculations, and recent experiments and the corresponding heat production in terawatts (TW) today

Method	Abundance (ppm)	Radiogenic heat production (TW)	References
Geochemical models	0	0	McDonough and Sun (1995), McDonough (1999), and GERM database
Theoretical	550±260	~4–5	Lodders (1995)[a]
	200–400		Buffett (2003)
	250–750		Labrosse (2003)
	Up to 1420	9	Roberts *et al*. (2003)[b]
	400	~3	Nimmo *et al*. (2004)
Experimental	<1	0.01	Chabot and Drake (1999)
	100–250	~0.8–2.0	Gessman and Wood (2002)
	60–130	0.4–0.8	Murthy *et al*. (2003)
	Up to 7000	Up to 45	Lee and Jeanloz (2003)[c]
	35	0.23	Hirao *et al*. (2005)

The GERM database values are shown for comparison.
[a]With chondritic U and Th.
[b]As quoted in Labrosse and Macouin (2003).
[c]See discussion in Lee and Jeanloz (2003). This is an upper limit; for realistic conditions of core formation in the Earth, the authors note that the value is likely to be much less.

We have made major strides in deciphering the chemistry and physics of the Earth's interior in the past few decades but the specific radioactive content of the mantle is not well constrained yet. The new evidence for radioactivity and radiogenic heat in the core is receiving much increased attention from geophysical and geochemical theorists and experimentalists because of its impact on the thermal and chemical evolution of the core, the planet, and the geomagnetic field.

V. Rama Murthy

Bibliography

Anderson, D.L., 1989a. Composition of the Earth. *Science*, **243**: 367–370.

Anderson, D.L., 1989b. *Theory of the Earth*. Boston: Blackwell Scientific Publications (http://resolver.caltech.edu/CaltechBOOK:1989.001).

Buffett, B.A., 2003. The thermal state of the earth's core. *Science*, **299**: 1675–1677.

Chabot, N.L., and Drake, M.J., 1999. Potassium solubility in metal: the effects of composition at 15kbar and 1900°C on partitioning between iron alloys and silicate melts. *Earth and Planetary Science Letters*, **172**: 323–335.

Clayton, R.M., 1993. Oxygen isotopes in meteorites. *Annual Review of Earth and Planetary Sciences*, **21**: 115–149.

Drake, M.J., and Righter, K., 2002. Determining the composition of the Earth. *Nature*, **416**: 39–44.

GERM, *A Geochemical Earth Reference Model* (http://earthref.org/GERM/index.html).

Gessman, C.K., and Wood, B.J., 2002. Potassium in the Earth's core? *Earth and Planetary Science Letters*, **200**: 63–78.

Hart, S.R., and Zindler, A., 1986. In search of a bulk-Earth composition. *Chemical Geology*, **57**: 247–267.

Herndon, J.M., 1980. The chemical composition of the interior shells of the Earth. *Proceedings of the Royal Society of London Series A*, **372**: 149–154.

Hirao, N., Ohtani, E., Kondo, T., Endo, N., Kuba, T., Suzuki, T., and Kikegawa, T., 2005. Partitioning of potassium between iron and silicate at the core-mantle boundary. *Geophysical Research Letters*, **33**: L08303.

Hofmann, A.W., 1988. Chemical differentiation of the Earth. *Earth and Planetary Science Letters*, **90**: 297–314.

Hofmeister, A.M., and Criss, R.E., 2005. Earth's heat flow revised and linked to chemistry. *Tectonophysics*, **395**: 159–170.

Humayun, M., and Clayton, R.N., 1995. Potassium isotope cosmochemistry: genetic implications of volatile element depletion. *Geochimica et Cosmochimica Acta*, **59**: 2131–2148.

Javoy, M., 1995. The integral enstatite chondrite model of the Earth. *Geophysical Research Letters*, **22**: 2219–2222.

Labrosse, S., 2003. Thermal and magnetic evolution of the Earth's core. *Physics of the Earth and Planetary Interiors*, **140**: 127–143.

Labrosse, S., and Macouin, M., 2003. The inner core and the geodynamo. *Comptes Rendus Geoscience*, **335**: 37–50.

Lassiter, J.C., 2004. Role of recycled oceanic crust in the potassium and argon budget of the Earth: toward a resolution of the "missing argon" problem. *Geochemistry Geophysics Geosystems*, **5**: Q11012 (doi: 10.1029/2004GC000711).

Lee, K.K.M., and Jeanloz, R., 2003. High-pressure alloying of potassium and iron: Radioactivity in the Earth's core? *Geophysical Research Letters*, **30**: 2312 (doi: 10.1029/2003GL018515).

Lee, K.K.M., Steinle-Neumann, G., and Jeanloz, R., 2004. *Ab-initio* high-pressure alloying of iron and potassium: implications for the Earth's core. *Geophysical Research Letters*, **31**: L11603 (doi: 10.1029/2004GL019839).

Lodders, K., 1995. Alkali elements in the Earth's core: evidence from enstatite chondrites. *Meteoritics*, **30**: 93–101.

Lodders, K., 2000. An oxygen isotope mixing model for the accretion and composition of rocky planets. *Space Science Reviews*, **92**: 341–354.

Lodders, K., and Fegley, B.J., Jr., 1998. *The Planetary Scientist's Companion.* Oxford: Oxford University Press.

Mattern, E., Matas, J., Ricard, Y., and Bass, J., 2005. Lower mantle composition and temperature from mineral physics and thermodynamic modeling. *Geophysical Journal International*, **160**: 973–990.

McDonough, W.F., 1999. Earth's core. In Marshall, C.P., and Fairbridge, R.W. (eds.), *Encyclopedia of Geochemistry.* Dordrecht: Kluwer Academic Publishers.

McDonough, W.F., and Sun, S.-S., 1995. The composition of the Earth. *Chemical Geology*, **120**: 223–253.

Murthy, V.R., van Westrenen, W., and Fei, Y., 2003. Experimental evidence that potassium is a substantial radioactive heat source in planetary cores. *Nature*, **423**: 163–165.

Nimmo, F., Price, G.D., Brodholt, J., and Gubbins, D., 2004. The influence of potassium on core and geodynamo. *Geophysical Journal International*, **156**: 363–376.

Pollack, H.N., Hunter, S.J., and Johnson, J.R., 1993. Heat flow from the Earth's interior: analysis of the global data set. *Reviews of Geophysics*, **31**: 267–280.

Roberts, P.H., Jones, C.A., and Calderwood, C.A., 2003. Energy fluxes and ohmic dissipation in the Earth's core. In Jones, C.A., Soward, A.M., and Zhang, K. (eds.), *Earth's Core and Lower Mantle.* London: Taylor and Francis.

Stein, C.A., 1995. Heat flow of the Earth. In Ahrens, T.J. (ed.) *A Handbook of Physical Constants: Global Earth Physics,* AGU Reference Shelf 1. Washington, DC: American Geophysical Union, pp. 144–158.

Taylor, S.R., and McClennan, S.M., 1985. *The Continental Crust: Its Composition and Evolution.* Oxford: Blackwell Scientific Publications, 312 pp.

Van Schmus, W.R., 1995. Natural radioactivity of the crust and mantle. In Ahrens, T.J. (ed.) *Global Earth Physics: A Handbook of Physical Constants,* AGU Reference Shelf 1. Washington, DC: American Geophysical Union, pp. 283–291.

Wanke, H.G., Dreibus, G., and Jagoutz, E., 1984. Mantle chemistry and the accretion history of the Earth. In Kroner, A., Hanson, G.N., and Goodwin, A.M. (eds.) *Archean Geochemistry.* New York: Springer-Verlag, pp. 1–24.

Cross-references

Core Composition
Core Origin
Core-Mantle Boundary, Heat Flow Across
Geodynamo, Energy Sources

REDUCTION TO POLE

Introduced by Baranov (1957) (see also, Baranov and Naudy, 1964), the reduction-to-pole transformation of total field magnetic anomalies (see crustal magnetic field) is intended to remove the skewness of the anomalies (see Figure R1). The transformation makes the anomalies overlie the sources, makes it possible to correlate the magnetic anomalies with other types of geophysical anomalies (e.g., gravity) and geological information, and aids their interpretation. In reality, even the amplitude of the anomaly is affected (increased) when sources of induced magnetization are observed at poles in comparison to lower magnetic latitudes because the Earth's field intensity increases from equator to poles; some of the reduction-to-pole methods can take this change in amplitude into account (e.g., equivalent source method) while the others typically do not (e.g., rectangular coordinate wavenumber domain methods). The expression of a magnetic anomaly, ΔT, due to a localized spherical source of uniform magnetization is helpful in understanding the transformation

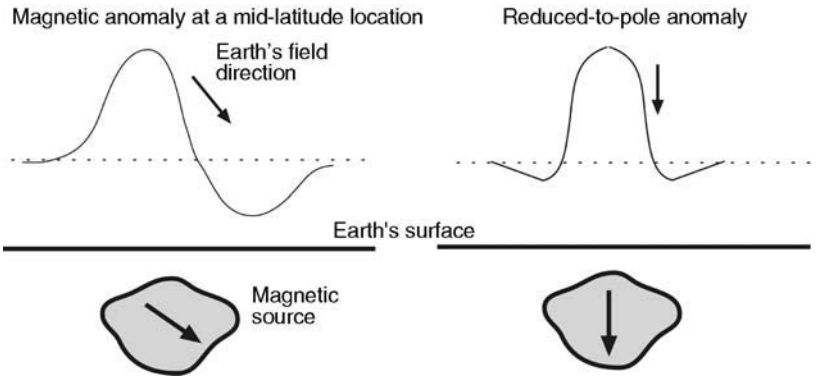

Figure R1 Skewness of a magnetic anomaly due to a uniform arbitrarily magnetized source below Earth's surface in an obliquely oriented Earth's magnetic field (left) and its reduced-to-pole expression in the vertical magnetization and vertical field conditions (right).

$$\Delta T(r) = -\frac{\partial}{\partial \beta}\Delta V_\alpha(r) = \Delta J \frac{\partial^2}{\partial \beta \partial \alpha}\frac{1}{r},$$

where r is source to observation distance, ΔV_α is anomalous potential due to the uniform anomalous magnetization direction α, ΔJ is the intensity of anomalous *magnetization* (*q.v.*), and β is the direction of the Earth's main field (assumed uniform). To derive the anomalous source function ($\Delta J/r$), one integrates the equation twice, once with respect to β (to find the anomalous potential), and once with respect to α. The magnetization direction of the source is usually not known and, therefore, induced magnetization is assumed, leading to $\alpha = \beta$. The reduced-to-pole magnetic anomaly (vertical intensity anomaly due to vertical magnetization) can then be computed by twice differentiating this source function in the vertical direction (to find first the potential due to the vertically magnetized source, and then its anomaly in the vertical direction) as

$$\Delta T_z(r) = \Delta Z(r) = \frac{\partial^2}{\partial z^2}\int_{-\infty}^{\infty}\int_{-\infty}^{\infty}\Delta T(r)\partial\alpha\partial\beta,$$

where both ΔZ and ΔT_z represent the vertical intensity magnetic anomaly.

In practice, these computations are significantly easier to perform in the wavenumber domain, where the process of integration involves division by a factor and differentiation involves multiplication by a factor. Under induced magnetization conditions (i.e., $\alpha = \beta$), the reduced-to-pole anomaly in the wavenumber domain is given by

$$\Delta T_z(k)^* = |k|^2 \frac{\Delta T(k)^*}{B^2},$$

where asterisks denote wavenumber domain representation of the respective anomalies, k is the radial wavenumber; in Cartesian coordinates, $k = (k_x^2 + k_y^2)^{1/2}$, where k_x and k_y are the wavenumbers in x and y directions; and $B = 1/[\mathrm{i}k_x \cos I \cos D + \mathrm{i}k_y \cos I \sin D + k \sin I]$, where I and D are the main field inclination and declination, respectively, and the trigonometric quantities represent direction cosines in the north, east, and down directions, respectively. An iterative wavenumber domain method for variable directions of magnetization and Earth's field intensity appropriate for a large region is described by Arkani-Hamed (1988).

Another customary approach of achieving reduction to pole is through the equivalent source technique (Dampney, 1969; Emilia, 1973; von Frese *et al*., 1981, 1988; Silva, 1986), where a configuration of equivalent sources is first assumed. Magnetization is generally assumed in the direction of the inducing field, but it can also be different if known for particular sources. Using inverse methods, and taking advantage of Green's principle of the equivalent layer (see Blakely, 1995), one can map magnetization variation for the region where anomalies are available. Using the derived magnetization distribution, it is possible to compute the reduced-to-pole anomaly under vertical magnetization and vertical Earth's field conditions.

The equivalent source method is subject to instabilities due to a variety of reasons (e.g., spacing of sources, altitude difference between observations and the sources, low magnetic inclinations, etc.), but most of the instabilities can be reduced or eliminated using damped least-squares or ridge regression approach (Silva, 1986; von Frese *et al*., 1988). The wavenumber domain reduction-to-pole operations also encounter instabilities in low magnetic latitudes ($<30^\circ$ inclination, i.e., when the terms involving vertical component of direction cosines are close to zero). Under these circumstances, when the other two direction cosines nearly negate one another, which happens along a line in a k_x–k_y plane due to the shape of the reduction-to-pole filter (see, e.g., Blakely, 1995), the quantity B^2 is nearly zero and small errors in the anomaly field are significantly enlarged in the reduction-to-pole process. Hansen and Pawlowski (1989) describe methods to overcome these artifacts by designing a Wiener filter for this purpose.

Dhananjay Ravat

Bibliography

Arkani-Hamed, J., 1988. Differential reduction-to-the-pole of regional magnetic anomalies. *Geophysics*, **53**: 1592–1600.

Baranov, V., 1957. A new method for interpretation of aeromagnetic maps: pseudo-gravimetric anomalies. *Geophysics*, **22**: 359–383.

Baranov, V., and Naudy, H., 1964. Numerical calculation of the formula of reduction to the magnetic pole. *Geophysics*, **29**: 67–79.

Blakely, R.J., 1995. *Potential Theory in Gravity and Magnetic Applications.* Cambridge: Cambridge University Press.

Dampney, C.N.G., 1969. The equivalent source technique. *Geophysics*, **34**: 39–53.

Emilia, D.A., 1973. Equivalent sources used as an analytic base for processing total magnetic field profiles. *Geophysics*, **38**: 339–348.

von Frese, R.R.B., Hinze, W.J., and Braile, L.W., 1981. Spherical earth gravity and magnetic anomaly analysis by equivalent point source inversion. *Earth and Planetary Science Letters*, **53**: 69–83.

von Frese, R.R.B., Ravat, D., Hinze, W.J., and McGue, C.A., 1988. Improved inversion of geopotential field anomalies for lithospheric investigations. *Geophysics*, **53**: 375–385.

Hansen, R.O., and Pawlowski, R.S., 1989. Reduction to the pole at low latitudes by Wiener filtering. *Geophysics*, **54**: 1607–1613.

Silva, B.C.J., 1986. Reduction to the pole as an inverse problem and its application to low latitude anomalies. *Geophysics*, **51**: 369–382.

Cross-references

Crustal Magnetic Field
Magnetic Anomalies

REPEAT STATIONS

Definition

Repeat stations are permanently marked sites where it is possible to make accurate observations of the Earth's magnetic field vector for a period of a few hours (sometimes a few days) every few years. Their main purpose is to track secular variation (see *Geomagnetic secular variation* and *Time-dependent models of the geomagnetic field*) and, if accurate observational techniques and careful reduction procedures are followed, they can be a cost-effective way of supplementing observatory data for secular-variation modeling. Figure R2 shows a plot of repeat station locations. The distribution is somewhat uneven, being determined more by local need and resources rather than requirements to achieve global coverage.

History

One of the earliest repeat station networks was in the UK where 190 stations were established and measurements were made at each by Sabine and colleagues in the 1830s (see *Sabine, Edward*). Many of these sites were reoccupied between 1857 and 1861. However, as the distribution of these stations was somewhat uneven and records enabling their further reoccupation do not seem to have survived, Rücker and Thorpe established a new network between 1884 and 1888 comprising some 200 stations (Barraclough, 1995 and references therein). Some of these stations are still in use today although probably none are exact reoccupations. Elsewhere in the world, the Carnegie Institution of Washington, Department of Terrestrial Magnetism (see *Carnegie Institution of Washington, Department of Terrestrial Magnetism*) permanently marked sites to enable reoccupation during their excursions around the world starting in the early 20th century (see *Bauer, Louis Agricola*) and many countries began to establish repeat station networks at around about this time.

Equipment

The instruments are usually the same as those used at magnetic observatories; a fluxgate theodolite to measure declination and inclination and a proton precession magnetometer (PPM) to measure field strength (see *Observatories, instrumentation*). At observatories fixed marks are usually already surveyed in but this is not always the case at repeat stations. Therefore additional instrumentation may be necessary for the determination of true north. This may be a gyro-attachment for the theodolite, eyepieces or sun filters and accurate timing equipment for sun or star observations, or separate geodetic-quality Global Positioning System (GPS) units. Also often necessary is a tent to provide shelter for the equipment and observer from the weather.

Procedures

Great care is taken to ensure that exact reoccupation of the site is made at each visit because, if there is an appreciable local gradient in the crustal field, any error in positioning the instruments will contaminate the resulting secular-variation data. At each visit a site survey with a PPM is usually done to check for magnetic contamination of the repeat station. An auxiliary station is established a few meters from the marked site and the difference in the total intensity of the field between these two sites is established using two PPMs running simultaneously. Depending on the method being used to determine true north the fluxgate theodolite or GPS unit may then be set up over the marked site. The fluxgate theodolite for observing declination and inclination is then set up over the marked site. The PPM at the auxiliary station logs data for the duration of the declination and inclination observations. Several rounds of observations are made over a number of hours, each round involving four circle readings to eliminate collimation errors between the theodolite telescope and the fluxgate sensor and within the theodolite itself.

An important aspect of the data reduction procedures is correction for the regular daily variation (see *Periodic external fields*) and magnetic storms (see *Storms and substorms, magnetic*). When repeat stations are close to observatories, these variations are observed and corrected for using continuous observatory data. Elsewhere, especially for repeat stations in areas of complex external fields such as the auroral zones or remote from geomagnetic observatories, on-site variometers are sometimes run to monitor these variations.

A useful publication for guidance on repeat station survey procedures is that published under the auspices of IAGA (Newitt *et al.*, 1996, see *IAGA*).

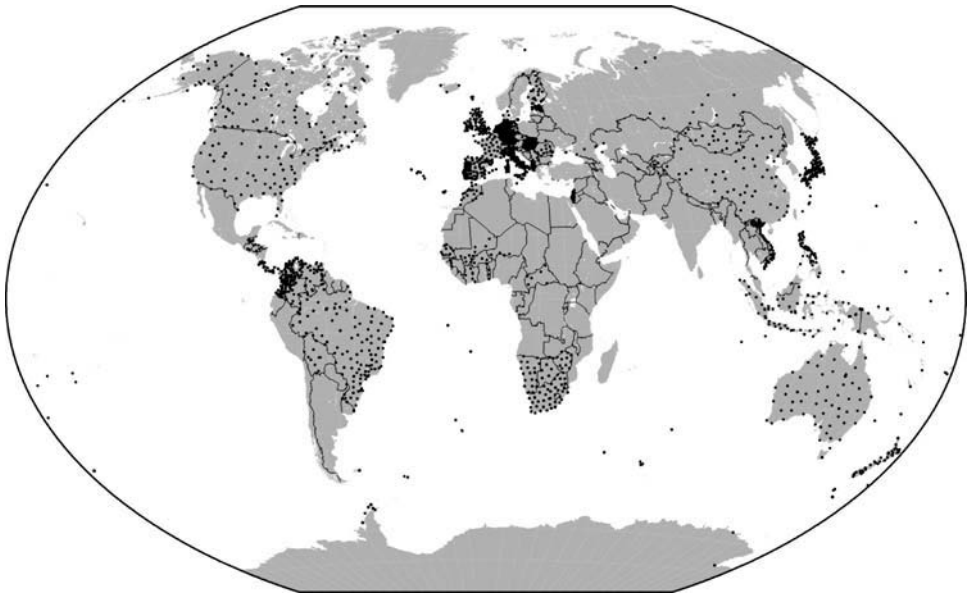

Figure R2 Locations of all known repeat stations visited more than once since 1975.

Use in modeling

Efforts to model the field over restricted regions of the Earth for the purposes of mapping rely on good local coverage of vector data such as that provided by repeat stations. Different approaches are used around the world depending on the extent of the area and coverage of data, but the most common is some form of spherical cap harmonic analysis (SCHA) (see *Harmonics, spherical cap*). As well as being applied in many individual countries to map the magnetic field, for example Canada, Spain, South Africa, SCHA has also been applied to European repeat station data to search for secular-variation anomalies. However, the degree of success has been limited partly because of the high uncertainties associated with the data (Korte and Haak, 2000). Repeat station data have also been used in global modeling and help fill in some gaps in the observatory distribution.

Susan Macmillan

Bibliography

Barraclough, D.R., 1995. Observations of the Earth's magnetic field made in Edinburgh from 1670 to the present day. *Transactions of the Royal Society of Edinburgh: Earth Sciences*, **85**: 239–252.

Korte, M., and Haak, V., 2000. Modelling European magnetic repeat station data by SCHA in search of time-varying anomalies. *Physics of the Earth and Planetary Interiors*, **122**: 205–220.

Newitt, L.R., Barton, C.E., and Bitterly, J., 1996. *Guide for Magnetic Repeat Station Surveys*. International Association of Geomagnetism and Aeronomy.

Cross-references

Bauer, Louis Agricola (1865–1932)
Carnegie Institution of Washington, Department of Terrestrial Magnetism
Geomagnetic Secular Variation
Harmonics, Spherical Cap
IAGA, International Association of Geomagnetism and Aeronomy
Observatories, Instrumentation
Periodic External Fields
Sabine, Edward (1788–1883)
Storms and Substorms, Magnetic
Time-Dependent Models of the Geomagnetic Field

REVERSALS, THEORY

Once it was appreciated that reversals of the geomagnetic field occurred (see *Geomagnetic polarity reversals*), it was natural to seek a theoretical understanding of these events. The dominant, dynamo theory for the generation of the Earth's field has no difficulty accounting for configurations in which the field is reversed from the present "normal" polarity; but detailed mechanisms, explaining how and why the field comes to reverse, remain the topics of active research, with many fundamental questions still to be definitively answered. Are reversals isolated phenomena, triggered by exceptional events within the core, or are they simply part of the normal range of the dynamical variations of the geodynamo? Does a reversal transition involve a fundamentally different regime of dynamo action (e.g., a period of field decay), or is it a relatively minor variation in the normal behavior? How does the transition field compare with the normal field? Despite the current lack of final answers, dynamo theory has been used to address all of these questions. (Reversal mechanisms have also been proposed for some of the alternative theories of geomagnetism; see *Nondynamo theories*.)

Equivalence of normal and reverse polarity states

Within the general theory of *Magnetohydrodynamics* (*q.v.*), the overall sign of the magnetic field is not dynamically important; the governing equations remain unchanged, if a field in the opposite direction is substituted (see *Geodynamo, symmetry properties*). There is therefore no problem in accounting for fields of both "normal" and "reverse" polarities (with dipoles oriented parallel and antiparallel to the present-day field, respectively). Indeed, if a state such as the present-day field exists, then the reverse state must be equally possible, theoretically; it is therefore gratifying that observations suggest that both polarities have occurred equally frequently, over the lifetime of the geomagnetic field.

The dynamo can therefore be viewed as a "bistable" system, which may reside in one of two equivalent states of opposite polarity; it is relatively stable within either of these states (or else reversals would be more common than they are), and yet is prone to occasionally flipping from one state to the other. The theoretical problem is to explain how, and why, the field moves between these two states in the irregular manner which it does. This remains a rather broad question, which may be addressed in many different ways. Some authors have focused on the study of individual reversals, considering in more detail how one particular reversal is "triggered", and exactly what happens to the field as it undergoes the process; others have considered the problem over longer timescales, developing models which seek to explain the statistical properties of sequences of reversals.

Kinematic mechanisms

The first successful models of dynamo action were kinematic models (see *Dynamos, kinematic*), which prescribed a flow, and investigated the magnetic field generated by this flow. It is therefore natural that some of the first attempts to explain reversals related to such models; these were typically formulated in terms of the *mean field* or *Braginsky dynamos* (*q.v.*) which were being developed at about the same time.

Within the kinematic problem, a stationary flow can generate fields of either stationary or oscillatory character (which may both ultimately grow or decay, depending on the overall strength of the flow). If the flow is made up of a number of components whose relative magnitude may be varied (e.g., differential rotation, "cyclonic" convection, and meridional circulation; the most common ingredients of mean field dynamo models), then solutions of different character are typically preferred for different forms of the velocity. Changes in the underlying flow can therefore result in changes in the nature of the field being excited (or decaying); and if the velocity moves through a suitable sequence of states, then a field reversals may be effected. The various kinematic mechanisms all propose some such sequence of velocity variations.

It is worth explicitly noting that some variation in the velocity is required, to obtain an irregularly reversing field; a stationary flow can only produce stationary or periodically reversing fields, as described above. The types of velocity variations envisaged in kinematic mechanisms are therefore entirely plausible; it is only the arbitrary manner in which the variations are assumed, without reference to the coupled dynamics of the full dynamo problem, that makes kinematic mechanisms somewhat unsatisfactory. Nevertheless, these mechanisms may still effectively isolate the important physics of reversal transitions, and thus provide insights often lost in more complex dynamical simulations.

One such mechanism was suggested by Braginsky (1964), when he first considered the consequences of dynamo action in his "nearly axisymmetric" system (see *Dynamo, Braginsky*). He found that, in the absence of a component of meridional circulation (i.e., an axisymmetric flow whose streamlines lie on planes of constant azimuth), his flows preferred to excite oscillatory fields; with some meridional circulation present, however, stationary fields were preferred. (The same situation often pertains to solutions of the closely related mean field dynamo systems.) He therefore argued that the geodynamo may normally function in the latter regime, with some meridional circulation stabilizing the solution, to give the predominantly steady geomagnetic field. If a fluctuation takes the velocity into a state with weaker meridional circulation, however, it is easy to see how an oscillation might commence, from the initially steady field. (And if the original flow

was near the boundary in preferences, then only an infinitesimal change of velocity might be needed.) Indeed, such an oscillation might be expected to take the form of a simple *dynamo wave* (*q.v.*). If the flow has returned to its original state after a single change of sign of the field (i.e., about half a period of the oscillating solution), then a stationary solution will again be preferred; but now, the stationary solution will be based on the post-oscillation field, in its new, reversed state. The same mechanism was later highlighted by Gubbins and Sarson (1994), who carried out three-dimensional kinematic calculations; and Sarson and Jones (1999) later found the effect to be important within a dynamical calculation, described below.

An alternative series of kinematic mechanisms was developed from original papers by Parker (1969) and Levy (1972). All of these are based on some form of *mean field dynamo* (*q.v.*), and rely on fluctuations in the strength or location of the eddy flows, or "cyclones", responsible for producing dipolar field from azimuthal field via the so-called "alpha"-effect. Parker (1969) noted that an occasional excess of cyclones at high latitudes (or a relative dearth at low latitudes) led to the fields generated at low latitudes being of opposite sign to the original, stable configuration. The new state therefore acts "degeneratively", with respect to the original field; if this situation persists for long enough for the low-latitude field to reverse sign, before the normal flow regime is restored, then the subsequent generation will be based on the new field sign, and a reversal will have been achieved. In a similar scheme, applied to a related mean field model, Levy (1972) showed that an occasional period of high-latitude cyclone activity, in a dynamo which normally generates field via low-latitude activity (or *vice versa*), would likewise lead to the field in some regions being "flooded" with fields of the "reverse" sign; this again can lead to a reversal, if the episodes are suitably timed. In contrast with the meridional circulation mechanism, these schemes are based entirely on stationary kinematic solutions, and rely upon the different morphologies of field excited before and after the change in velocity, to effect the reversal.

In all such kinematic mechanisms, the change in velocity responsible for triggering the reversal—and the change responsible for subsequently stabilizing the system in the new polarity—is simply imposed, and is not subject to self-consistent dynamical forces (including the feedback of the field on the flow). It may also seem rather convenient that the change of flow persists for just long enough to undergo a single transition, leading to a reversal. But in defense of the mechanism, shorter deviations in flow would plausibly give rise to excursions, which may occur more frequently than full reversals. Such fluctuations in the flow may be happening all the time, with only the more extreme cases leading to reversals (e.g., Gubbins, 1999). Additionally, there are some dynamical reasons to accept that the flow might plausibly be restored on the timescale of the field oscillation itself.

Other kinematic mechanisms are also possible, of course. It has been suggested by more than one author, for example, that reversals may begin when the field and flow have evolved to a state too close to being axisymmetric. Then, since *Cowling's theorem* (*q.v.*) states that such an axisymmetric state cannot be maintained, a period of field decay must commence; and depending upon the subsequent development of field and flow, a reversal may occur before the normal generation process is resumed. (A number of similar "free decay" models have been proposed, where interruptions to the normal state of convection result in flows unable to sustain dynamo action, and thus also leading to periods of field decay, and the possibility of reversals.)

Dynamic mechanisms

The obvious limitation in the kinematic mechanisms outlined above—as with kinematic theories in general—is the lack of a self-consistent treatment of the varying velocity responsible for the reversal; the equations of motion are not explicitly addressed. This is particularly unsatisfactory given that the magnetic field is thought to play a dynamically important role in the dynamo process; so that a reversal is rather likely to influence the velocity.

A strong case can be made for the geodynamo being in a so-called "strong field" state, with the magnetic Lorentz force being a dominant force. Since the magnetic field often acts to make convection easier (see, e.g., *Magnetoconvection*), then such a state may be dynamically distinct from nonmagnetic or weakly magnetic states, in the sense that it requires some "boot-strapping" to attain: the dynamo is stable, as long as the field is present; but if the field is lost, e.g., as a result of natural fluctuations, then the entire convective state may decay. In such a scenario, a reversal may occur as a catastrophic event, with the dynamo losing the strong field solution branch, and both field and flow initially decaying. Subsequently, convection must reestablish itself, and the strong field state may ultimately be reattained. Given the drastic nature of this field collapse, however, it is quite reasonable to allow that fluctuations might result in the new field having been seeded with either polarity, so that a reversal may have occurred. Such a scenario was envisaged by Zhang and Gubbins (2000), who noticed the extreme sensitivity of magnetoconvection calculations to the strength of the dipolar magnetic field, in particular.

Such dynamic mechanisms differ from kinematic mechanisms through their consideration of the evolving equations of motion (particularly with respect to the Lorentz force) during the reversal process. This makes such scenarios formidably complex, however, and detailed reversal mechanisms along these lines remain relatively uncommon. In terms of appreciating the dynamics of reversals, more work has perhaps been invested in studying the reversals observed in numerical geodynamo simulations. Dynamic mechanisms are also inherent in the dynamical systems models discussed further below.

Reversals in numerical simulations

Another approach to understanding reversals theoretically—possible since the advent of detailed numerical simulations (see *Geodynamo, numerical simulations*)—is to study the reversals produced by such simulations phenomenologically, to try to understand why these particular systems, at least, undergo reversals. Given the inability of these simulations to attain the regime of the geodynamo, reversal mechanisms deduced in this way may or may not ultimately prove relevant to geomagnetic reversals; yet such studies remain clearly of interest. The output of such simulations is highly complex, however, with field and flow fluctuating together in ways that can be difficult to track, so that clear-cut mechanisms for reversals remain difficult to isolate.

Glatzmaier and Roberts (1995) noted that their reversal was accompanied by oscillations in the quadrupole component of the field, and also noted that the reversal proceeded through a relatively complex sequence of events, with the azimuthal field, and then the dipole field in the interior, reversing before the dipole field visible at the surface. They also identified an effect earlier noted by Hollerbach and Jones (1993), that the solid inner core can act to stabilize the system, providing a "reservoir" of field that cannot easily be overturned by short-term oscillations (and thus stabilizing the field to the sort of fluctuations envisaged by Gubbins, 1999). Nevertheless the overall picture remains extremely complicated, and a clear causal process is not obvious.

In a calculation with highly truncated azimuthal resolution, Sarson and Jones (1999) observed a reversal to occur shortly after a fluctuation in the meridional circulation of their solution. They could therefore relate their reversal to one of kinematic mechanisms outlined above, an interpretation that was endorsed by subsequent kinematic calculations. In this case, however, the fluctuation in meridional circulation occurred as a natural part of the full dynamic system. (It appeared to be related to a surge in the buoyancy driving.)

In perhaps the most detailed study of simulated reversals to date, Wicht and Olson (2004) analyzed a sequence of reversals obtained from a single calculation, highlighting a relatively clear sequence of effects. They also found meridional circulation to play an important role in this reversal process (and also verified this role via related kinematic calculations). Unfortunately, these reversals did not occur in a very Earth-like solution; e.g., the flow contained a significant

component of transequatorial flow, which is not expected to be significant within *rotating convection* (*q.v.*). Furthermore, as the authors themselves point out, the solution behaves almost kinematically, with the magnetic field playing no important dynamical role; again, rather far from the case expected for the Earth. (It is arguably true that all of the current numerical dynamo models behave rather too kinematically, with the magnetic field never yet playing as strong a dynamical role as it should in the geodynamo.)

Li *et al*. (2002) obtain irregular reversals in a weakly compressible, ideal gas, dynamo system. Interestingly, they find their system to possess more than one steady state (in either polarity), differentiated by different relative signs of the dipole and octupole terms. In the "high energy" state, characterized by antialigned dipole and octupole moments, the system is susceptible to reversals. This state is also associated with more vigorously fluctuating convection, and by significant transequatorial flows (as in Wicht and Olson, 2004). As in the reversal of Glatzmaier and Roberts (1995), a significant component of axial quadrupole field is observed during the transitions.

It is somewhat encouraging that the current set of numerical simulations seem to share at least some aspects of their reversal behavior. On the other hand, the detailed mechanisms occurring within any of the simulations remain imperfectly understood; and the ultimate relevance of these simulations to the geodynamo remains unproven. While promising, therefore, the analysis of reversals from numerical simulations remains at rather an early stage, in terms of deriving new models for geomagnetic reversals.

Dynamical systems approaches

The preceding sections discussed attempts to analyze individual reversals in terms of detailed deterministic processes. Another, parallel line of enquiry, however, is concerned with the analysis of sequences of reversals. Sufficiently many reversals have been observed that reasonable sequence statistics are available (e.g., describing the statistical distribution of the durations of the stable polarity intervals). By taking sequences of "synthetic" reversals from numerical models, and calculating comparable statistics for these, theoreticians can check the long-term time-behavior of their dynamo models.

Unfortunately, obtaining reversal sequences of the length required, from the detailed numerical simulations described above, is computationally prohibitive. For this approach, a rather simplified model is required instead; various authors have chosen a variety of ways to isolate simple sets of equations which allow reversals, while, hopefully, retaining much of the essential physics of the dynamo process. In studying these systems, the dynamics omitted from the earlier kinematic mechanisms is restored to central place Yet within this approach, the question "why does the field reverse?" is not often addressed. It is accepted that such dynamical systems are subject to occasional reversals (and the systems studied are, essentially, constructed to exhibit such behavior); reversals are just one part of the normal range of behavior, together with secular variation or excursions.

This approach has a long history, going back to the coupled disk dynamos of Rikitake (1958), based on the homopolar *disk dynamo* (*q.v.*) earlier studied by Bullard. The original disk dynamo had been proposed as a heuristic model of dynamo action; by coupling two such disks together, and obtaining a system of equations exhibiting irregular reversals, Rikitake derived a heuristic model for dynamical systems reversals. This model, notably, predates the 1963 Lorenz equations—derived in a similar spirit to model atmospheric convection—which have become something of a paradigm for deterministic chaos. Although the coupled disk dynamos do not model the geodynamo more than schematically—the disk dynamo is perhaps best viewed simply as an analogue of the true geodynamo system, rather than being essentially related to it—they have retained interest as a simple dynamical model of reversals, and been subject to many studies and refinements; some early work on these systems is summarized in Moffatt (1978). While the coupled disk dynamos exhibit behavior suggestive of reversals and excursions, however, the statistics of such behavior is not particularly "Earth-like", and alternative models have been proposed, following a variety of approaches.

Melbourne *et al*. (2001) constructed a model based on the interaction of various symmetries of magnetic field—axial dipole, equatorial dipole, and axial quadrupole—that separate in the kinematic problem, for geophysically plausible symmetries of the velocity (see *Geodynamo, symmetry properties*). For certain specializations from the generic form for the dynamical interaction of such symmetries, this system has structurally stable "heteroclinic cycles," which allow intermittent excursions and reversals between dominantly axial dipole states; and for some choices of parameters, the sequences of reversals display relatively realistic properties. While somewhat abstract in construction, the explicit use of symmetry interactions in this model is an attractive feature, potentially allowing more detailed comparisons with the paleomagnetic record, or with the output of detailed numerical simulations.

Although most models studied in this vein have been of "low order"—evolving typically just a few scalar variables, as proxies for the whole complex process of dynamo action—models of increasing complexity can now also be studied in this way. Hoyng *et al*. (2001) considered a nonlinear, axisymmetric *mean field dynamo* (*q.v.*), with the addition of random fluctuations to the "alpha"-effect term responsible for the generation of dipole field. The fluctuations model the variations in this flow on rapid timescales (cf. the magnetic timescales explicitly modeled here); in a sense they implement, in a random way, the type of fluctuations envisaged in the kinematic mechanisms of Parker and Levy. The resulting system exhibits plausible reversal behavior, with a Poissonian distribution of inter-reversal intervals, as is often claimed for the paleomagnetic data.

A complementary approach is taken by Narteau *et al*. (2000), who couple a simple mean field model for the magnetic field to a rather complex "multiscale" model for the evolution of the flow producing the "alpha"-effect. This model tries to simulate the evolution of eddy flows over a variety of length scales, albeit in a rather phenomenological way (with the cascades of energy both up and down the range of length scales being controlled in a rather arbitrary manner). The result, however, is a system containing some memory of past behavior, allowing for a wide variety of reversal behavior.

All of the above models show how the intermittent behavior observed of reversals can arise, from relatively simple dynamical systems modeling the nonlinear interactions of interest in the full geodynamo system. The challenges for future work in this direction are to identify which interactions appear most important, in modeling the true reversal behavior, and to develop this type of analysis towards more realistic simulations.

Long-term changes in reversal behavior

The preceding analyses have assumed the problem of reversal behavior to be a static problem; they have assumed that the Earth's core is in some stationary base state, and that the observed reversal behavior reflects this underlying state (with a single statistical distribution, for example, being applicable across the whole span). Given the timescales for the evolution of the Earth's core (see, e.g., *Core origin*), this is a reasonable approximation for the analysis of individual transitions, or of reversal sequences of even moderate length. Yet considered over the full history of the geomagnetic field, it need not obviously remain valid. Another approach, also amenable to theoretical enquiry, considers mechanisms whereby variations in the mean state of the core over such timescales can affect the reversal behavior. Note that this approach assumes that there truly are significant variations in reversal behavior which can be investigated, and this is not yet definitively resolved. Even relatively "obvious" changes in long-term reversal behavior, such as superchrons (see *Superchrons, changes in reversal frequency*), might alternatively arise from "intermittency" in the dynamical system responsible for the reversals. Yet there remain some clear theoretical reasons why the long-term reversal behavior might vary.

Receiving most attention to date has been the thermal influence of the overlying mantle, which evolves on a much slower timescale than the core, effectively applying very slowly varying boundary conditions to the latter system (see *Core-mantle boundary coupling, thermal*). Different regimes of reversal behavior can then be anticipated for different states of this boundary; one configuration might produce flows conducive to reversals, while another may produce very stable flows. This possible effect has already been illustrated via a suite of dynamo simulations by Glatzmaier *et al*. (1999), incorporating a series of different thermal boundary conditions, and indeed obtaining different patterns of reversal behavior. While the exact relation between the simulations and the true Earth remains open to debate (as with all current simulations), the potential importance of such coupling on reversals remains clear.

Another long-term effect of potential importance is the slow growth of the Earth's inner core, which has solidified within the fluid outer core since the original differentiation of the Earth's interior (see, e.g., *Core origin*. For a number of reasons—including the important role of the inner core in permitting *chemical convection* (*q.v.*) in addition to thermal convection; the nonnegligible geometrical effect of a moderately sized inner core; the importance of the *Inner core tangent cylinder* (*q.v.*) on outer core fluid dynamics; and the magnetically stabilizing role of the inner core noted by Hollerbach and Jones (1993)—it is very likely that different regimes of dynamo behavior existed during different stages of inner core growth. Although some simulations have begun to address this topic (e.g., Roberts and Glatzmaier, 2001), the net effect of all these factors remains far from clear. Nevertheless, the potential importance to long-term reversal behavior is apparent.

Both of the above mechanisms are discussed in more detail under *Superchrons: changes in reversal frequency* (*q.v.*).

Graeme R. Sarson

Bibliography

Braginsky, S.I., 1964. Kinematic models of the Earth's hydrodynamic dynamo. *Geomagnetism and Aeronomy*, **4**: 572–583 (English translation).

Glatzmaier, G.A., and Roberts, P.H., 1995. A three-dimensional self-consistent computer simulation of a geomagnetic field reversal. *Nature*, **377**: 203–209.

Glatzmaier, G.A., Coe, R.S., Hongre, L., and Roberts, P.H., 1999. The role of the Earth's mantle in controlling the frequency of geomagnetic reversals. *Nature*, **401**: 885–890.

Gubbins, D., 1999. The distinction between geomagnetic excursions and reversals. *Geophysical Journal International*, **137**: F1–F3.

Gubbins, D., and Sarson, G., 1994. Geomagnetic field morphologies from a kinematic dynamo model. *Nature*, **368**: 51–55.

Hollerbach, R., and Jones, C.A., 1993. Influence of the Earth's inner-core on geomagnetic fluctuations and reversals. *Nature*, **365**: 541–543.

Hoyng, P., Ossendrijver, M.A.J.H., and Schmitt, D., 2001. The geodynamo as a bistable oscillator. *Geophysical and Astrophysical Fluid Dynamics*, **94**: 263–314.

Levy, E.H., 1972. Kinematic reversal schemes for the geomagnetic dipole. *Astrophysical Journal*, **171**: 635–642.

Li, J., Sato, T., and Kageyama, A., 2002. Repeated and sudden reversals of the dipole field generated by a spherical dynamo action. *Science*, **295**: 1887–1890.

Melbourne, I., Proctor, M.R.E., and Rucklidge, A.M., 2001. A heteroclinic model of geodynamo reversals and excursions. In Chossat, P., Armbruster, D., and Oprea, I. (eds.) *Dynamo and Dynamics: A Mathematical Challenge.* Dordrecht: Kluwer, pp. 363–370.

Moffatt, H.K., 1978. *Magnetic Field Generation in Electrically Conducting Fluids.* Cambridge: Cambridge University Press.

Narteau, C., Blanter, E., Le Mouël, J.-L., Shirnman, M., and Allègre, C.J., 2000. Reversal sequences in a multiple scale dynamo mechanism. *Physics of the Earth and Planetary Interiors*, **120**: 271–287.

Parker, E.N., 1969. The occasional reversal of the geomagnetic field. *Astrophysical Journal*, **158**: 815–827.

Rikitake, T., 1958. Oscillations in a system of disk dynamos. *Proceedings of the Cambridge Philosophical Society*, **54**: 89–105.

Roberts, P.H., and Glatzmaier, G.A., 2001. The geodynamo, past, present and future. *Geophysical and Astrophysical Fluid Dynamics*, **94**: 47–84.

Sarson, G.R., and Jones, C.A., 1999. A convection driven geodynamo reversal model. *Physics of the Earth and Planetary Interiors*, **111**: 3–20.

Wicht, J., and Olson, P., 2004. A detailed study of the polarity reversal mechanism in a numerical dynamo model. *Geochemistry Geophysics Geosystems*, **5**: Q03H10.

Zhang, K., and Gubbins, D., 2000. Is the geodynamo process intrinsically unstable? *Geophysical Journal International*, **140**: F1–F4.

Cross-references

Convection, Chemical
Convection, Nonmagnetic Rotating
Core-Mantle Coupling, Thermal
Core Origin
Cowling's Theorem
Dynamo Waves
Dynamo, Braginsky
Dynamo, Disk
Dynamos, Kinematic
Dynamos, Mean Field
Equilibration of Magnetic Field, Weak and Strong Field Dynamos
Geodynamo, Numerical Simulations
Geodynamo, Symmetry Properties
Geomagnetic Polarity Reversals
Inner Core Tangent Cylinder
Magnetoconvection
Magnetohydrodynamics
Nondynamo Theories
Superchrons, Changes in Reversal Frequency

RIKITAKE, TSUNEJI (1921–2004)

The late Tsuneji Rikitake (1921–2004), professor emeritus of the University of Tokyo and the Tokyo Institute of Technology, contributed greatly to the advancement of the following areas in geomagnetism through his extensive research activity, mostly at the Earthquake Research Institute, University of Tokyo, Japan.

1. Electromagnetic induction by geomagnetic variations and the electrical state of the Earth's interior
2. Short-period geomagnetic variations and electrical conductivity anomalies in the upper *mantle* (*q.v.*)
3. Dynamo theory as a mechanism of Earth's magnetic field generation
4. Fluid motion in the Earth's *core* (*q.v.*)
5. A model of polarity reversal of the magnetic field (*q.v.*)
6. *Magnetohydrodynamic waves* (*q.v.*) in the Earth's core
7. Geomagnetic and geoelectric changes associated with earthquakes
8. Electrical resistivity changes of rocks associated with strain and their application to earthquake prediction
9. Magnetic anomalies of volcanoes and their changes before and after volcanic eruptions (see *Volcano-electromagnetic effects*)

Figure R3 Professor Tsuneji Rikitake (1921–2004).

Rikitake (Figure R3) proposed a global model of electrical conductivity distribution in the Earth's interior by his own analyses of various types of geomagnetic variations since the latter half of the 1940s and a theory of electromagnetic response of a spherical conductor. He then found an anomaly in the vertical component of short-period geomagnetic variations in central Japan in the early 1950s. Subsequent intensive observations revealed a systematic short-period geomagnetic variation anomaly, called the Central Japan Anomaly, which was one of the earliest findings of a series of similar anomalies over the globe. He interpreted such an anomaly in terms of a conductivity anomaly, possibly undulation of the surface of the conducting *mantle* (*q.v.*). Conductors under oceanic areas seemed to be depressed under the Japanese island arc; this was understood as representing subduction of the oceanic plate beneath the island arc. Such pioneer work stimulated, in 1972, an *IAGA* (*q.v.*) workshop on electromagnetic induction; these workshops have been continued every two years, the latest (18th) having been held in Spain. Rikitake is also well known as one of the pioneers in *Magnetotellurics* (*q.v.*) for investigating the crust and upper mantle.

Rikitake was also one of the pioneers in the so-called dynamo problem in the 1950s, but without the use of high-speed electronic computers. The epoch-making work of Sir *E.C. Bullard* (*q.v.*), widely known for the *Bullard-Gellman dynamo* model (*q.v.*), showed how the magnetic field might be generated in the Earth. However, no kinematic dynamo model can give rise to polarity reversal. One day an idea suddenly came to the mind of Rikitake when he was in the train in Tokyo. He must have been thinking about the *disk dynamo* (*q.v.*), for which a nonreversing analytical solution had been found by Sir Edward Bullard. In an analogy to possible turbulence in the Earth's core, he considered two disks coupled together electrically. This coupled-disk model cannot be solved analytically because of nonlinearity, so Rikitake solved the nonlinear equations numerically using a mechanical calculator. He found a spontaneous polarity *reversal* (*q.v.*). This result was published by Rikitake (1958), 5 years before the finding of a famous example of *chaos* by a meteorologist, E.N. Lorentz. It should be remembered that recent numerical results for MHD dynamo models, derived from high-speed supercomputers, have shown the occurrence of such a spontaneous reversal. This coupled-disk model has been called the Rikitake model.

Rikitake was a professor at the Earthquake Research Institute and hence was naturally involved in earthquake and volcano studies. In the 1960s an earthquake swarm hit a small town in central Japan. Rikitake undertook electric and magnetic measurements in an attempt to find anomalous phenomena associated with earthquakes. He became one of the most distinguished experts in this research field. In particular, he found from *in situ* observations that the electrical resistivity of rock changes in response to small strains. He then devised and installed a very sensitive field instrument and discovered many examples of resistivity steps associated with earthquakes that obviously corresponded to strain steps. His interest expanded further to include various kinds of phenomena precursory to earthquakes and to systematic understanding of precursory phenomena—for example, he established empirical relations for precursory times and earthquake magnitudes.

Rikitake's research achievements were published in more than 200 original papers and more than 50 books. Although most of the books were written in Japanese, some books are written in English, such as "Electromagnetism and the Earth's Interior" (1966), or "Earthquake Prediction" (1976) which have proved invaluable to graduate students and researchers over the world.

Y. Honkura

Bibliography

Rikitake, T., 1958. Oscillations of a system of disk dynamos. *Proceedings of the Cambridge Philological Society*, **54**: 89–105.

Cross-references

Bullard, Edward Crisp (1907–1980)
Core Motions
Dynamo, Bullard-Gellman
Dynamo, Disk
EM, Regional Studies
IAGA, International Association of Geomagnetism and Aeronomy
Magnetohydrodynamic Waves
Magnetotellurics
Reversals, Theory
Seismo-Electromagnetic Effects
Volcano-Electromagnetic Effects

RING CURRENT

The Earth's ring current consists of millions of Amperes of electrical current, encircling the Earth in space near and within the geosynchronous orbit (6.6 Earth radii). It is a feature of the interaction between the magnetized conducting solar wind and the Earth, with its geomagnetic field and conducting ionosphere.

The geomagnetic field is a peculiar feature of Earth when compared to our planetary neighbors in the inner solar system. Mercury has a weak dipolar magnetic field, but Mars' field consists of scattered patches of remnant crustal magnetization, and Venus has no sensible planetary field. It seems plausible that the geomagnetic field has played an important role in the habitability of Earth, but this is so far unproven. We do know that the geomagnetic field creates a well-defined bubble in space, called a *magnetosphere* (*q.v.*). The Earth's ionosphere expands into and fills the magnetosphere with a low density conducting plasma (the fourth state of matter, consisting of free electrons and their parent ions) that is to some degree confined within it but eventually escapes.

The solar atmosphere, also in the plasma state, similarly expands into a well-defined bubble called the *heliosphere*, consisting of the solar wind plasma and magnetic field and their extension to the limits of the solar system. Just as the Earth's magnetospheric bubble is embedded in the solar wind, the heliospheric bubble is embedded within the interstellar medium, a partially ionized plasma having its own magnetic field, flowing generally away from the galactic center, but otherwise of so far indeterminate characteristics. Our galaxy has a bubble of its own, with a boundary at the edge of intergalactic space.

Owing to solar variations and activity, the solar wind inside the heliosphere is highly variable in intensity and magnetic structure, on timescales much shorter than the time required for a particular parcel of the solar wind to expand to the boundary of the heliosphere.

Many types of motion of conducting gases or fluids generate electrical currents that in turn produce magnetic fields. Much as surface tension acts to confine water in droplets or air in bubbles, magnetic fields act to confine plasmas in magnetic cells. When two cells of plasma collide, or when a single magnetic cell of plasma divides into two smaller cells that go separate ways, their magnetic field lines are reconfigured accordingly by a process called *reconnection*, which links or unlinks magnetic field lines between the two cells at their boundaries. The behavior of magnetic cells is loosely analogous to the behavior of surface tension bubbles, but the magnetic field and its cohesive influence are distributed throughout a plasma cell and are not concentrated at the boundaries, as surface tension is for water droplets or air bubbles. Magnetic field lines act more like a connective tissue of fibers that thread the entire cell of plasma, rather than as a membrane at the outer boundary.

When two magnetic cells collide, magnetic field lines that were initially limited to the respective cells become linked from one cell to the other. Cohesive electromagnetic forces are created that act to accelerate each of the cells toward the velocity of the other, tending toward a merger and the formation of a single unified plasma cell with properties weighted by the relative contributions of the two merged cells.

Conversely, if any section of a magnetic plasma cell should acquire a large velocity relative to the overall cell of which it is a part, the magnetic field may not be strong enough to maintain the integrity of the initial cell. In such a case, the cell will stretch out as the errant plasma attempts to escape from the cell proper. Depending upon the amount of momentum acquired by the plasma and the strength of the magnetic field, the cell magnetic field may become so highly distorted by the stretching motion that a separate blob of plasma is formed and the overstretched field is pinched off between the two. Field lines connecting the cell with the errant subcell are then reconnected so that they no longer link the two and are confined to their respective cells. Readers may recognize this behavior as being analogous to the behavior of fluid cells confined by surface tension, a familiar example being found in the "lava lamp" that became popular in the 1960s.

We have been discussing discrete cells of plasma and their magnetic fields. But what if one cell is much larger than another and the smaller is embedded within the larger, as the larger one streams by at high velocity. This is the situation of Earth's magnetosphere, embedded within the solar wind. The large bubble will tend to engulf and acquire the smaller cell; to pick it up and carry it off downstream, and assimilate it. The solar wind and geomagnetic fields reconnect so that they are interlinked, and the magnetic forces that are created seek to accelerate Earth's ionospheric plasma up to solar wind speed while simultaneously exerting drag on the solar wind plasma. The electrical currents that form link the solar wind to the roots of the interlinked field lines, in the auroral zone around each magnetic pole.

The larger cell (solar wind flow in the heliosphere) seeks continuously to link to and entrain the small cell into itself. Conversely, the smaller cell seeks to slow down the solar wind and entrain it into itself, but can succeed only to a limited degree. The outermost contents of the smaller cell are accelerated downstream, driving a return flow through the interior of the small cell. When this circulation is sufficiently strong, the slowed solar wind and accelerated ionospheric plasmas form an errant plasma cell in the tail of the magnetosphere, which episodically pinches off and escapes from the main cell, forming new cells of mixed plasma called "plasmoids." These are carried off downstream in the solar wind. The result is a continual ablation of the plasma in the smaller cell, which is fed by the sunlit atmosphere and auroral zones. A substantial amount of solar wind is slowed down and incorporated into the magnetosphere, with excess energy being either thermalized or transferred to the ionospheric plasmas. This increases the ionospheric plasma contribution to the cell and the rate of loss downstream.

So finally, we come to the formation of the ring current (Figure R4). As the solar wind seeks to erode away the plasma and fields of the Earth and carry them off downstream, the magnetosphere responds by forming a ring of current around the Earth that increases the total dipole moment of the Earth and inflates the magnetic field lines. This is a result of the energy dissipation associated with the work or effort on the part of the solar wind to accelerate and assimilate the magnetosphere. The situation is analogous to a water droplet suspended in a supersonic gas flow, for which the frictional interaction is so intense that it heats the droplet contents, turns them to vapor, and only then carries them off downstream.

In the magnetosphere, solar wind energy dissipation goes partly into the ionosphere and partly into the plasma clouds of the magnetosphere. Energy going into the ionosphere and atmosphere causes them to expand and inflate upward against gravity into the magnetosphere. The energy that goes into the magnetospheric plasma clouds (which

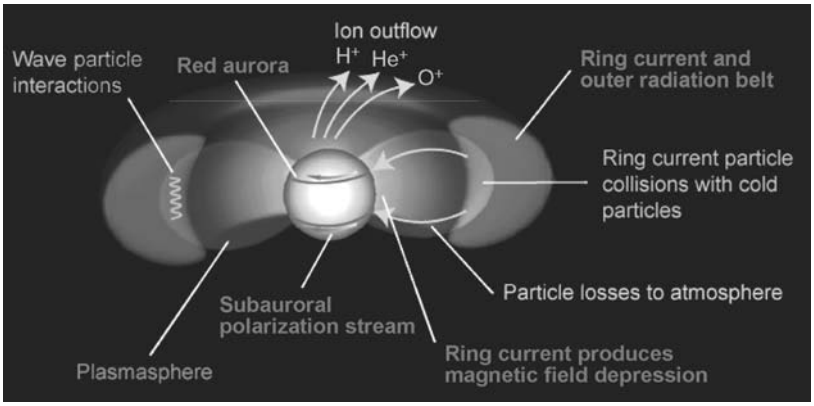

Figure R4 The Earth's ring current is depicted as a red toroidal or donut-shaped region encircling the Earth near the equator inside geosynchronous orbit (6.6 Earth radii). Also shown are the cold extended ionospheric region known as the *plasmasphere;* the ionospheric outflow regions at latitudes higher than the plasmaspheric boundary, and ionospheric features such as the subauroral red (SAR) arcs and polarization streams. Coulomb collisions and wave particle interactions are indicated as loss mechanisms operating on the ring current particles.

then contain more material from the ionosphere) raises the pressure of those plasmas to the point that they inflate the magnetic field that confines them. This is just another way of saying that the plasmas carry currents in the same sense as the Earth's core, adding to the total dipole moment of the planet and inflating the geomagnetic field. Since the pressure and current exists in space around the Earth, it reduces the magnetic field intensity near Earth's surface, while increasing it outside the ring of current.

This can also be viewed as a Faraday's law response: any action that changes a magnetic field induces a current with a sense to oppose that change. The harder the solar wind blows and the more it tries to erode the magnetosphere, the more current is generated in magnetospheric plasmas in such a sense as to oppose that erosion and inflate the magnetosphere. In fact, the solar wind is a tempestuous medium, and the magnetosphere is buffeted by its variations. A side effect of this buffeting is the acceleration of a fraction of the charged particles to very high energies, creating large variations of the Van Allen radiation belts around the Earth.

The ring current was originally discovered by 1917 as the reduction of the magnetic field near the equator of the Earth, by as much as 1–2%. It was inferred by Chapman and Ferraro that this was consistent with a large scale current flowing around the Earth in space (see Bibliography), adding to the dipole moment of the Earth. Theoretical work refined this inference quantitatively, and the advent of spacecraft measurements led to direct observations of the responsible particles, which are mainly ions in the energy range of 50–500 keV. Energetic electrons carry at most 20% of the current. Beginning in the 1970s, ion composition observations showed that the ring current acquires a substantial component of oxygen ions when it becomes strong. These O^+ ions have certainly come from the ionosphere, illustrating the point made above that solar and terrestrial plasmas mix when the solar wind interaction is very strong. The largest ring currents consist almost entirely of ionospheric O^+ plasmas, making it clear that the ring current results in large part from the ablation of the ionosphere into space by solar wind energy deposition.

In recent years, the IMAGE mission has enabled us to globally image and visualize the dynamics of both the outflow of ionospheric plasmas into the magnetosphere, and the creation of high pressure clouds of ionospheric and solar plasmas that produce the ring current. Imaging of plasmas is made possible by a fundamental interaction between atoms and ions in which an electron is exchanged between a fast ion and a slow atom; leading to a fast atom and a slow ion. The fast atom, no longer bound by electromagnetic forces, flies off in a straight line. Suitable cameras record the "glow" of fast atoms coming from any hot plasma that coexists within a neutral gas. For Earth, the hot ring current plasmas coexist with the so-called "geocorona" of the Earth, a spherical region of declining hydrogen density that extends well beyond geosynchronous orbit and a fraction of the way to the moon. Global imaging has revealed some surprises about the ring current, including the fact that it is stronger on the night side than on the day side when it intensifies, and only relaxes into a symmetric ring shape as it fades. This and other more subtle aspects of the ring current can be understood through study of the motions of individual charged particles in the disturbed electromagnetic fields of the storm time magnetosphere.

Other planets that have substantial internal magnetic fields also have ring currents. These include Mercury, Jupiter, Saturn, Neptune, and Uranus in our own planetary system. Presumably other magnetized planets would share this feature, provided that a mechanical energy source dissipates energy in the plasma confined with each magnetosphere. Mercury has a magnetosphere so small that there is not much room for a ring current, and it has very little sensible atmosphere, so the internal source of plasma is weak. Mariner 10 observations of Mercury will soon be complemented by new observations by the Messenger spacecraft, which will greatly increase our understanding of this case. Jupiter is a special case in that it is so large and rotates so rapidly (every 10 h) that more energy comes from braking the rapid rotation than from braking the solar wind flow. Nevertheless, a strong ring current results as plasma from the atmospheres of both the planet and its moons (especially Io) fill the magnetosphere and are spun up by the planetary rotation. Saturn rotates less rapidly and has a solar wind interaction more like that of Earth. It also has a strong ring current inflation of its magnetic field. The magnetosphere of Neptune is also more like that of Earth in terms of ring current, but that of Uranus is peculiar in that the spin and dipole axes are tilted to a large angle from the ecliptic plane normal, so that the magnetosphere lies nearly "pole-on" to the solar wind for half of the Uranian "year." The Earth may resemble Uranus in this respect during a geomagnetic field reversal. This leads to a magnetosphere whose tail is nearly aligned with its magnetic poles, yielding significant differences in the shape of many magnetospheric features. Nevertheless, Uranus has a substantial ring current, and for the same reasons: internal plasmas from the planet, its moons, and the solar wind are heated by energy dissipation, building up pressure and inflating the dipolar magnetic field region.

Ring currents are thus a common feature of magnetospheres filled with hot plasma. That includes in some sense the magnetized astrospheres of the sun and other stars, whose stellar plasma winds inflate their magnetic fields enormously, distending them throughout their astrospheres and generating extended ring currents. In these cases the energy to create and inflate the plasma currents comes from the object itself, rather than being derived from an enveloping medium, as is the case for the Earth's magnetosphere. On the other hand, a rotation-dominated magnetosphere like Jupiter's may be understood as an intermediate case in which energy to create and heat the plasma originates both internally and externally. In summary, ring currents should be thought of as natural extensions of the intrinsic magnetic fields of astrophysical objects, which are sustained when the supply of energy is sufficient to create and maintain a plasma atmosphere of sufficient pressure.

Thomas E. Moore

Bibliography

Burch, J.L., 2001. The Fury of space storms. *Scientific American*, **284**: 86–94.

Cladis, J.B., and Francis, W.E., 1985. The polar ionosphere as a source of the storm time ring current. *Journal of Geophysical Research*, **90**: 3465.

Daglis, I., 2003. Magnetic storm—still an adequate name? *Eos Transactions American Geophysical Union*, **84**(22): 207–208.

Fok, M.-C., Wolf, R.A., Spiro, R.W., and Moore, T.E., 2001. Comprehensive computational model of the Earth's ring current. *Journal of Geophysical Research*, **106**(A5): 8417.

Hamilton, D.C., Gloeckler, G., Ipavich, F.M., Stüdemann, W., Wilken, B., and Kremser, G., 1988. Ring current development during the great geomagnetic storm of February 1986. *Journal of Geophysical Research*, **93**: 14343.

Kistler, L.M., Ipavich, F.M., Hamilton, D.C., Gloeckler, G., Wilken, B., Kremser, G., and Stüdemann, W., 1989. Energy spectra of the major ion species in the ring current during geomagnetic storms. *Journal of Geophysical Research*, **94**: 3579–3599.

Kozyra, J.U., Shelley, E.G., Comfort, R.H., Brace, L.H., Cravens, T.E., and Nagy, A.F., 1987. The role of ring current O+ in the formation of stable auroral red arcs. *Journal of Geophysical Research*, **92**: 7487.

Moore, T.E., Chandler, M.O., Fok, M.-C., Giles, B.L., Delcourt, D.C., Horwitz, J.L., and Pollock, C.J., 2001. Ring currents and internal plasma sources. *Space Science Reviews*, **95**(1/2): 555–568.

Williams, D.J., 1985. Dynamics of the Earth's ring current: theory and observations. *Space Science Reviews*, **42**: 375.

Cross-reference

Magnetosphere of the Earth

ROBUST ELECTROMAGNETIC TRANSFER FUNCTIONS ESTIMATES

Deep probing electromagnetic (EM) induction methods use naturally occurring temporal variations of EM fields observed at the surface of the earth to map variations in electrical conductivity within the Earth's crust and mantle. In the magnetotelluric (MT) method, which is most commonly used for studies of crustal and upper mantle conductivity structure, both electric and magnetic fields are measured at a series of sites. Under the generally reasonable assumption that external sources are spatially uniform, the two horizontal components of the electric field variations can be linearly related to the two horizontal magnetic field components through a 2×2 frequency-dependent impedance tensor. Estimation of these impedances from the raw electromagnetic time series (Figures R5 and R6) is the first step in the interpretation of MT data, followed by inversion of the estimated impedances for Earth's conductivity, and then mapping of electrical conductivity to parameters more directly related to geological processes. The MT impedance tensor is a particular case of a more general electromagnetic response or transfer function (TF). This article focuses primarily on MT impedances and their estimation, but other closely related examples of TFs are also discussed briefly.

The earliest approaches to MT TF estimation were based on classical time series methods (e.g., Bendat and Piersol, 1971), applying a simple linear least squares (LS) fitting procedure to a series of Fourier transformed data segments (Figure R5). However, MT data quality can be highly variable, with both signal and noise amplitudes varying by orders of magnitude over the data record. Furthermore, contrary to the standard LS assumption, there is typically noise in both the "output" or predicted electric field channels, and the "input" or independent magnetic channels, leading to biases in TF estimates. As a consequence the simplest LS approach often fails to yield physically reasonable or reproducible results. Two developments have improved the situation considerably: remote reference, in which data from a simultaneously operating second MT site is used for noise cancellation (Gamble *et al*., 1979), and data adaptive robust TF estimation schemes which automatically downweight or eliminate poor quality data (Egbert and Booker, 1986; Chave *et al*., 1987).

Electromagnetic induction transfer functions

The basic assumption underlying the EM TF approach is that the external source variations which induce currents in the earth can be approximated well as random linear combinations of a small number of modes of fixed known geometry. In the most important case, relevant to MT, the external sources are assumed to be spatially uniform and hence linear combinations of two simple modes: unit magnitude sources linearly polarized North-South and East-West, respectively. Physically this assumption is justified if the spatial scale of external magnetic fields at the Earth's surface is large compared to the depth of penetration of the EM fields in the conducting Earth. Except at long periods ($>10^4$ s), for which penetration depths in the Earth exceed several hundred kilometers, and in the auroral zone where ionospheric current systems vary over short-length scales, this assumption generally holds quite well. For very long-period global studies other sorts of simplifying source assumptions are used to justify TFs.

Uniform source transfer functions

For periodic sources at a fixed frequency the uniform source assumption implies that the horizontal electric and magnetic field vectors measured at a single site are linearly related in the frequency domain as

$$\begin{pmatrix} E_x \\ E_y \end{pmatrix} = \begin{pmatrix} Z_{xx}(\omega) & Z_{xy}(\omega) \\ Z_{yx}(\omega) & Z_{yy}(\omega) \end{pmatrix} \begin{pmatrix} H_x \\ H_y \end{pmatrix}. \qquad \text{(Eq. 1)}$$

The 2×2 TF $\mathbf{Z}$, which depends on frequency ω, is referred to as the impedance tensor; see Figure R6 for an example. Equation(1) can be justified by the linearity of Maxwell's equations, and the assumption that all sources can be expressed as linear combinations of two linearly independent polarizations. Under these circumstances, two independent field components (e.g., H_x and H_y at one location) uniquely determine all other EM field components everywhere in the domain. The uniform source assumption also justifies other sorts of TFs. In particular, vertical magnetic fields can be linearly related to the two horizontal components at the local site

$$H_z = \begin{pmatrix} T_x(\omega) & T_y(\omega) \end{pmatrix} \begin{pmatrix} H_x \\ H_y \end{pmatrix}. \qquad \text{(Eq. 2)}$$

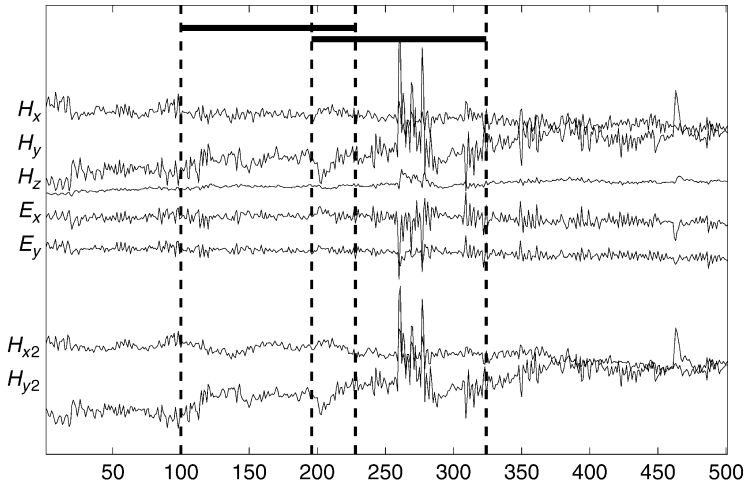

Figure R5 Example of time series used for estimation of MT TFs, from a site near Parkfield, CA. From top, the three vector components of the magnetic field (measured by an induction coil), two colocated orthogonal horizontal electric field components (measured as the potential difference between pairs of electrodes separated by 100m), and two horizontal components of the magnetic field at a distant remote site. Two short (128 point) overlapping data segments are indicated by the vertical dashed lines. Segments such as these are Fourier transformed to yield a series of complex Fourier coefficients for each data channel, which are then used for the various transfer function estimates discussed in the text.

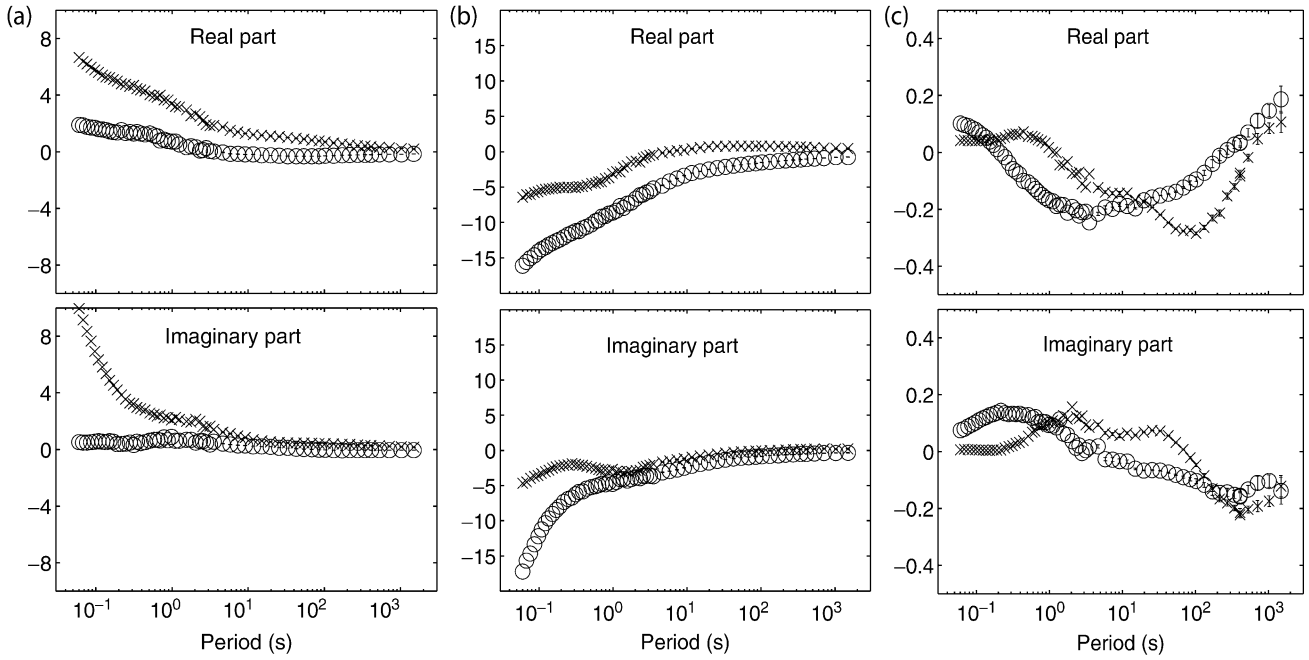

Figure R6 Examples of TFs estimated from the time series of Figure R5. (a) Two components of the TF relating E_x to H_x and H_y, the first row of the impedance tensor: Z_{xx} (circles) and Z_{xy} (crosses). Upper plots give real parts, lower plots imaginary. (b) TF for E_y, the second row of the impedance tensor: Z_{xy} (circles) and Z_{yy} (crosses). Note that the off-diagonal components of the impedance (Z_{xy}, Z_{yx}) are dominant. (c) Vertical field TF T_x (circles), T_y (crosses).

Vertical field TFs (Figure R6c), which are commonly estimated along with the impedance in most MT surveys, are referred to variously as the Tipper vector, Parkinson vector, or Wiese vector (see *Induction Arrows*). Vertical field TFs have frequently been used to map lateral conductivity variations in the crust qualitatively, and they provide useful additional constraints (along with the impedance) in quantitative two- and three-dimensional inversions for conductivity.

When two or more sites are run simultaneously, interstation magnetic TFs can also be defined. These relate magnetic fields at a remote site to the horizontal components at a reference site

$$\begin{pmatrix} H_{x2} \\ H_{y2} \end{pmatrix} = \begin{pmatrix} T_{xx}(\omega) & T_{xy}(\omega) \\ T_{yx}(\omega) & T_{yy}(\omega) \end{pmatrix} \begin{pmatrix} H_{x1} \\ H_{y1} \end{pmatrix}. \qquad \text{(Eq. 3)}$$

Interstation TFs are used to map concentrations of electric current in the crust resulting from lateral variations of conductivity, and can in principle also be used as data for inversion.

Transfer functions for global induction and large arrays

The TFs of (1)–(3) derived from the assumption that external sources are approximately spatially uniform. For global studies and for large arrays other sorts of source assumptions are appropriate, leading to additional examples of induction TFs. The best known of these is the *Z*/*H* TF used for long-period global studies of mantle conductivity. Here the assumption is that external magnetic sources can be approximated as a single zonal dipole (P_1^0). With this one-dimensional source space an appropriate TF is

$$H_z = T_{zh}(\omega) H_x, \qquad \text{(Eq. 4)}$$

i.e., the scalar TF $T_{zh}(\omega)$ is the ratio of vertical (Z) to meridional (H) geomagnetic variation components. Under the assumption that conductivity in the Earth depends only on depth, and that sources are purely P_1^0, $T_{zh}(\omega)$ can be transformed to an equivalent MT impedance. Variants on (4) have also been applied to studies at daily variation periods, with a fixed geometry for sources (dominated by the P_{m+1}^m spherical harmonic for a frequency of m cpd) assumed.

With geomagnetic arrays of large enough size spatial gradients of the magnetic fields can be directly computed, and gradient TFs can be estimated. In the standard approach, the TF function relationship takes the form

$$H_z = C(\omega)[\partial_x H_x + \partial_y H_y]. \qquad \text{(Eq. 5)}$$

Equation (5) strictly applies only to the case where conductivity varies only with depth, and in this case $C(\omega)$ can be converted into an equivalent one-dimensional impedance $Z(\omega) = i\omega C(\omega)$. Extension to the more general case of multidimensional conductivity is possible, as reviewed in Egbert (2002).

Robust transfer function estimation

Least squares estimates

To be explicit consider estimating the MT TF between one component of the electric field (e.g., E_x) and the two horizontal magnetic field components H_x and H_y at a single fixed frequency ω. This TF corresponds to the first *row* of the usual MT impedance tensor. All of the discussion here and in subsequent sections applies equally to the second row of the impedance, and to the other transfer functions outlined above. Because all the TFs are most succinctly described in the frequency domain as in (1)–(5) the first step in processing is generally to Fourier transform the data. After possibly despiking and/or prewhitening, time series for each component are divided into M short time-windows, tapered, and Fourier transformed (Figure R5). Fourier coefficients for N periods in a band centered around ω are used for the TF estimate, for a total of $I = MN$ complex data. Estimates $\hat{\mathbf{Z}}$ of the TF (i.e., impedance elements) are then obtained for frequency ω by LS fitting of the linear model

$$\mathbf{E} = \mathbf{HZ} + \mathbf{e}. \qquad \text{(Eq. 6)}$$

or in matrix notation

$$\begin{pmatrix} E_1 \\ \vdots \\ E_I \end{pmatrix} = \begin{pmatrix} H_{x1} & H_{y1} \\ \vdots & \vdots \\ H_{xI} & H_{yI} \end{pmatrix} \begin{pmatrix} Z_{xx} \\ Z_{xy} \end{pmatrix} + \begin{pmatrix} \varepsilon_1 \\ \vdots \\ \varepsilon_I \end{pmatrix}, \qquad \text{(Eq. 7)}$$

With standard LS this is accomplished by minimizing the sum of the squares of the residuals

$$\sum_i |E_{xi} - (H_{xi}\hat{Z}_{xx} + H_{yi}\hat{Z}_{xy})|^2 = \sum_i |r_i|^2 \rightarrow \text{Min}, \qquad \text{(Eq. 8)}$$

yielding

$$\hat{\mathbf{Z}} = (\mathbf{H}^\dagger\mathbf{H})^{-1}(\mathbf{H}^\dagger\mathbf{E}), \qquad \text{(Eq. 9)}$$

where the superscript † denotes the conjugate transpose of the complex matrix.

The regression M-estimate

The simple LS estimator implicitly assumes a Gaussian distribution for the errors ϵ in (6). This assumption often fails for MT data due to the nonstationarity of both signal and noise, which can result in a marginal error distribution in the frequency domain which is heavy tailed, or contaminated by outliers. As a result, the simple LS estimate all too frequently leads to biased and noisy TF estimates with large error bars (Figure R7a). A number of MT processing methods have been proposed to overcome these difficulties, generally using some sort of automated screening or weighting of the data. Early efforts in this direction used *ad hoc* schemes, for example weighting data segments based on broadband coherence between input and output channels. A more rigorously justifiable approach is based on the regression M-estimate (RME; Huber, 1981), a variant on LS that is robust to violations of distributional assumptions and resistant to outliers (Egbert and Booker, 1986; Chave *et al*., 1987).

For the RME minimization of the quadratic loss functional of (8) is replaced by the more general form

$$\sum_i \rho\left(|E_{xi} - (H_{xi}\hat{Z}_{xx} + H_{yi}\hat{Z}_{xy})|/\hat{\sigma}\right) = \sum_i \rho(|r_i|/\hat{\sigma}) \rightarrow \text{Min}, \qquad \text{(Eq. 10)}$$

where $\hat{\sigma}$ is some estimate of the scale of typical residuals. LS is a special case of the general form of (10), with $\rho(r) = r^2$. By instead choosing ρ to penalize large residuals less heavily than with the quadratic used for LS, the influence of outliers on the estimate can be substantially reduced. The Huber (1981) loss function

$$\rho(r) = \begin{cases} r^2/2 & |r| < r_0 \\ r_0|r| - r_0^2/2 & |r| \geq r_0 \end{cases} \qquad \text{(Eq. 11)}$$

is commonly used with $r_0 = 1.5$ for robust estimation of induction TFs. To find the minimizer of (10) an iterative weighted LS procedure can be used. Let $\psi(r) = \rho'(r)$ be the derivative of the loss function (referred to as the influence function), and set $w(r) = \psi(r)/r$. Then it is easily shown that the minimizer of (10) satisfies

$$\hat{\mathbf{Z}} = (\mathbf{H}^\dagger\mathbf{WH})^{-1}(\mathbf{H}^\dagger\mathbf{WE}), \qquad \text{(Eq. 12)}$$

where $\mathbf{W} = \text{diag}(w_1, \ldots, w_I) = \text{diag}(w(|r_1|), \ldots, w(|r_I|))$ is a diagonal matrix of weights. The RME thus corresponds approximately to the weighted LS problem $\sum_i w(|r_i|)|r_i|^2 \rightarrow \text{Min}$. However the weights depend on the residuals r_i (and hence on the TF estimate), so an iterative procedure is required. Given an estimate of the TF (and of the error scale $\hat{\sigma}$) residuals can be used to calculate weights, and the weighted LS problem can be solved for a new TF estimate. This procedure can be started from a standard LS estimate of the TF (and some robust estimate of error scale) and then repeated until convergence.

For convex loss functions (e.g., the Huber function of (11)) convergence of this procedure to the unique minimizer of (10) is guaranteed (Huber, 1981). For the loss function in (11) the weights are

$$w(r) = \begin{cases} 1 & |r| < r_0 \\ r_0/|r| & |r| \geq r_0 \end{cases}, \qquad \text{(Eq. 13)}$$

i.e., data corresponding to large residual vectors get smaller weights. To allow for a sharp cutoff, with data completely discarded if residuals

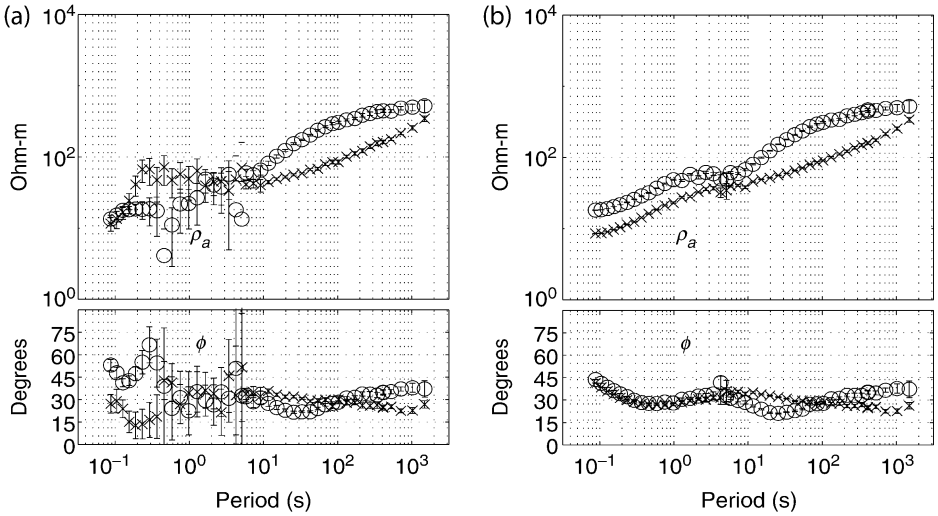

Figure R7 Comparison of TFs estimated from the same time series with (a) standard unweighted LS and (b) the regression M-estimate (RME) described in the text. Here apparent resistivities $\rho_a = (\omega\mu_0)^{-1}|Z|^2$ and phases $\phi = a\tan(Z)$ are plotted, computed from the dominant off-diagonal impedances Z_{xy} (circles) and Z_{yx} (crosses). The LS estimates are too noisy to be useful over much of the frequency range, while the robust estimates vary smoothly with frequency and have small error bars.

exceed a prescribed threshold, a nonconvex loss function must be used. Convergence of the iterative minimization algorithm cannot be guaranteed in this case, so standard practice is to iterate with a convex loss function such as (11) to convergence, followed by a final step with a hard cutoff to completely discard extreme outliers. This completely automated procedure frequently results in significant improvements in TF estimates, as indicated by improvements in smoothness and physical realizability of apparent resistivity and phase curves (Figure R7b), and reproducibility of results.

More *ad hoc* schemes are also frequently used, sometimes in conjunction with the RME, for down-weighting noisy or inconsistent data. These can be viewed as special cases of the weighted LS estimate of (12), but with weights now determined by some criteria other than residual magnitude. For example, in coherence weighting, broadband coherence of input and output channels is used to downweight time segments with low signal-to-noise ratios.

Leverage

The RME can be excessively influenced by a small number of very large amplitude data sections, resulting in breakdown of the estimator. In the terminology of linear statistical models, these large amplitude data are *leverage points*. For the LS estimate the predicted data are

$$\hat{\mathbf{E}} = [\mathbf{H}(\mathbf{H}^{\dagger}\mathbf{H})^{-1}\mathbf{H}]\mathbf{E}, \qquad \text{(Eq. 14)}$$

with the matrix expression in brackets (which maps observed data to be predicted) referred to as the "hat matrix." It is readily shown that the sum of the diagonal elements of the hat matrix satisfies, $\sum_{i=1}^{I} h_{ii} = 2$, and that the individual diagonal elements h_{ii} can be interpreted as the fraction of total magnetic field signal power in the ith Fourier coefficient. Large values of h_{ii} indicate data points with inordinate influence on the TF estimates. Furthermore, in extreme cases leverage points are used heavily to predict themselves, making the iterative RME ineffective. To deal with leverage points in routine MT processing, it is thus useful to include an additional weighting term (a function of the magnitude of h_{ii}) to reduce the influence of any observations of unusually large amplitude.

Remote reference

The linear statistical model (6) is strictly appropriate to the case where noise is restricted to the output, or predicted electric field channels. Violation of this assumption results in the downward bias of estimated impedance amplitudes. These biases are proportional to the ratio of noise power to signal power, and can be quite severe in the so-called MT "dead band" at periods of around 1–10 s (Figure R8). To avoid these bias errors horizontal magnetic fields recorded simultaneously at a remote reference site are correlated with the EM fields at the local site. Letting R_{xi} and R_{yi} be the Fourier coefficients for the two remote site components for the ith data segment, and $\mathbf{R}$ the corresponding $I \times 2$ matrix, then the analogue of the LS estimate is

$$\hat{\mathbf{Z}} = (\mathbf{R}^{\dagger}\mathbf{H})^{-1}(\mathbf{R}^{\dagger}\mathbf{E}). \qquad \text{(Eq. 15)}$$

To generalize the RME to remote reference, one can iterate the weighted analogues of (15), i.e., $\hat{\mathbf{Z}} = (\mathbf{R}^{\dagger}\mathbf{W}\mathbf{H})^{-1}(\mathbf{R}^{\dagger}\mathbf{W}\mathbf{E})$, with the weights on the diagonal of $\mathbf{W}$ determined from the residual magnitudes, exactly as for the single site robust estimator. It is also useful to add some additional weighting to allow for outliers at the remote site, and as with the single site estimates, for leverage.

When arrays of simultaneously operating EM instruments are available more complex procedures, which use data from multiple sites to define the reference fields, are possible (Egbert, 2002).

Error estimates

With a statistical approach to TF estimation, one also obtains estimation error variances which define the precision of the TF estimates. These error bars are ultimately required at the modeling or inversion stage to assess the adequacy of fit of a derived model to the measured data, and thus play an important role in the overall interpretation of EM data. The covariance of the linear LS TF estimate of (9) is readily derived from standard theory, using linear propagation of errors

$$\mathrm{Cov}(\hat{\mathbf{Z}}) = \hat{\sigma}^2(\mathbf{H}^{\dagger}\mathbf{H})^{-1}, \quad \hat{\sigma} = (I-2)^{-1}\sum_i |r_i|^2, \qquad \text{(Eq. 16)}$$

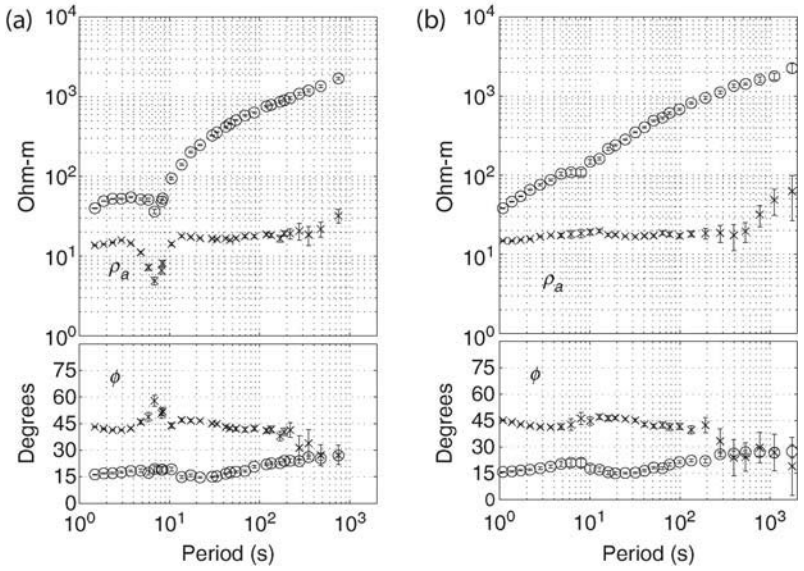

Figure R8 Comparison of TFs (from a different site) estimated with (a) the RME applied to data from a single station and (b) the robust remote reference estimate. As in Figure R7, results are plotted as apparent resistivity and phase. Although both curves are smooth, and have small error bars, a significant (nonphysical) bias is evident in the single site results of (a).

where r_i are again the residuals. An analogous expression for the error covariance for the remote reference estimate is

$$\mathrm{Cov}(\hat{\mathbf{Z}}) = \hat{\sigma}_{\mathrm{r}}^2(\mathbf{R}^\dagger\mathbf{H})^{-1}(\mathbf{R}^\dagger\mathbf{R})(\mathbf{H}^\dagger\mathbf{R})^{-1}, \quad \hat{\sigma}_{\mathrm{r}} = (I-2)^{-1}\sum_i |r_i|^2. \tag{Eq. 17}$$

For both (16) and (17) the diagonal components of the 2×2 covariance matrices are the estimation error variances for the two impedance elements.

For the RME variances of the estimates are complicated by nonlinearity, but asymptotic expressions (valid in the limit of large sample sizes) can be obtained from standard theory (Huber, 1981)

$$\mathrm{Cov}(\hat{\mathbf{Z}}) = \frac{(I-2)^{-1}\sum_i w_i^2|r_i|^2}{\left[I^{-1}\sum_i \psi'(|r_i|/\hat{\sigma})\right]^2}(\mathbf{H}^\dagger\mathbf{H})^{-1}, \tag{Eq. 18}$$

where r_i, w_i, $i=1, I$, and $\hat{\sigma}$ are the residuals, weights, and error scale from the final iteration, and the prime denotes the derivative of the influence function. An analogous asymptotic covariances for the robust remote reference estimates can be given with $(\mathbf{H}^\dagger\mathbf{H})^{-1}$ in (18) replaced by $(\mathbf{R}^\dagger\mathbf{H})^{-1}\mathbf{R}^\dagger\mathbf{R}(\mathbf{H}^\dagger\mathbf{R})^{-1}$.

As an alternative to asymptotic error estimates such as (18), the nonparametric jackknife method (Efron, 1982) has also been frequently used for computing TF error estimates (Thomson and Chave, 1991). The jackknife approach can also be applied to compute error bars for complicated nonlinear functions of TFs, as arise for example in some forms of distortion analysis. The jackknife approach significantly increases computational effort required for TF estimation, unless some approximations are used.

Gary D. Egbert

Bibliography

Bendat, J.S., and Piersol, A.G., 1971. *Random Data: Analysis and Measurement Procedures.* New York: John Wiley and Sons.

Chave, A.D., Thomson, D.J., and Ander, M., 1987. On the robust estimation of power spectra: coherence and transfer functions. *Journal of Geophysical Research*, **92**: 633–648.

Efron, B., 1982. *The Jackknife: The Bootstrap and Other Resampling Methods.* Philadelphia: Society for Industrial and Applied Mathematics.

Egbert, G.D., 2002. Processing and interpretation of electromagnetic induction array data: a review. *Survey of Geophysics*, **23**: 207–249.

Egbert, G.D., and Booker, J.R., 1986. Robust estimation of geomagnetic transfer functions. *Geophysical Journal of the Royal Astronomical Society*, **87**: 173–194.

Gamble, T., Goubau, W., and Clarke, J., 1979. Magnetotellurics with a remote reference. *Geophysics*, **44**: 53–68.

Huber, P., 1981. *Robust Statistics.* New York: John Wiley and Sons.

Thomson, D., and Chave, A., 1991. Jackknifed error estimates for spectra, coherence, and transfer functions. In Haykin, S. (ed.), *Advances in Spectrum Analysis and Array Processing.* Englewood Cliffs: Prentice Hall.

Cross-references

Coast Effect of Induced Currents
Conductivity, Ocean Floor Measurements
EM Modeling, Inverse
Geomagnetic Deep Sounding
Induction Arrows
Magnetotellurics
Natural Sources for EM Induction Studies
Transfer Functions

ROCK MAGNETISM

Introduction

Rock magnetism is the study of the magnetic properties of rocks and it includes the study of magnetic minerals. Rock magnetism is one of the oldest sciences known to man. Historians still debate when the magnetic properties of lodestone (leading stone or compass) were first discovered. Some historians suggest that the Greek philosopher Thales made observations in the 6th century B.C. on lodestone, known today as magnetite. Beginning as early as the 3rd century B.C. the Chinese literature makes reference to the magnetic properties *ci shi*, the loving stone, still another name for magnetite. One early school of thought (the animists), which included Thales, argued that the attraction powers of lodestone occurred because it possessed a soul. Even the commonly referred to father of magnetism, William Gilbert of Colchester (who was born in 1544 and died of the plague in 1603), offered the following explanation for lodestone's magnetic attraction: "the Loadstone hath a soul."

The separation of rock magnetism from the broader subject of magnetism of materials occurred in the first half of the 20th century following particularly influential experimental work of Koenigsberger, Thellier, and Nagata. The theoretical foundations of rock magnetism were later established by Néel. The first book on rock magnetism, written by Nagata in 1953, preceded the first book on paleomagnetism written in 1964 by Irving. Rock magnetism primarily deals with the records of magnetic fields recorded in rocks. The inferences drawn from these records usually fall under the subject of paleomagnetism. An excellent modern comprehensive coverage of rock magnetism has been given by Dunlop and Özdemir (1997). In this brief overview article several topics are introduced that are more fully discussed elsewhere in this volume.

Physics of magnetism

Essentially all materials are magnetic because they possess electrons that have a spin (magnetic moments) and because the electron's motion results in currents with their associated magnetic fields. Magnetism is often subdivided into induced magnetization and "permanent" magnetization. Induced magnetization is described by the equation

$$\mathbf{M} = \chi\mathbf{H},$$

where $\mathbf{M}$ is the magnetization, $\mathbf{H}$ is the magnetic field, and χ is a second order tensor referred to as the susceptibility. If χ is negative, the material is diamagnetic (halite, NaCl, is an example) and if χ is positive, the material is paramagnetic (for example, iron-rich olivine or fayalite, Fe_2SiO_4).

Scientists no longer attribute the cause of permanent magnetism to a soul, but instead attribute it to exchange energy. A permanent magnetic order results from exchange energy, which combines Coulomb interaction energy with the Pauli exclusion principle. Thus, exchange energy can only properly be understood through quantum mechanics. Exchange energy is often calculated by evaluating the nature of overlap of electron orbitals. Depending on the details of the electron overlap, a minimum in exchange energy sometimes requires that adjacent atoms have parallel magnetic moments and the material is referred to as ferromagnetic. With different overlap, the minimum in energy occurs when the adjacent magnetic moments have opposite sign. Then the material is described as antiferromagnetic when the moments are of equal magnitude and ferrimagnetic when the adjacent magnetic moments differ in magnitude. The best-known example of a ferrimagnetic mineral is magnetite (Fe_3O_4). Magnetite is said to have an indirect exchange energy because the coupling of adjacent iron atoms occurs through intervening oxygen atoms.

As the temperature of a material is increased the thermal energy (primarily recorded in quantized lattice vibrations referred to as phonons)

increases and eventually overwhelms the exchange energy. The Curie temperature is the highest temperature a ferromagnetic material can possess a magnetic structure in the absence of an external magnetic field. The analogous permanent loss of magnetic order in antiferromagnetic and ferrimagnetic structures occurs at the Néel temperature. (Some paleomagnetists also refer to this as the Curie temperature.) The saturation magnetization monotonically increases on cooling from the Curie or Néel temperature to absolute zero providing no phase change occurs on cooling. The Curie temperature at ambient pressure of iron, a ferromagnetic material, is 1043 K and the Néel temperature of ferrimagnetic magnetite is 853 K. Ilmenite ($FeTiO_3$) is an example of an antiferromagnetic substance and it has a Néel temperature of 40 K. It is useful to recognize that the melting temperature of a magnetic material always exceeds the Curie or Néel temperature. (So-called magnetic fluids contain suspended solid magnetic material.) Because the electron overlap is a function of pressure, the Néel and Curie temperatures are also functions of pressure. Physics and engineering aspects of magnetism are summarized in books such as Mattis (1988) and Hubert and Schäfer (1998).

Remanent magnetizations

Remanent magnetization (RM) is what is meant by most people when they refer to "permanent magnetization." An RM is defined as the magnetization that is present in a material in the absence of an external magnetic field. One of the prime goals of rock magnetists is to explain the properties and origins of various forms of RM. Of particular interest is the origin of RM that was acquired under natural conditions, natural RM (NRM).

A particularly useful way to gain insight into RM is through an oversimplified model involving a large ensemble of identical uniformly magnetized particles that are noninteracting. (These particles would correspond to individual magnetic mineral grains in a rock.) We assume there are only two assessable minimum energy states, E_u and E_d, of equal magnitude (in the absence of an external field) in which the magnetization is, respectively, in the up or down direction. There is an energy barrier separating these two states of magnitude E_B. In equilibrium and in the absence of an external field one expects both states to be occupied by the same number of magnetic particles. The material, which we will subsequently refer to as rock, is then said to be demagnetized. Let us apply a very large external magnetic field in the up direction. We take this field to be so large that all the particles become magnetized up. When the external field is removed the majority of the particles will remain in E_u. (All the particles would be in E_u if the experiment were carried out at absolute zero temperature where thermal fluctuations could be ignored.) The sample now has an RM referred to as a saturated isothermal RM (SIRM). If we had used a smaller, but still strong, external field so that there were some particles still in E_d after the external field was applied, then the resulting RM would be referred to as an IRM. Consider yet a different thought experiment in which we start with a demagnetized rock and apply a weak field such that $\mathbf{m}\cdot\mathbf{H}$ (where $\mathbf{m}$ is the magnetic moment of a particle) is smaller than E_B. With time thermal fluctuations may displace some of the particles from E_d to the minimum energy state E_u. The magnetization of the rock acquired over time in a magnetic field is referred to as a viscous RM (VRM) acquired at temperature T. If T is not explicitly given, the VRM is assumed to have been acquired at ambient temperature.

There are many types of RM, far more numerous that can be reviewed here. However, rock magnetists are often interested in distinguishing between a primary RM, one acquired when the rock formed, from a secondary RM formed later. The most common forms of primary RM of interest to paleomagnetists are TRM, DRM, and postdepositional DRM. Thermal RM (TRM) is the primary RM acquired by an igneous rock when it cools from the Curie or Néel temperature to room temperature in a weak field, such as that of Earth's magnetic field. Detrital RM (DRM) is acquired by sediments as they settle out of a quiet fluid environment, such as a lake. Postdepositional DRM seems to be the predominant mechanism by which a primary RM is acquired by marine sediments. Mixing, often by marine organisms, and compaction typically occurs in the sediments closest to the surface in a marine environment. The primary RM, a postdepositional DRM in this case, is acquired at a depth in the sediments. The depth of acquisition varies depending on the type of sediment and its physical and biological environment. Postdepositional DRM also can, and sometimes does, occur in lakes.

Similarly there are many types of secondary RM such as a VRM or an IRM. One of the most common forms of secondary RM is a chemical RM (CRM) usually defined as any RM acquired during chemical change below the Curie or Néel temperature. Some scientists use a more restricted definition of CRM to mean that RM acquired during the growth of a mineral in a magnetic field (CRM then refers to crystalline RM). Unfortunately, this ambiguity in definition of CRM is not always contextually obvious. There are more than 30 different types of RM that have been introduced into the literature, a dozen or so of which are commonly used.

There are two other terms that are useful to introduce and are common to those scientists who have worked with magnetic hysteresis. The bulk coercive force is the magnitude of a field that is applied in the opposite direction to the magnetization to reduce the magnetization to zero. The remanent coercive force is equal to or larger than the bulk coercive force; it is the magnitude of the field applied to a sample in the opposite direction to its RM that will leave the sample demagnetized after the external field is removed. The bulk coercive force and the remanent coercive force provide somewhat different measures of the stability of the RM with respect to an external magnetic field.

Anisotropy

It is important to recognize that the presence of an RM in a sample is a nonequilibrium process that requires magnetic anisotropy. This is manifested in the thought experiment used above. In the absence of an external magnetic field, the particles in the rock example considered possess uniaxial anisotropy: there is an easy axis of magnetization parallel to the magnetization of the grain and a plane of hard directions perpendicular to the easy axis. In the above example discrete energies were used, but in an actual grain it would be possible for the magnetization to be in a direction other than an easy axis in the presence of an external field but not otherwise. (We exclude the possibility of the magnetization residing in the metastable hard direction because thermal fluctuations would quickly lead to the magnetization changing to the easy axis, except close to absolute zero.) Note that the equilibrium state in zero external field is the demagnetized state. If there is no anisotropy, there is no energy barrier separating minimum energy states and thermal fluctuations would quickly reduce the magnetization to zero.

Although magnetic anisotropy at the grain level is a necessary condition to have a remanence, it is also important to recognize that a rock can be magnetically isotropic and carry an RM. For example, if the particles discussed above (each of which is by itself magnetically anisotropic) were randomly orientated, the rock would be isotropic. The most common extrusive rock, basalt, is typically isotropic while other igneous rocks sometimes exhibit magnetic fabrics and thus are anisotropic.

The basic underlying mechanisms that produce magnetic anisotropy in a grain at the microscopic level include dipole-dipole interaction and most importantly the coupling of unquenched orbital moments with spin. However, a continuum approach is applied in rock magnetic calculations that use phenomenological equations to describe anisotropy. Magnetostatic, magnetostriction, shape, and exchange are explicitly described by equations that are not strictly valid at the microscopic level. They probably are valid down to a scale size comparable to that applicable to reconstructed surfaces in solids; i.e., a size of ten to several tens of angstroms. Scientists that claim accuracy below a 100 Å or so using a continuum approach might wish to investigate their assumptions closely. The external part of the magnetostatic

energy is the energy difference of a material in zero external field and in the presence of an external field. The internal part of the energy is most commonly referred to as the demagnetization energy. It can be derived from the constitutive equation

$$\mathbf{B} = \mu_0 \mathbf{H} + \mathbf{M},$$

where $\mathbf{B}$ is the magnetic induction field and μ_0 is the free-air permeability. Using the fact that the divergence of $\mathbf{B}$ and the curl of $\mathbf{H}$ (in the absence of electric current and electric displacement current) are zero, it is straightforward to use the constitutive equation to derive Poisson's equation for a scalar potential in which the divergence of $\mathbf{M}$ acts as a magnetic charge density. This means that wherever the magnetization changes in direction or magnitude there is a bound magnetic charge. In particular, these charges are present on all grain boundaries for which there is some perpendicular component of the magnetization. Then the bound magnetic charges (analogous to electric charges on a capacitor) produce an internal field that has a component opposite to the magnetization. Because of this, the internal field is often referred to as the demagnetization field. The demagnetization field can result in a strong magnetic anisotropy. For example, the presence of a demagnetization field explains why it is typically much easier to magnetize a needle-shaped grain along its long axis than perpendicular to this axis.

The magnetocrystalline anisotropy energy is represented in the uniaxial case by

$$E_K = K \sin^2 \theta,$$

where K is the anisotropy constant and θ is the angle between the easy anisotropy axis and the magnetization. The larger K the more difficult it is to reverse the magnetization. Additional anisotropy constants are used for most materials, such as cubic magnetite for which two anisotropy constants are commonly employed. These constants are usually empirically determined rather than calculated from first principles.

The ordering of magnetic moments in a material results in a stress that produces strain, referred to as magnetostriction. Because stress and strain are second order tensors, the equations for magnetostriction can be complicated. Not only do they depend on crystallography, but they also must be able to accommodate additional sources of stress, such as associated with dislocations. One of the simplest examples is the equation for energy applicable to isotropic magnetostriction in which the magnetization and strain are measured in the same direction

$$E_\lambda = (3/2)\lambda\sigma V \sin^2 \alpha,$$

where the stress σ is a tension applied in the direction of the magnetization and λ is the magnetostriction constant, V is the volume, and α is the angle between the easy magnetostrictive anisotropy axis and the magnetization. Note that in this case the equation for magnetostriction energy is of the same form as that given for the uniaxial magnetocrystalline anisotropy. Most situations are more complicated and additional magnetostriction constants are introduced to describe experimental results.

Although the exchange energy is purely isotropic, it can result in anisotropy when two or more phases are present. An example is when an antiferromagnetic phase with a relatively high Néel temperature is coupled through exchange to a ferromagnetic phase with a lower Curie temperature. In this case there is a uniaxial anisotropy in the ferromagnetic material that has an easy axis aligned with the directions of the antiferromagnetic moments.

Self-reversal

An isotropic rock will usually acquire an RM parallel to the external field. However there are circumstances for which a rock can acquire an RM antiparallel to the field and when such circumstances occur the rock is said to have self-reversed. Néel presented the first mechanisms for self-reversal in the mid-1950s and shortly thereafter Nagata and Uyeda discovered the first reproducible self-reversing rock, the Haruna dacite. Self-reversal always involves two magnetic phases. The first phase acquires an RM parallel to the external field. An antiparallel coupling to a second phase produces an RM opposite to the external field. If the magnetic moment of the second phase exceeds that of the first phase at room temperature, then a self-reversal will have occurred. The negative coupling between the two phases can be cause by exchange interaction (as is the case for the Haruna dacite) or by magnetostatic interaction. Another process that can lead to self-reversal involves an order-disorder transition. For example, suppose the collective magnetic moment of cations at lattice site A is greater than at lattice site B at elevated temperature where a material is disordered. Further suppose that the exchange coupling between the two sites is negative (antiferromagnetic). If on cooling the material becomes an ordered one with the dominant magnetic moment now being that of site B, then a self-reversal will have occurred.

Demagnetization

There are several different demagnetization procedures that can be employed to bring a rock to a demagnetized state (defined above in the section entitled remanent magnetizations). An RM has a relaxation time τ that is useful to describe the decay of an initial magnetization M_0 with time t:

$$M = M_0 \mathrm{e}^{-t/\tau}.$$

In actual rock samples there typically is a range of relaxation times that correspond to the fact that there are many contributions to anisotropy energy. These relaxation times are functions of many intrinsic variables (associated with the anisotropy energies) and extrinsic variables, such as magnetic field, stress, and temperature. Demagnetization procedures provide information on the sensitivity of magnetic relaxation to these extrinsic factors. A magnetic component is said to be stable or locked in to a sample when it has a long relaxation time with respect to the time of interest to the investigator.

Only the two most commonly employed demagnetization methods will be mentioned here. The first is thermal demagnetization that measures the sensitivity of the sample to temperature. A complete thermal demagnetization of a sample can occur by heating the sample to a temperature exceeding its Curie or Néel temperature and cooling the sample back to room temperature in the absence of an external magnetic field. Partial thermal demagnetization occurs when the sample is heated to some temperature T that is lower than the Curie or Néel temperature and then cooled to room temperature in zero external field. The magnetization that is demagnetized by the last process is referred to as being unblocked at T. In igneous rocks it is often found that a TRM consists of independent components of magnetization that are locked into the rock during cooling at different temperatures. These components can be unlocked by progressively thermally demagnetization of a sample. This is the process by which a sample is partially demagnetized in a series of experiments in which the peak demagnetization temperature is sequentially increased. (This procedure is sometimes referred to as the progressive method and it is the one most commonly employed. There also is a continuous method in which the RM is measured while the sample is still hot.) The unblocking temperature is typically assumed to be the blocking temperature, that temperature at which the component of magnetization was locked into an igneous rock during cooling. Although it is well known by modern rock magnetists that the unblocking and blocking temperatures are not usually identical, the difference is often negligible for practical purposes (especially for single domain grains defined in the next section). Thermal demagnetization is a measure of the instability of the magnetization as a function of temperature and it often provides valuable information of a sample even when the magnetization is not a TRM.

The second method discussed here is alternating field (AF) demagnetization. This method involves the gradual decrease of an alternating (often at 60 Hz) magnetic field from some peak value H_p to zero. The preferred AF demagnetization method also randomly tumbles the sample with respect to the external field. Those components of magnetization with relaxation times that are small with respect to some characteristic time of the experiment (associated with the rate the alternating field is decreased) are thought to be randomized by this process. Usually AF demagnetization employs a sequence of increasing values for H_p.

Most paleomagnetists use thermal demagnetization, which provides information on the stability of magnetization with respect to temperature, and AF demagnetization, which provides information on the stability of the magnetization with respect to alternating magnetic fields, to infer stability of magnetization in a rock sample with time. The magnetic components that are most stable with respect to temperature or alternating magnetic fields are believed to be the most probable carriers of the primary RM. However, paleomagnetists are well aware that this is not always the case, for example when the sample has acquired a particularly stable CRM. Thus numerous experiments are undertaken to determine the primary RM. There are no hard and fast rules to do this and undoubtedly mistakes are made. For such reasons consistency of a variety of data and interpretations are sought and rock magnetism remains a vibrant field of intellectual endeavor.

Magnetic structure

The structure of magnetic grains depends on many factors including mineralogy, grain size, grain shape, and defects. Grains are classified for a fixed mineralogy as superparamagnetic (SP), single domain (SD), pseudo-single domain (PSD), and multidomain (MD). The smallest are the uniformly magnetized SP grains that have short relaxation times (usually less than 10 s or so). These grains do not contribute to the remanent magnetization but they do affect the susceptibility. SD grains are also uniformly magnetized and can exhibit relaxation times from the largest SP grains to times that exceed the age of Earth (4.6 billion years). PSD grains have the poorest defined structures that range from slight deviations from a SD structure to small multidomain grains. MD grains are grains that contain uniformly magnetized regions, called domains that are separated from each other by transition regions referred to as domain walls. A domain wall is referred to as an x wall, where x is the number of degrees required by the gradual rotation of magnetic moments in the wall to accommodate the magnetization in the adjacent domains. For example, a 180° domain wall separates domains with opposite magnetizations, while a 70° wall is a transition of magnetic moments between two magnetic domains that have magnetic directions that differ by 70°. MD grains are often classified on the basis of the number of domains they have. For example, a two-domain grain has two oppositely magnetized domains separated by a 180° wall.

Micromagnetic calculations minimize the exchange and anisotropy energies to determine the equilibrium states available to a grain. The structures found this way can be compared to those found by various imaging techniques, such as magnetic force microscopy. One finds that there is often more than one magnetic structure that a grain can have depending on its magnetic history. These different structures reflect different local energy minimum or LEM states. Let us consider what happens to an initial SD grain of magnetite as its size is increased. We will assume the grain is a cube and use one side to indicate its size. The SP-SD threshold at room temperature is near 0.045 μm, the SD-PSD is near 0.05 μm, and there is no agreed upon PSD-MD threshold size. This lack of agreement on the PSD-MD transition probably reflects that the transition is a gradual one, although some investigators using a hysteresis parameter definition put this size around 15 μm. The largest PSD domains have several magnetic domains, but they exhibit different stability properties from large MD grains. A reference to a PSD grain or PSD behavior can be confusing because there are incompatible definitions of them that are still commonly used.

It needs to be pointed out that one might find a SD magnetite with a size of say 0.06 μm at room temperature. However, this would presumably not reflect a global minimum energy state. In the case of magnetite the curling, also called vortex, state would have a lower energy at this size. Vortex and flower states, names that reflect the magnetic structure, are the most common states calculated for the smallest PSD grains. A given size grain can exhibit more than one domain structure depending on the circumstances under which the grain became magnetized. Further discussion of this subject can be found in Dunlop and Özdemir (1997).

Magnetic mineralogy

Although the elements Fe, Co, and Ni are ferromagnetic, only Fe plays a prominent role for magnetic properties in minerals and rocks on Earth. Pure iron is the primary phase responsible for remanence on the moon and Fe-Ni alloys are common in meteorites. However, on Earth the most common forms of remanence are found in compounds of iron such as iron oxides, iron-titanium oxides, iron oxyhydroxides, and iron sulfides. There are also other less common systems, such as the solid solution series Mn_3O_4-Fe_3O_4 (end members hausmannite and magnetite and intermediate members collectively called jacobsite) in which the peak in saturation magnetization occurs when Mn_3O_4/Fe_3O_4 is around 16.7%. The most commonly studied solid solution series are those of titanomagnetites, FeO-Fe_3O_4 with end members wüstite and magnetite, and titanohematites, $FeTiO_3$-Fe_2O_3, with end members ilmenite and hematite. Low temperature oxidation of titanomagnetites produce γ phases (titanomaghemites) while high temperature oxidation includes titanohematites as products. For instance, Fe_3O_4 is oxidized to cubic maghemite, γFe_2O_3, at room temperature and to rhombohedral hematite, αFe_2O_3, at say 900 K. The magnetic properties vary significantly with changes in composition. The magnetic properties of hematite will be briefly discussed to illustrate some of the complexities associated with magnetic mineralogy.

Hematite is an antiferromagnetic substance that contains a parasitic ferromagnetism and thus it possesses a different magnetic order than given earlier in the oversimplified description of the origins of magnetic order. It is well known that alternating basal planes in hematite are antiferromagnetically coupled. There is a slight canting of the magnetic moments in these planes such that the moments in alternating planes are not precisely 180° apart. This implies that there is a weak, or parasitic, ferromagnetism that is perpendicular to the ternary axis. In addition, hematite sometimes displays a defect moment in which defects occur more commonly on alternating planes and thereby produces a ferrimagnetic-like moment that is nearly perpendicular to the spin-canted moment. The magnetocrystalline anisotropy of hematite changes sign near 258 K, the Morin transition, and below this temperature the ternary axis (perpendicular to the basal plane) becomes the easy axis. Only the defect moment is present below the Morin temperature. Because of the defect moment the saturation magnetization of hematite is somewhat variable with magnitude around 1/200 of that of magnetite at room temperature (the latter is $480 \times 10^3\,A\,m^{-1}$). Interestingly some intermediate values of titanohematites reach saturation magnetization values that are a significant fraction of that for magnetite. Although this brief discussion of hematite is far from exhaustive, it should be sufficient to illustrate the complexity of magnetic mineralogy and the prominent role such mineralogy plays in the understanding of magnetic properties of rocks.

Some applications

Magnetic minerals are very sensitive to oxidation conditions. Because of this, iron titanium oxide assemblages in igneous rocks are sometimes used to estimate the oxygen fugacity and temperature in Earth's mantle. In partial contrast, it is the pE and pH that is often responsible for the equilibrium assemblages in marine sediments. Because of their sensitivity to climatic conditions, magnetic minerals in sediments are

sometimes used as proxies for paleoclimatic variation. For similar reasons magnetic minerals are sensitive to man-induced changes and this has led to the field of environmental magnetism. Such studies are complicated by the fact that microbes can also mobilize some cations, including Fe, in sediments. In addition, some microbes such as magnetotatic bacteria produce chains of SD magnetite within their cells and appear to use this magnetite to determine the vertical direction in mud where they are neutrally buoyant. The microbe examples reflect the use of rock magnetism in the fields of geobiology and biomagnetism. Magnetic properties such as susceptibility, remanence, and magnetic phase transitions are often used to correlate sedimentary layers in magnetostratigraphy. Paleoflow directions of fluids are sometimes estimated from the magnetic fabric of rocks. Finally, the most common uses of rock magnetism are in paleotectonic and paleogeomagnetic studies.

Ronald T. Merrill

Bibliography

Dunlop, D., and Özdemir, Ö., 1997. *Rock Magnetism: Fundamentals and Frontiers.* Cambridge: Cambridge University Press, 573 pp.

Hubert, A., and Schäfer, R., 1998. *Magnetic Domains: The Analysis of Magnetic Microstructures.* New York: Springer-Verlag, 696 pp.

Mattis, D., 1988. *The Theory of Magnetism 1: Statics and Dynamics.* New York: Springer-Verlag, 300 pp.

Cross-references

Biomagnetism
Demagnetization
Iron Sulfides
Magnetic Anisotropy, Sedimentary Rocks and Strain Alteration
Magnetic Domain
Magnetization, Chemical Remanent (CRM)
Magnetization, Isothermal Remanent (IRM)
Magnetization, Natural Remanent (NRM)
Magnetization, Remanent, Application
Paleomagnetism

ROCK MAGNETISM, HYSTERESIS MEASUREMENTS

Use and scope of hysteresis measurements

The term hysteresis in general describes that an effect is lagging behind its cause (from greek $\upsilon\sigma\tau\epsilon\rho\epsilon\iota\nu$: to lag behind). More specifically, magnetic hysteresis is a property of all ferromagnetic materials (in sensu lato) causing the magnetization of such a material to be strongly dependent on its magnetic history, i.e., exposure to an external magnetic field.

Practical description of magnetic hysteresis

In order to obtain a complete hysteresis loop, the magnetization **M** of a sample is measured as a function of an external inducing field **B** which is cycled from zero to the maximum positive value, back to zero, up to the maximum negative value and then back again to the maximum positive value. Magnetization is generally measured only in the direction of the inducing field so that both quantities are treated as scalars.

The most simple hysteresis measurement of a rock is performed with a set of two concentric coils of which one is inducing the external field B (Figure R9). The magnetic moment of the rock is generating a magnetic stray field which, when the sample is pulled out from the set of coils, in turn induces a voltage pulse in the second (measurement) coil. This induction pulse is a direct measure for the magnetization

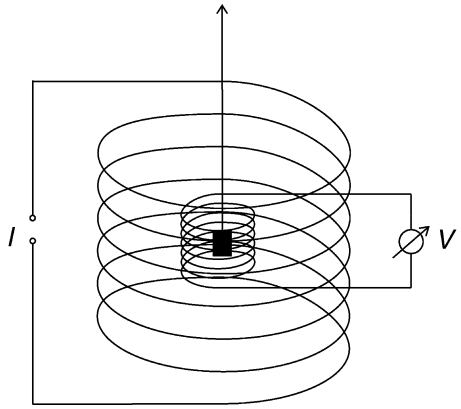

Figure R9 Schematic drawing of a simple hysteresis measurement.

of the sample for a given external field step. The whole procedure can then be repeated for a sufficient number of field steps to obtain the hysteresis loop.

Rocks generally present a mixture of different minerals. Some of these minerals (in most cases ore minerals containing iron) form a long range ferro-, ferri-, or antiferromagnetic spin order below their critical Curie or Néel temperature. In this ordered state the volume dV at r carries a spontaneous magnetization $M(r)$. In most materials $M(r)^2 = M_s^2$ is constant. Within a given external field $B(r)$ and stress tensor $\sigma(r)$ the magnetization structure $M(r)$ adjusts itself into a local minimum of the total magnetic energy $E(M(r), B(r), \sigma(r))$ which encompasses exchange, anisotropy, demagnetizing, magnetoelastic, magnetostrictive, and external field energy.

During an isothermal external field variation the magnetization change of such a system usually lags behind the field change which is expressed in the term "hysteresis." If the field amplitude B_{max} in measuring a hysteresis loop is sufficiently large, this loop defines four basic quantities (Figure R10) (1) the saturation magnetization M_s is the maximal magnetization of the ordered phase within any external field, (2) the saturation remanence M_{rs} is the maximal magnetization of the sample in zero field, (3) the coercive field B_c is the maximal field where zero magnetization of the ordered phase is possible, and (4) the total hysteresis work E_{hys} corresponds to the area inside the hysteresis loop. The coercivity of remanence B_{cr} is the counter field necessary to remove the saturation remanence. It cannot be directly read from the hysteresis loop but requires an additional measurement.

Most rocks also contain paramagnetic minerals, i.e., minerals containing ions with permanent magnetic moments which are not forming a long range spin order. As these minerals cannot carry a remanent magnetization, they do not contribute to M_{rs}, B_c, or E_{hys}. However, they do contribute to the induced magnetization $\mathbf{M}_i = \chi_p(1/\mu_0)\mathbf{B}$, where χ_p is the paramagnetic susceptibility. χ_p is independent of B in the field range typically used for hysteresis measurements. It thus defines the slope of the hysteresis loop above the field where the ordered phase saturates. The paramagnetic contribution has to be subtracted to determine the saturation magnetization of the ordered phase (Figure R10). Another contributor to the field independent susceptibility in rocks are diamagnetic minerals, e.g., quartz.

Definitions and units for magnetic quantities

Much confusion in rock magnetism arises from the fact that the older system of cgs units is still used in many publications besides the now recommended SI units. Table R4 shows the basic magnetic quantities, their units in the cgs and SI system, and the conversion factors. In the SI system the following applies for the relation between magnetic induction **B** and magnetic field **H**

$$\mathbf{B} = \mu_0(\mathbf{H} + \mathbf{M}) \qquad \text{(Eq. 1)}$$

with $\mu_0 = 4\pi \times 10^{-7}\,\mathrm{V\,s\,A^{-1}\,m^{-1}}$ being the magnetic permeability of vacuum.

Note, that for convenience in the case of $M = 0$, i.e., outside a sample, the term "magnetic field" is also used for $\mathbf{B} = \mu_0 \cdot \mathbf{H}$.

Most measurement techniques for hysteresis curves determine the magnetic moment of a given sample which is then normalized either by sample volume V or sample mass m. $M = \mu/V$ is called the (volume) magnetization, whereas $\sigma = \mu/m$ is called the specific magnetization.

Use of hysteresis measurements

The shape of hysteresis loops measured on rocks is determined by several properties of the contained minerals: Among these are the type of spin ordering (i.e., ferro-, ferri-, and antiferromagnetic) or the absence of spin order (para- and diamagnetic), the grain size, grain shape, concentration, and also distribution of each contributing mineral. Due to the multitude of influencing factors, generally some additional information about the magnetic mineralogy is needed for the interpretation of hysteresis loops in rock magnetism. If such information is available, hysteresis loops allow a rapid characterization of samples regarding compositional variations, the stability of paleomagnetic information carried by the rocks, change of depositional regime in the case of sediments or alteration processes affecting rocks in general.

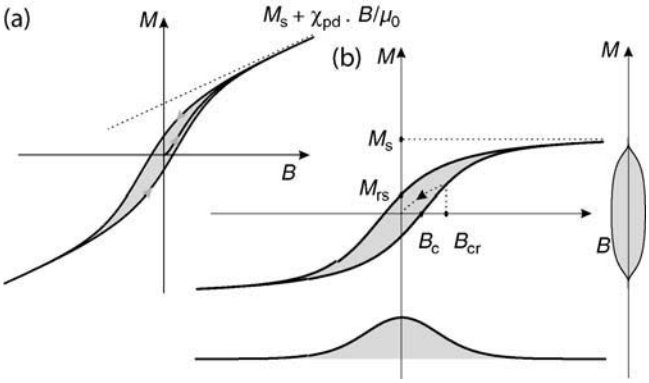

Figure R10 Measured hysteresis loops (a) contain para- or diamagnetic susceptibilities χ_{pd} from sample holder or admixtures which first must be removed to obtain the ferromagnetic loop (b). The coercive force B_c is defined by the zero crossing ($M = 0$) of the lower hysteresis branch, the saturation remanence M_{rs} is the magnetization of the upper branch at $B = 0$. The saturation magnetization M_s is obtained by estimating the limit value of the asymptotic approach to saturation. The coercivity of remanence B_{cr} is defined to be the field value at which switching off the field in course of the lower hysteresis branch would lead to zero remanence. Note that the susceptibility correction leads to different B_c values for (a) and (b), whereas M_{rs}, M_s, and B_{cr} are unchanged. Subtracting the hysteresis branches either in vertical direction or subtracting their average in horizontal direction leads to two representations of the coercivity distribution with respect to B or M. The shaded area in all cases is equal and represents the magnetic energy dissipation E_{hys} during one hysteresis run.

Physical mechanisms of hysteresis

Reversible and irreversible magnetization processes

Magnetic hysteresis is a result of irreversible magnetization changes. An abstract physical process between two states $A \rightarrow B$ is reversible if each intermediate state is arbitrarily close to an equilibrium state. In this case the cycle $A \rightarrow B \rightarrow A$ dissipates no energy. A simple mechanical example of an irreversible process is a switch (Figure R11). It is typical for any system which allows for irreversible changes. (1) It possesses two (or more) metastable positions separated by an energy barrier that must be overcome to change from one to the other. (2) The systems current state depends upon previous physical influences: it serves as a memory.

Natural magnetic systems usually contain a huge number of different metastable magnetization states which give rise to irreversible magnetization processes whenever external variables like magnetic field, temperature, or pressure change. These processes are usually very complex, but as was firstly shown in Stoner and Wohlfarth (1948), there is one important magnetic analog to the mechanical switch: a coherently rotating single-domain (SD) particle.

Single-domain particles

In sufficiently small magnetic particles, quantum mechanical exchange coupling keeps all spins aligned. The most simple case where the particle contains a single axis of preferred spin direction is discussed in many textbooks (Dunlop and Özdemir, 1997; Bertotti, 1998; Hubert and Schäfer, 1998). This is one of the few situations where a complete analytical treatment of magnetic hysteresis is possible. Most of our ideas on physical interpretation of hysteresis implicitly or explicitly are founded on this ideal situation. As sketched in Figure R12a, the magnetic energy of the particle varies during rotation of the magnetization. When a magnetic field $\mathbf{B}$ is applied, the particle behaves as a magnetic switch. When K denotes its uniaxial anisotropy constant

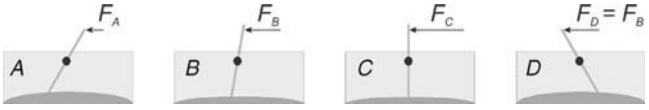

Figure R11 Reversible and irreversible physical processes in a switch. Slowly increasing the force between A and B is a reversible process through a series of well-defined equilibrium states. In contrast, the state transition from B over C to D is irreversible. There are no equilibrium states between C and D. Slowly decreasing the force in position D to the value at B does not reinstall the position of the switch.

Table R4 Units and conversion of magnetic quantities

Quantity	Symbol	SI units	cgs units	Conversion cgs ↔ SI
Magnetic induction	B	$\mathrm{T(Tesla) = V\,s\,m^{-2}}$	G (Gauss)	$1\,\mathrm{T} = 10^4\,\mathrm{G}$
Magnetic field	H	$\mathrm{A\,m^{-1}}$	Oe (Oersted)	$1\,\mathrm{A\,m^{-1}} = 4\pi \times 10^{-3}\,\mathrm{Oe}$
Magnetic moment	μ	$\mathrm{A\,m^2}$	$\mathrm{G\,cm^3}$	$1\,\mathrm{A\,m^2} = 10^3\,\mathrm{G\,cm^3}$
Magnetization	$M = \mu/V$	$\mathrm{A\,m^{-1}}$	G	$1\,\mathrm{A\,m^{-1}} = 10^{-3}\,\mathrm{G}$
Susceptibility	χ	Dimensionless	Dimensionless	$1(\mathrm{SI}) = 1/4\pi(\mathrm{cgs})$

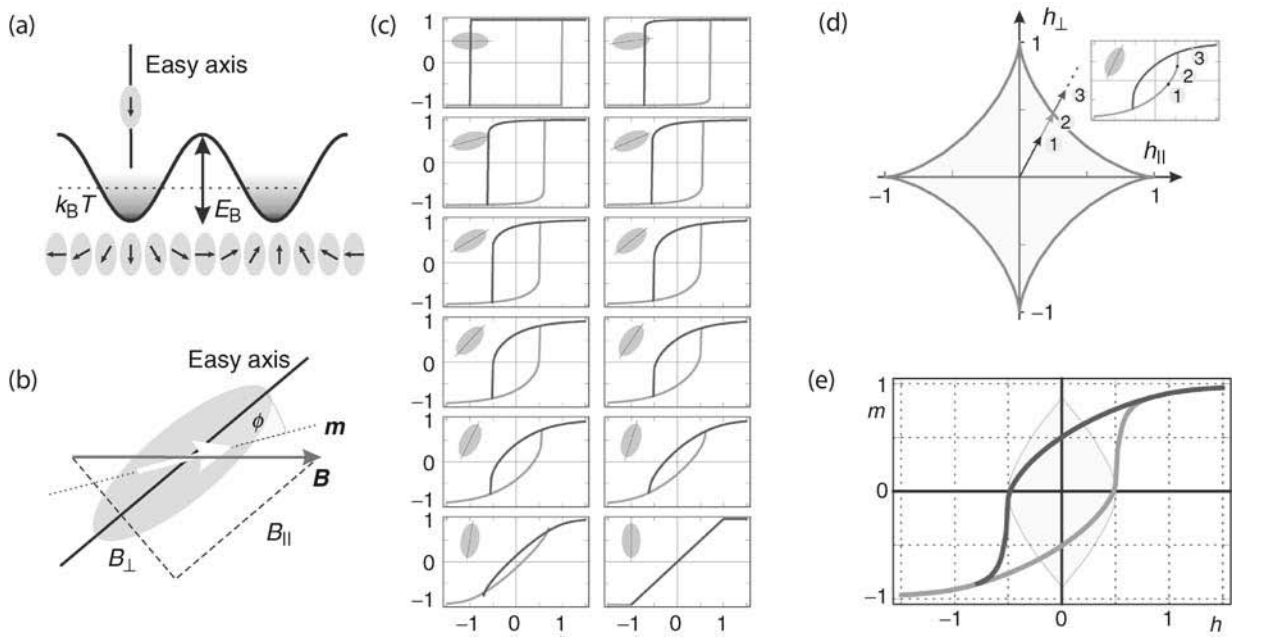

Figure R12 Stoner-Wohlfarth theory of hysteresis loops in coherently rotating single-domain particles. (a) Each particle has a preferred easy axis of magnetization and an energy barrier E_B opposes the rotation. It can result from magnetostatic-, crystal-, or stress-induced anisotropy. Thermal activation $k_B T$ is assumed to be small in comparison to E_B. (b) Application of an external field with components $B_{||}$ and $B_\perp$ with respect to the easy axis results in a magnetization deflection ϕ. (c) Plotting the magnetization component m_B versus B results in single particle hysteresis loops. Their shape depends upon the angle between easy axis and external field B. (d) The switching instability traces an asteroid in the $h_{||} - h_\perp$ space. For field vectors inside the asteroid the system is bistable, outside the asteroid the magnetization state is unique. (e) Averaging over an isotropic ensemble of identical single-domain particles results in the shown Stoner-Wohlfarth hysteresis loop. More realistic ensembles average in addition over a distribution of anisotropy constants.

and M_s its spontaneous magnetization, the particles' energy as a function of the deflection angle φ is given by

$$e(\varphi) = K \sin^2 \varphi - \mu_0 B_{||} M_s \cos \varphi - \mu_0 B_\perp M_s \sin \varphi. \qquad \text{(Eq. 2)}$$

Solving the system of equations $e'(\varphi) = e''(\varphi) = 0$, yields a parametrization of the critical line in field space where the magnetization becomes unstable and switches direction

$$h_{||}^* = -\cos^3 \varphi, \quad h_\perp^* = \sin^3 \varphi,$$

where $h = BM_s/(2K)$ is the normalized field strength and φ serves as parameter. This curve is the Stoner-Wohlfarth asteroid (Bertotti, 1998; Hubert and Schäfer, 1998) (Figure R12d).

Plotting the magnetization component parallel to the field versus the field yields the Stoner-Wohlfarth hysteresis loops in Figure R12. For simple numerical mixing experiments, a useful approximation for a Stoner-Wohlfarth particle ensemble is $m_{SW}(h) = \tanh(0.8h) \pm 0.5\,\mathrm{sech}(1.9h)$.

Hysteresis in multidomain particles

In magnetic particles beyond the critical SD size, magnetostatic self-interaction overcomes the strong quantum mechanical exchange coupling and deflects a part of the spins to form an inhomogeneous internal magnetization structure which minimizes the energy by partial magnetic flux closure. In large particles the optimal magnetization configuration is a subdivision of the grain in different relatively large magnetic domains, nearly homogeneously magnetized along some preferred axes and separated by relatively small domain walls wherein the magnetization changes continuously. To a certain extent, it is easy to change the magnetization of a multidomain grain by moving its domain walls such as to enlarge one domain and diminish another (Figure R13). One mechanism of hysteresis in multidomain grains originates from impeding the continuous motion of a domain wall by pinning it to a local defect or stress source which creates an energy barrier which must be overcome to proceed with the motion. By larger field variation, the energetically optimal number of domains changes and a global reorganization of domain structure occurs by nucleation or denucleation of domains. In all these cases, one can envisage the self-demagnetizing field as the driving force which adjusts the internal structure to the prescribed external field. Only beyond the saturation field B_{sat}, the internal magnetization structure is homogeneous and essentially rotates like an SD particle into the field direction. Because this rotation is a reversible process, the branches of the hysteresis curve coincide for $B > B_{sat}$.

While a quantitative description of the physical processes in multidomain particles is extremely difficult, a general understanding of multidomain hysteresis in terms of the self-demagnetizing field H_d, as given by Néel (1955), is very easy. In this simplified picture the MD particles' average magnetization M creates an average internal demagnetizing field

$$H_d = -NM,$$

where the numerical demagnetizing factor $0 < N < 1$ nearly does not depend on the domain configuration. The total internal field H_i inside the particle then is the sum $H + H_d$ of external and demagnetizing field. Assuming that anhysteretic magnetization and internal field are linked by an internal susceptibility χ_i one obtains

$$M(H) = \chi_i H_i = \chi_i (H + H_d) = \chi_i (H - NM(H)).$$

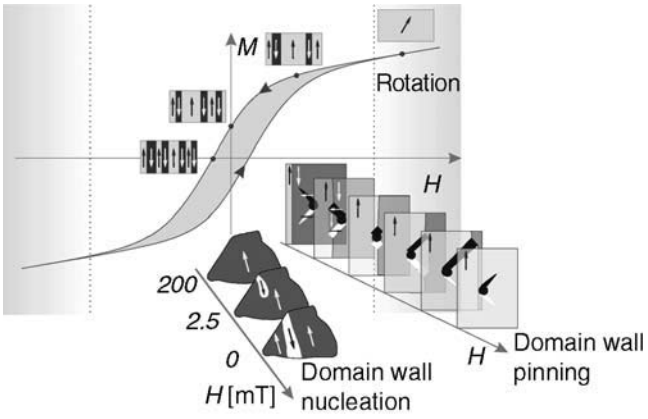

Figure R13 Hysteresis in multidomain particles is effected by changes of the domain structure. Domains grow or shrink by domain wall movement which can be impeded by pinning at lattice defects. An example is irreversible pinning of a 180° domain wall as observed in a single crystal iron film (after Hubert and Schäfer 1998). Changing the number of domains requires global reorganization of the magnetization pattern (nucleation). For example nucleation of domains as observed in a 15-μm titanomagnetite (after Halgedahl and Fuller 1983). In high fields the sample becomes saturated with essentially homogeneous magnetization which in increasing field rotates toward the field direction.

Solving for $M(H)$ yields

$$M(H) = \frac{\chi_i}{1 + N\chi_i} H \approx H/N,$$

where the last approximation assumes large χ_i. For given H_c, the two hysteresis branches then are $M^{\pm}(H) \approx (H \mp H_c)/N$, from which for $H = 0$ Néel (1955) obtains

$$\frac{M_{rs}}{M_s} = \frac{1}{NM_s} H_c. \qquad \text{(Eq. 3)}$$

Overview of typical measurements

Instrumentation

There are two commonly used techniques to measure the magnetization of a sample in dependence of an applied field.

Firstly, magnetization can be determined by measuring the stray field generated by the magnetic moment of a sample. Commonly used instruments in rock magnetism applying this principle are vibrating sample magnetometers (VSMs). During the measurement the sample is vibrating and its magnetization is registered by measuring the flux change of the magnetic field through a system of pickup coils. The inducing external field is homogeneous and constant through time and therefore does not contribute to the measurement signal. One of the advantages of VSMs is the quick magnetization measurement, which allows to sample the hysteresis loop with typically up to 1000 evenly distributed data points. Despite this large number, measurement of a complete hysteresis loop typically does not take longer than one minute. Other instruments use superconducting quantum interference devices (SQUIDs) to measure the stray field of a magnetized sample. These devices are more common in the measurement of remanent magnetization but can also be used for measuring magnetization in applied fields. This technique is realized in the magnetic property measurement system (MPMS).

The second class of instruments measures the force which is exerted by a magnetic gradient field on the magnetized sample in order to determine its magnetization. The classical instrument using this technique is the magnetic balance. Here, the sample is suspended from a force measuring system and is positioned between the pole pieces of the electromagnet generating the inducing field. In order to generate a measurable force, the sample is not positioned in the area of homogeneous magnetic field but rather at the edges of the pole pieces where a large field gradient is present. Another frequently used configuration involves pole pieces which are shaped in a special way so that the inducing field is not homogeneous but has a well-defined gradient which is exerting a translational force on the sample (Collinson, 1983). The field gradient is generally dependent on the strength of the inducing field **B** so that the measurement of **M** is not independent of **B**.

This disadvantage of the magnetic balance can be overcome by separating the source of the gradient field from the inducing homogeneous field. The variable field translation balance (VFTB), a modified magnetic balance, uses this approach by supplying the gradient field through an additional set of coils. In addition, this gradient field is oscillating, forcing the sample to oscillate as well. Thus, the force acting onto the sample and eventually the magnetization can be determined dynamically from the sample's oscillation amplitude. This yields a higher sensitivity in comparison to the static force measurement of the classical magnetic balance. A similar approach is used in the alternating gradient field magnetometer (AGFM) where the sample is mounted on a quartz rod, which itself is attached to a piezoelectric transducer recording the force acting on the sample.

Measurement procedures

The basic interpretation of hysteresis properties requires determination of the four parameters saturation magnetization M_s, saturation remanence M_{rs}, coercive field B_c, and coercivity of remanence B_{cr}. The first three quantities are determined from the hysteresis loop, whereas B_{cr} can only be determined from the so-called backfield curve.

Measurement procedures for hysteresis loops depend on the speed of data acquisition and thus the number of data points. For instruments like the VSM and AGFM with typically 600–1000 data points per loop, field steps are chosen equidistantly to obtain a quasicontinuous loop. In the case of instruments with slower data acquisition and typically 20–40 field steps (e.g., VFTB, MPMS), nonequidistant spacing is advisable in order to properly sample all features of the loop shape.

von Dobeneck (1996) proposed the following series yielding increasing field increments toward the field maxima

$$B(i) = \frac{|i|}{i} \frac{B_{max}}{\lambda} [(\lambda + 1)^{|i|/n} - 1]$$

with $i = -n, \ldots, -1, 0, 1, \ldots, n$ ($2n$ number of data points per branch) and $\lambda > 0$ defining the accumulation of field steps toward the origin. This provides a good sampling of the bends in the region of irreversible magnetization changes and a less dense spacing in the region of the approach to saturation.

As magnetic hysteresis is temperature dependent, a proper temperature control during hysteresis loop measurement is crucial to obtain high-quality data.

For measurement of the backfield curve the sample is first brought into magnetic saturation by applying the maximum magnetic field in positive field direction. The sample's remanent magnetization is then measured in zero field being equal to M_{rs}. Subsequently, successively higher fields are imparted in negative field (or backfield) direction and after each field-on step, the remanent magnetization is again measured in zero field. The field at which the remanent magnetization switches from positive to negative values is called the coercivity of remanence B_{cr}. As the backfield measurement always consists of discrete steps, the crossing of the abscissa is usually determined by interpolation.

For instruments where the inducing field is generated by an electromagnet with pole pieces, it is necessary to compensate the residual magnetic field of these pole pieces in order to conduct a proper zero field measurement. Usually, this is accomplished by an additional set of coils.

Typical measurement results

Some results of hysteresis loop measurements and associated backfield curves are shown in Figure R14. The loop of synthetic MD magnetite (Figure R14a) shows the typical ramp-like shape and a quick saturation below 500 mT. Note also the comparatively low B_c of 3.5 mT and the small area inside the loop corresponding to a small E_{hys}. The high B_{cr}/B_c ratio is characteristic for multidomain particles. The young ocean basalt sample (Figure R14b) has a fairly low B_c as well. For the herein contained titanomagnetite, however, much higher fields are necessary for magnetic saturation. Although irreversible processes (causing the difference between the two loop branches) do not occur above $B \approx 0.4$ T, the loop shows significant curvature up to fields of 1.4 T due to reversible rotation of magnetic moments. Older ocean basalts, where titanomagnetite is transformed into titanomaghemite by low-temperature oxidation often show almost perfect single-domain behavior as represented by the hysteresis loop in Figure R14c. Both the M_{rs}/M_s and B_{cr}/B_c ratio are approaching the ideal values for noninteracting uniaxial single-domain particles (see Table R5). Natural titanomaghemites as found in ocean basalts have even higher saturation fields than titanomagnetites.

The grain size dependence of hysteresis loops and parameters will be discussed in the following section. More hysteresis loops of rock forming minerals can be found in the literature, e.g., Chevallier and Mathieu (1943) (Hematite) and Keller and Schmidbauer (1999) (Titanomagnetite).

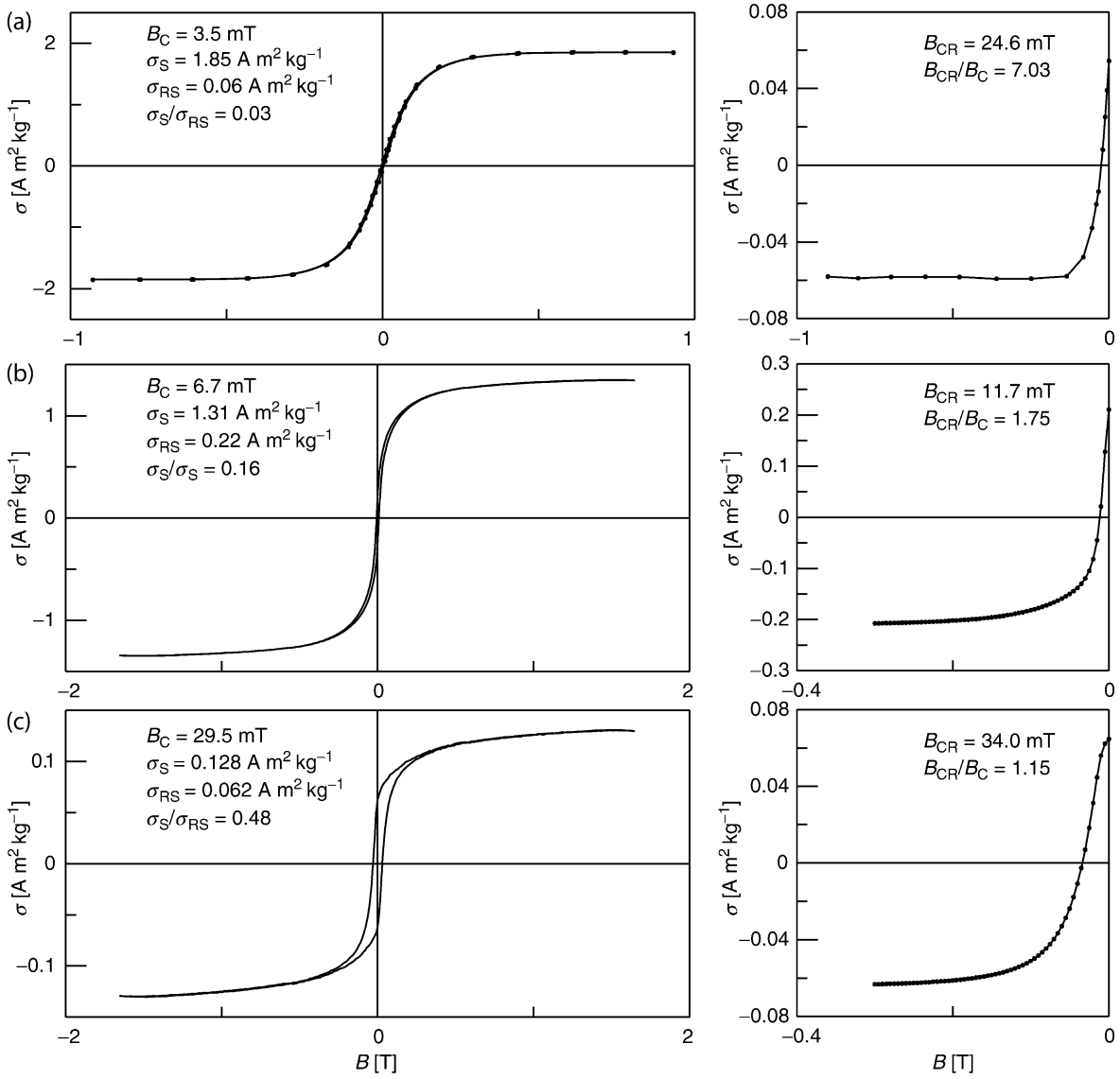

Figure R14 Three examples of room temperature hysteresis curves and corresponding backfield measurements. (a) Synthetic multidomain mangetite (average grain size 12 μm) dispersed in CaF_2 and measured with a VFTB. (b) Young (0.7 Ma) ocean basalt sample containing titanomagnetite. (c) 32-Ma old ocean basalt sample containing single-domain titanomaghemite. Both ocean basalts were measured with a Princeton Measurements VSM.

Table R5 Theoretical values of hysteresis parameters for isotropic noninteracting single-domain particle ensembles (after Joffe and Heuberger 1974)

	Prolate	Oblate	Cubic: $K < 0$	Cubic: $K > 0$
B_{cr}/B_c	1.09	1.15	1.08	1.04
M_{rs}/M_s	0.5	0.638	0.866	0.831

Interpretation of hysteresis loops

Constituents of the hysteresis loop

The initial curve of a hysteresis loop starts at zero field and zero remanence (Figure R10a). There exist many different magnetization states having zero remanence and accordingly many different initial curves are possible. While the most symmetric choice is the thermally demagnetized initial state, usually the alternating field (AF) demagnetized state is regarded in the literature. In sufficiently small fields the initial curve of multidomain particle ensembles can be described by the Rayleigh law:

$$M(B) = \kappa_0 B + \alpha B^2.$$

The first term accounts for reversible changes (wall movements) whereas the second term is associated with irreversible processes. In rock magnetic applications, the initial susceptibility κ_0 is often used as a relative proxy for magnetic mineral concentration.

The part of the hysteresis curve measured between maximum + and maximum − field is called upper hysteresis branch, the subsequent measurement between maximum − and maximum + field is termed lower hysteresis branch. With only a few exceptions (associated with a certain type of magnetic interaction; Meiklejohn and Carter, 1960), the two branches are point symmetric with respect to the origin. The intersections of the hysteresis branches with the ordinate and abscissa give the values for saturation remanence M_{rs} and B_c, respectively. The area between the two branches defines the total hysteresis work E_{hys}. One of the factors influencing the shape of the hysteresis branches is the grain size of magnetic minerals. Figure R12e shows the idealized loop shape for an ensemble of uniaxial single-domain grains, whereas Figure R14a shows the typical ramp-like shape of a sample containing multidomain grains.

An important difficulty in hysteresis measurements is the determination of the saturation magnetization M_s from the loop. It requires to estimate the limit value of magnetization toward high fields. The *approach to saturation* occurs in the high field region where irreversible magnetization changes are completed. The loop is a single branch which in case of pure rotation theoretically is described by:

$$M(B) = \chi_{pd} B + M_s - \frac{a_2}{B^2} + \cdots$$

Experimental evidence rather indicates an expansion

$$M(B) = \chi_{pd} B + M_s - \frac{a_1}{B} - \frac{a_2}{B^2} + \cdots$$

Deviations from the ideal case result mainly from small stress centers of point defects, dislocation dipoles, or inclusions (Kronmüller and Fähnle, 2003). In rock magnetic applications it is sometimes difficult to ensure that a sample is sufficiently saturated since some natural minerals saturate only in high fields and especially titanomagnetites may be extremely sensitive to stress.

A natural generalization of the hysteresis measurement procedure is the variation of start and end fields. Any zigzag sequence of fields $B_1, B_2, \ldots, B_n$ may be applied to the sample to produce a sequence of higher order hysteresis branches. All these branches lie inside the region outlined by the main hysteresis curve between the maximal field values $\pm B_{max}$. The additional information contained in higher order curves may be helpful for a detailed sample characterization. In the framework of Preisach theory it is possible to infer theoretical relations between different higher order curves. Especially, it is possible to show that the complete information of any Preisach system can be retrieved from its first-order curves, which result from the field sequences B_{max}, B, B_{max} (Mayergoyz, 1991).

The most basic interpretation of the backfield curve yields a single value for the coercivity of remanence B_{cr} of the bulk sample. The curve shape, however, does also contain information about the distribution of coercivities due to a mixture of different magnetominerals or a distribution of grain sizes of the contained magnetic phase. It is important to know that the B_{cr} value of a mixture of different magnetic minerals or grain sizes cannot be explained by simple linear mixing theory (e.g., Dunlop 2002a).

Hysteresis parameters

Saturation magnetization M_s is a material constant being independent of grain size. In rock magnetic applications M_s is thus dependent on the type of magnetic mineral and its concentration. In contrast to M_s, saturation remanence M_{rs} is a grain size sensitive parameter. Meaningful interpretation of this parameter therefore almost always requires normalization to M_s as it is also dependent on mineral type and concentration. It can then be compared to theoretical domain state threshold values to determine the magnetic grain size as discussed in the next section. The coercivity parameters B_{cr} and B_c are independent of concentration and can be interpreted in terms of the stability of magnetic remanence. Coercivity is controlled by magnetomineralogy, grain size and the anisotropies controlling the magnetic energy. In minerals being dominated by magnetostrictive anisotropy, e.g., titanomagnetite, the coercivity parameters are strongly dependent on internal and external stresses acting onto the mineral grains. Other important factors controlling coercivity are grain shape, crystal impurities, and lattice imperfections. B_{cr} is generally normalized by B_c in order to yield independent granulometric information.

The Day plot

It was observed by Nagata (1953) that B_c varies linearly with M_{rs}/M_s in igneous rocks. As seen in (3), Néel (1955) explained this linear dependency as a direct effect of the self-demagnetizing field. His theory implies that M_{rs}/M_s and B_c do not represent independent grain size information and that the slope of M_{rs}/M_s versus B_c strongly depends upon M_s and thus on mineralogy (Wasilewski, 1973). In Day *et al.* (1977) it was reported for titanomagnetites that besides M_{rs}/M_s also the ratio B_{cr}/B_c well reflects grain size variations, but is independent of mineral composition. They therefore suggested to plot M_{rs}/M_s versus B_{cr}/B_c and delineated regions containing predominantly SD or MD remanence carriers (Day *et al.*, 1977) (Figure R15). This *Day plot* has since been extensively used in rock magnetism to characterize magnetic grain size. Between the SD and MD region lies a broad transitional interval which is attributed to pseudo-single-domain (PSD) behavior. Several reasons for this peculiar behavior are discussed in the literature (see, e.g., Dunlop and Özdemir, 1997). Among these are SD-like moments in larger MD grains caused by dislocations or surface defects, the magnetic moments of domain walls, unusual domain states such as vortex structures or mixtures of MD and SD grains. Recent theoretical and experimental studies investigate this influence of grain size mixtures upon the Day plot (Dunlop, 2002a,b; Carter-Stiglitz *et al.*, 2001; Lanci and Kent, 2003).

Table R5 after Joffe and Heuberger (1974) gives the theoretical SD values of B_{cr}/B_c and M_{rs}/M_s for isotropic noninteracting particle ensembles. With increasing temperature the value of B_{cr}/B_c for uniaxial random SD ensembles approaches 1 (Joffe, 1969).

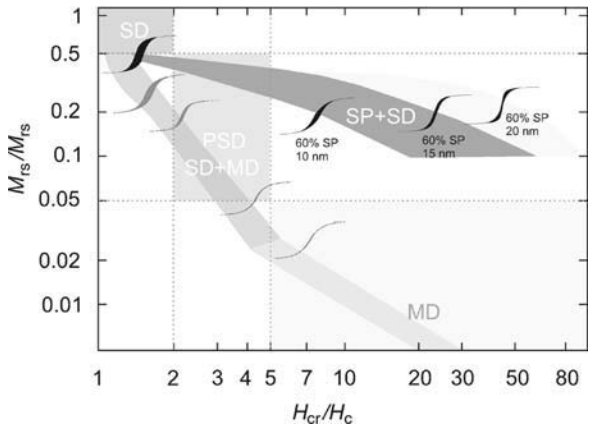

Figure R15 The Day plot classifies hysteresis curves in terms of the grain size sensitive quantities M_{rs}/M_s and B_{cr}/B_c. For magnetite and titanomagnetites the shown grain size classes have been originally defined in Day *et al.* (1977) and recently revised by Dunlop (2002a). The indicated theoretical trends for mixtures are taken from Dunlop (2002a) and Lanci and Kent (2003). While in case of the extensive quantities M_{rs} and M_s normalization is necessary to remove the volume dependence, using the ratio of the intensive quantities B_{cr} and B_c intends to remove dependencies of these quantities upon mineral composition. Exemplary hysteresis loops are shown inset. Loops are centered on the respective M_{rs}/M_s and B_{cr}/B_c values. Black: calculated synthetic loops. Gray: hysteresis loops of synthetic magnetite samples measured with an alternating gradient field magnetometer (maximum field 300 mT).

Hysteresis shape

The possible shapes of magnetic hysteresis loops cover a wide range and only few general rules can be stated. (a) If saturation is reached, all magnetic memory is erased and the loop is point symmetric $M^+(B) = -M^-(-B)$. In most materials the coupling between magnetic system and lattice is very weak and the magnetic free energy obeys the thermodynamic laws. (b) After correcting for para- or diamagnetic slope, each hysteresis branch increases monotonically: $B_1 \leq B_2$ implies $M(B_1) \leq M(B_2)$. (c) The area E_{hys} of the loop corresponds to the energy dissipated by the magnetic system which implies $E_{hys} \geq 0$.

In rock magnetism the general outline of hysteresis loops has been classified into constricted (wasp-waisted) rectangular (normal) and rounded (pot-bellied) shapes (Wasilewski, 1973; Muttoni, 1995; Roberts *et al.*, 1995; Hodych, 1996; Tauxe *et al.*, 1996). Extreme shape variations usually result from mixtures of samples with anhysteretic loops of very different saturation behavior and coercivity (Bean, 1955; Wasilewski, 1973; Hejda *et al.*, 1994). Figure R16 demonstrates shape changes for a simple system of noninteracting SD particles mixed with an SP fraction of varying anhysteretic slope (e.g., grain size). While the vertical loop difference is unchanged by this process, the horizontal difference reflects the degree of constriction from pot-bellied to wasp-waisted loops. To quantitatively describe constriction the ratio between maximal and minimal horizontal difference has been used (Xu *et al.*, 2002; Gee and Kent, 1999). Another possibility is the parameter

$$\sigma_{hys} = \log\left(\frac{E_{hys}}{4M_s B_c}\right), \qquad \text{(Eq. 4)}$$

where log denotes the natural logarithm (Fabian, 2003). For constricted loops $\sigma_{hys} > 0$ whereas for round loop shapes $\sigma_{hys} < 0$.

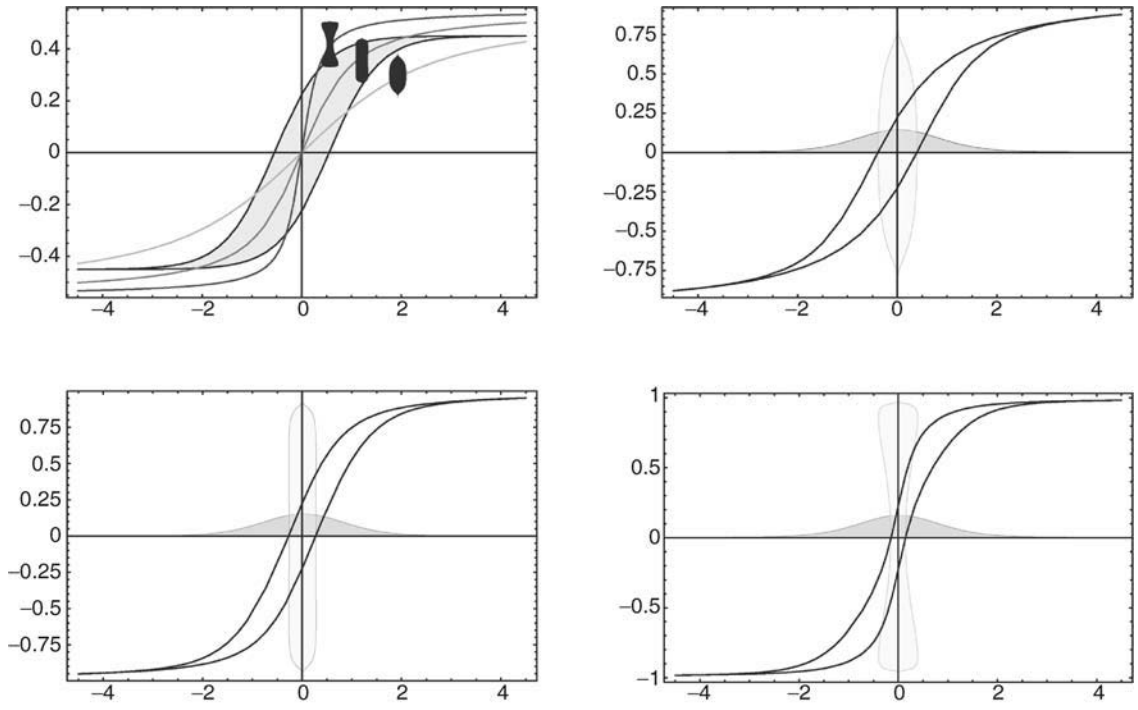

Figure R16 Three hysteresis shapes result from linear mixture of the same primary hysteresis loop with Langevin functions of different susceptibility. The vertical loop difference is unchanged by this process, whereas the horizontal difference clearly reflects the rounded or constricted shape of the loops.

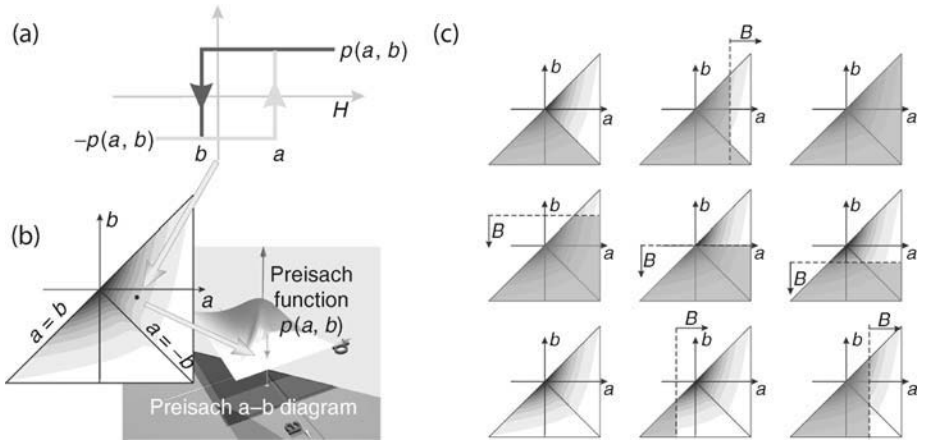

Figure R17 A noninteracting ensemble of rectangular switching curves as in (a) is a very general system with hysteresis. If a and b denote downward and upward switching fields, respectively, the systems hysteresis properties are completely characterized by the Preisach function $p(a, b)$ (b), which is defined for $a \geq b$. In (c) the magnetization change of the system is determined by integration over the Preisach plane. Shaded areas correspond to upward switched loops and count positively, while unshaded areas count negatively (see (Eq. 5)).

Stress control and annealing

An important factor influencing the hysteresis properties of natural and synthetic samples is stress. It originates either from external sources (hydrostatic or shear stress) or from internal sources like defects, dislocations, twin boundaries, or changes in lattice constants due to oxidation or ion diffusion. A further intrinsic stress source for magnetic materials is magnetostriction. It denotes the lattice deformation in reaction to the local magnetic moment vector. Any inhomogeneous magnetization structure creates a magnetostrictive stress field which compensates for the incompatible local deformations (Hubert and Schäfer, 1998).

The inverse effect is that the magnetization structure adapts to external stress patterns. In a material with isotropic magnetostriction constant λ_s an external stress σ leads to an additional uniaxial anisotropy along the stress axis with anisotropy constant $K = \frac{3}{2}\lambda_s\sigma$.

Stress effects both, reversible and irreversible magnetization patterns. Reversible processes which govern the approach to saturation are influenced by the increased anisotropy (Dankers and Sugiura, 1981; Hodych, 1990; Özdemir and Dunlop, 1997), while irreversible processes, reflected by coercive fields as B_c and B_{cr} or remanences as M_{rs}, are enhanced by stress-induced pinning sites. Since characteristic domain sizes scale with $\sqrt{K}$ if all other material parameters are constant (Hubert and Schäfer, 1998), the apparent magnetic grain size, as observed, e.g., in the Day plot, changes with $1/\sqrt{\sigma}$ when stress anisotropy prevails.

Decomposition of hysteresis curves

Conceptually, a hysteresis loop traces a continuous magnetization process and contains much more information about the sample than represented by a few remanence, coercivity or shape parameters. Especially in environmental magnetism one wishes to use all available information to analyze compositional variations within large sample collections. Several procedures have been put forward to exactly describe the hysteresis loop by large parameter sets. Among them are Fourier decomposition (Jackson *et al.*, 1990) and a representation by hyperbolic basis functions (von Dobeneck, 1996). Ideally, such methods attempt to use hysteresis loops and other magnetization curves (Robertson and France, 1994) to decompose a set of given mixed loops into their end members which can be attributed to different sources. In case of linear mixing this kind of decomposition is possible (Thompson, 1986; Carter-Stiglitz *et al.*, 2001). However it is not possible to uniquely identify end members from only mixed samples. Moreover, unmixing procedures which synchronously use different magnetization curves should take into account mutual interdependencies between these curves (Fabian and von Dobeneck, 1997). The extreme case of complete sample description is based on the measurement of the samples Preisach function or—equivalently—its FORC distribution.

Preisach model

Preisach (1935) put forward a simple mathematical concept which allows to understand many fundamental properties of hysteresis loops and other magnetization curves. His model replaces the magnetic sample by a collection of rectangular switching processes characterized by their respective downward and upward switching fields (a, b) (Figure R17a). The weight of (a, b) for the sample is given by the Preisach function $p(a, b)$ (Figure R17b). Whether a loop is in its *up* or *down* position depends on the previous field history. In Figure R17c shaded a-b areas represent loops in *up* position. Increasing the field B switches loops with $a < B$ in the *up* position, decreasing B switches loops with $b > B$ in their *down* position. When $p(a, b)$ is known, the sample magnetization after an arbitrary field history is

$$m = \int_{S^+} p(a,b)\mathrm{d}a\,\mathrm{d}b - \int_{S^-} p(a,b)\mathrm{d}a\,\mathrm{d}b, \qquad \text{(Eq. 5)}$$

where S^+ and S^- denote the subsets of the a-b plane with, respectively, upward or downward switched loops. The Preisach model has been used in rock magnetism to investigate interaction (Dunlop, 1969; Dunlop *et al.*, 1990), viscosity (Mullins and Tite, 1973), and grain size (Ivanov *et al.*, 1981). Mapping of the Preisach function yields detailed information about the sample (Hejda and Zelinka, 1990). A special measurement scheme for mapping of the Preisach function, originally developed and studied by Girke (1960), is now routinely used in rock magnetism (Pike *et al.*, 1999, 2001). Using the Preisach model it is also possible to obtain general theoretical relations between different magnetization processes (Fabian and von Dobeneck, 1997). There is extensive literature on using this or similar models in engineering and mathematics (Mayergoyz, 1991; Visintin, 1991).

David Krása and Karl Fabian

Bibliography

Bean, C., 1955. Hysteresis loops of mixtures of ferromagnetic micropowders. *Journal of Applied Physics*, **26**: 1381–1383.

Bertotti, G., 1998. *Hysteresis in Magnetism.* San Diego: Academic Press.

Carter-Stiglitz, B., Moskowitz, B., and Jackson, M., 2001. Unmixing magnetic assemblages and the magnetic behavior of bimodal mixtures. *Journal of Geophysical Research*, **106**(B11): 26397–26411.

Chevallier, R., and Mathieu, S., 1943. Propriétés magnétiques des poudres d'hématite—influence des dimensions des grains. *Annales de Physique*, **18**: 258–288.

Collinson, D.W., 1983. *Methods in Rock Magnetism and Palaeomagnetism: Techniques and Instrumentation.* New York: Chapman and Hall.

Dankers, P., and Sugiura, N., 1981. The effects of annealing and concentration on the hysteresis properties of magnetite around the PSD-MD transition. *Earth and Planetary Science Letters*, **56**: 422–428.

Day, R., Fuller, M., and Schmidt, V.A., 1977. Hysteresis properties of titanomagnetites: grain-size and compositional dependence. *Physics of the Earth and Planetary Interiors*, **13**: 260–267.

von Dobeneck, T., 1996. A systematic analysis of natural magnetic mineral assemblages based on modelling hysteresis loops with coercivity-related hyperbolic basis functions. *Geophysical Journal International*, **124**: 675–694.

Dunlop, D., 1969. Preisach diagrams and remanent properties of interacting monodomain grains. *Philosophical Magazine*, **19**: 369–378.

Dunlop, D., 2002a. Theory and application of the Day plot (M_{rs}/M_s versus H_{cr}/H_c) 1. Theoretical curves and tests using titanomagnetite data. *Journal of Geophysical Research*, **107**(B3): 2056 (doi: 10.1029/2001JB000486).

Dunlop, D., 2002b. Theory and application of the Day plot (M_{rs}/M_s versus H_{cr}/H_c) 2. Application to data for rocks, sediments, and soils. *Journal of Geophysical Research*, **107**(B3): 2057 (doi: 10.1029/2001JB000487).

Dunlop, D., and Özdemir, Ö., 1997. *Rock Magnetism: Fundamentals and Frontiers. Cambridge studies in Magnetism*. Cambridge: Cambridge University Press.

Dunlop, D.J., Westcott-Lewis, M.F., and Bailey, M.E., 1990. Preisach diagrams and anhysteresis: do they measure interactions? *Physics of the Earth and Planetary Interiors*, **65**: 62–77.

Fabian, K., 2003. Some additional parameters to estimate domain state from isothermal magnetization measurements. *Earth Planetary Science Letters*, **213**: 337–345.

Fabian, K., and von Dobeneck, T., 1997. Isothermal magnetization of samples with stable Preisach function: a survey of hysteresis, remanence and rock magnetic parameters. *Journal of Geophysical Research*, **102**: 17659–17677.

Gee, J., and Kent, D.V., 1999. Calibration of magnetic granulometric trends in oceanic basalts. *Earth Planetary Science Letters*, **170**: 377–390.

Girke, H., 1960. Der Einfluß innerer magnetischer Kopplungen auf die Gestalt der Preisach-funktionen hochpermeabler Materialien. *Zeitschrift für Angewandte Physik*, **11**: 502–508.

Halgedahl, S., and Fuller, M., 1983. The dependence of magnetic domain structure upon magnetization state with emphasis upon nucleation as a mechanism for pseudo-single-domain behavior. *Journal of Geophysical Research*, **88**: 6505–6522.

Hejda, P., and Zelinka, T., 1990. Modelling of hysteresis processes in magnetic rock samples using the Preisach diagram. *Physics of the Earth and Planetary Interiors*, **63**: 32–40.

Hejda, P., Kapička, A., Petrovský, E., and Sjöberg, B.A., 1994. Analysis of hysteresis curves of samples with magnetite and hematite grains. *IEEE Transactions on Magnetics*, **30**: 881–883.

Hodych, J., 1990. Magnetic hysteresis as a function of low temperature in rocks: evidence for internal stress control of remanence in multi-domain and pseudo-single-domain magnetite. *Physics of the Earth and Planetary Interiors*, **64**(1): 21–36.

Hodych, J., 1996. Inferring domain state from magnetic hysteresis in high coercivity dolerites bearing magnetite with ilmenite lamellae. *Earth and Planetary Science Letters*, **142**: 523–533.

Hubert, A., and Schäfer, R., 1998. *Magnetic Domains.* Berlin Heidelberg New York: Springer.

Ivanov, V.A., Khaburzaniya, I.A., and Sholpo, L.Y., 1981. Use of Preisach diagram for diagnosis of single- and multi-domain grains in rock samples. *Izvestiya Earth Physics*, **17**: 36–43.

Jackson, M.J., Worm, H.-U., and Banerjee, S.K., 1990. Fourier analysis of digital hysteresis data: rock magnetic applications. *Physics of the Earth and Planetary Interiors*, **65**: 78–87.

Joffe, I., 1969. The temperature dependence of the coercivity of a random array of uniaxial single domain particles. *Journal of Physics C*, **2**: 1537–1541.

Joffe, I., and Heuberger, R., 1974. Hysteresis properties of distributions of cubic single-domain ferromagnetic particles. *Philosophical Magazine*, **29**: 1051–1059.

Keller, R., and Schmidbauer, E., 1999. Magnetic hysteresis properties and rotational hysteresis losses of synthetic stress-controlled titanomagnetite ($Fe_{2.4}Ti_{0.6}O_4$) particles—I. Magnetic hysteresis properties. *Geophysical Journal International*, **138**(2): 319–333.

Kronmüller, H., and Fähnle, M., 2003. *Micromagnetism and the Microstructure of Ferromagnetic Solids.* Cambridge: Cambridge University Press.

Lanci, L., and Kent, D.V., 2003. Introduction of thermal activation in forward modeling of hysteresis loops for single-domain magnetic particles and implications for the interpretation of the Day diagram. *Journal of Geophysical Research*, **108**(B3): 2142.

Mayergoyz, I.D., 1991. *Mathematical Models of Hysteresis.* New York: Springer-Verlag.

Meiklejohn, W.H., and Carter, R.E., 1960. Exchange anisotropy in rock magnetism. *Journal of Applied Physics*, **31**: 164–165.

Mullins, C., and Tite, M., 1973. Preisach diagrams and magnetic viscosity phenomena for soils and synthetic assemblies of iron oxide grains. *Journal of Geomagnetism and Geoelectricity*, **25**: 213–229.

Muttoni, G., 1995. "Wasp-waisted" hysteresis loops from a pyrrhotite and magnetite-bearing remagnetized Triassic limestone. *Geophysical Research Letters*, **22**: 3167–3170.

Nagata, T., 1953. *Rock Magnetism.* Tokyo: Maruzen.

Néel, L., 1955. Some theoretical aspects of rock-magnetism. *Advances in Physics*, **4**: 191–243.

Özdemir, Ö., and Dunlop, D.J., 1997. Effect of crystal defects and internal stress on the domain structure and magnetic properties of magnetite. *Journal of Geophysical Research*, **102**(B9): 20211–20224.

Pike, C.R., Roberts, A.P., and Verosub, K.L., 1999. Characterizing interactions in fine magnetic particle systems using first order reversal curves. *Journal of Applied Physics*, **85**(9): 6660–6667.

Pike, C.R., Roberts, A.P., Dekkers, M.J., and Verosub, K.L., 2001. An investigation of multi-domain hysteresis mechanisms using force diagrams. *Physics of the Earth and Planetary Interiors*, **126**(1–2): 11–25.

Preisach, F., 1935. Über die magnetische Nachwirkung. *Zeitschrift für Physik*, **94**: 277–302.

Roberts, A., Cui, Y., and Verosub, K., 1995. Wasp-waisted hysteresis loops: minerals magnetic characteristics and discrimination of components in mixed magnetic systems. *Journal of Geophysical Research*, **100**(B9), 17909–17924.

Robertson, D.J., and France, D.E., 1994. Discrimination of remanence-carrying minerals in mixtures, using isothermal remanent magnetization acquisition curves. *Physics of the Earth and Planetary Interiors*, **82**(3–4): 223–234.

Stoner, E., and Wohlfarth, E., 1948. A mechanism of magnetic hysteresis in heterogeneous alloys. *Philosophical Transactions of the Royal Society of London Series A*, **240**: 599–642.

Tauxe, L., Mullender, T., and Pick, T., 1996. Potbellies, wasp-waists, and super-paramagnetism in magnetic hysteresis. *Journal of Geophysical Research*, **101**: 571–583.

Thompson, R., 1986. Modeling magnetization data using simplex. *Physics of the Earth and Planetary Interiors*, **42**(1–2): 113–127.
Visintin, A., 1991. *Differential Models of Hysteresis.* Berlin: Springer-Verlag.
Wasilewski, P., 1973. Magnetic hysteresis in natural materials. *Earth Planetary Science Letter*, **20**: 67–72.
Xu, L., Van der Voo, R., Peacor, D.R., and Beaubouef, R.T., 2002. Alteration and dissolution of fine grained magnetite and its effects on magnetization of the ocean floor. *Earth Planetary Science Letters*, **151**: 279–288.

Cross-references

Magnetization, Isothermal Remanent
Magnetization, Thermoremanent
Paleomagnetism
Rock Magnetism

ROCK MAGNETOMETER, SUPERCONDUCTING

Superconducting Rock Magnetometers, often abbreviated as SRM, are the most commonly used magnetometers in modern Paleomagnetism. The SRM uses superconducting quantum interference devices (SQUIDs), superconducting magnetic flux transformers, superconducting magnetic shielding, and a liquid helium temperature environment of 4.2 K to measure the remanent and induced magnetic moment in samples inserted into the instrument. These samples are usually measured at room temperature. There have been many different configurations of superconducting sensors used for paleomagnetic measurements but, we will focus on the instrument designs that are, or have been commercially available and that have been the most widely used in these magnetic studies.

History

The SRM had its beginning in 1967 with the first development made by the author after meeting Dr. Richard Doell and Dr. Brent Dalrymple of the US Geological Survey at Menlo Park, CA and Prof. Alan Cox of Stanford University. They were conducting research on the reversals of the earth's magnetic field (Cox *et al*., 1964). The author was at Stanford Research Institute in Menlo Park, CA studying the recently discovered quantum interference properties of superconducting devices. These devices were being used as very sensitive detectors of magnetic fields (Deaver and Goree, 1967). In discussions with Doell and Cox it became clear that the use of these superconducting devices could be helpful in the measurement of magnetic properties of geophysical samples.

The standard paleomagnetic measurement systems in use in the 1960s were the astatic, the induction coil spinner, and the fluxgate spinner. See Collinson (1983) and Fuller (1987) for complete descriptions of these instruments. The meetings with Cox, Doell, and Dalrymple in 1967 and 1968, and later discussions with Prof. Michael Fuller at the University of Pittsburgh led to the design and construction of the first SRM by the authors group, then at Develco, Inc., Mountain View, CA. Fuller envisioned many applications of the SRM in the study of magnetic properties of rocks and obtained funding from the US National Science Foundation to buy the first SRM. Fuller's scientific and technical expertise was fundamental in defining the instrument features so that this instrument could be used for many different measurements important to paleo- and rock magnetism (Goree and Fuller, 1976). Figure R18 is a photograph of this first SRM design installed at the University of Pittsburgh in 1970. This instrument was the foundation for design evolution that has resulted in over 200 SRMs used in laboratories throughout the world.

This first SRM was horizontally orientated with a straight through, room temperature access. This design proved to be somewhat complex for the existing state of the art in SQUID and thermal insulation technology, and only two of these systems were constructed. For the next 13 years all SRMs were a more conventional vertical cryogenic design with sample access from the top end, as shown in Figure R19. In this design the superconducting components were installed in a probe that was lowered into a conventional liquid helium dewar. The advantage of this design was primarily that the probe could be easily removed to gain access to the SQUIDs, superconducting shield and cryogenic vacuum seals. The primary disadvantages were the high liquid helium loss rate due to thermal load down the large dewar and probe neck tubes, and the fact that the room temperature access could not be straight through the magnetometer. Therefore the design was not suitable for long core measurements. The typical SRM of this design had a helium loss rate of about 3 l day^{-1}. Several vertical systems were constructed with cryocoolers mounted on the dewar to intercept much of the thermal load, and the loss rate was reduced to about 1 l day^{-1}.

The author reintroduced the horizontal straight through access system in 1981 and incorporated the cryogenic components with

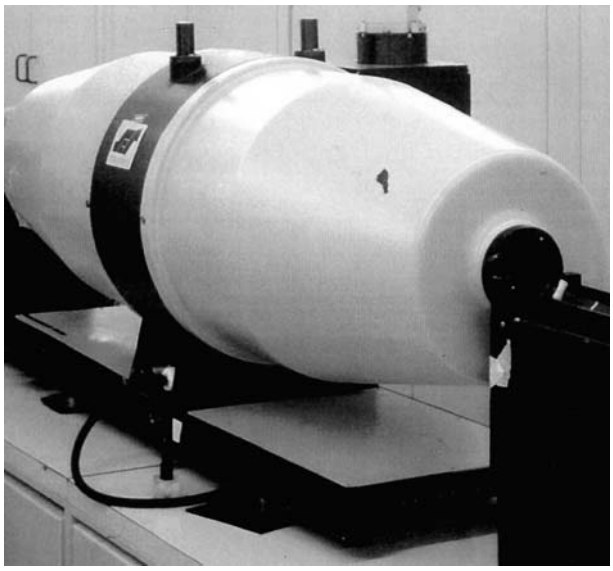

Figure R18 First SRM design.

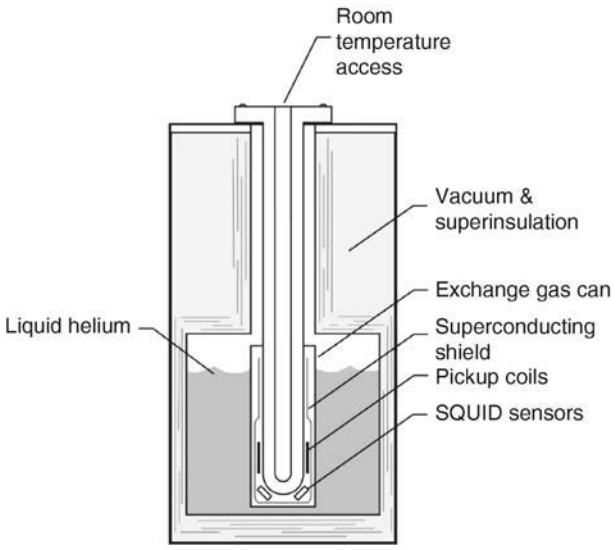

Figure R19 Conventional liquid helium dewar with vertical SRM insert.

Table R6 SRM manufacturers

Company	SRMs delivered
Develco, Inc., 1969–1973	30
Superconducting Technology, Inc., 1973–1975	45
Cryogenic Consultants, Ltd, 1977–1994	15
CTF Systems, Inc., 1977–1990	15
CEA-LETI, France, 1978	3
2G Enterprises, 1981–August 2005	104

the SQUIDs and superconducting shield to provide an integrated design that eliminated the large neck tube heat load between room temperature and liquid helium. This new design has been sold through a marketing arrangement between the authors company (William S. Goree, Inc.) and William Goodman's company (Applied Physics Systems, Inc.) as 2G Enterprises. The new design eliminated all cryogenic fiberglass-epoxy vacuum parts, thereby removing the diffusion of helium gas into the high vacuum insulation volume. These vacuum changes combined with improved superinsulation and mechanical supports and a cryocooler to intercept much of the thermal load resulted in systems with liquid helium loss rates below 0.11 day^{-1}. These very low helium loss rates provided operating times exceeding 3 years on a single fill of helium and made it practical to use the SRM in laboratories where liquid helium was very expensive and/or difficult to obtain.

There have been six different companies, starting in 1969 that have built various styles of the basic SRM. Table R6 list the companies and the approximate number of instruments built by each as of August 2005.

Instrument description

The SRM is an instrument that uses SQUIDs (Kleiner *et al*., 2004) to measure the magnetic field of a sample typically at room temperature. The SQUID is the world's most sensitive detector of magnetic fields and, with the use of superconducting flux transformers, large samples can be coupled to the very small sensor (Goree and Fuller, 1976). One of the first design parameters used in the SRM was the concept of a very homogeneous measurement region. For a "standard" paleomagnetic sample of 2.5-cm diameter by 2.5-cm long it was desired to measure the three orthogonal components of the samples magnetic moment with a single insertion of the sample into the measurement volume. The measurement should be done quickly, in a few seconds, and should be independent of the exact location of the magnetic sources within the sample. A complete magnetic measuring system as used in most paleomagnetic laboratories consists of the SRM for the accurate measurement of the magnetic moment of the sample, sample handling equipment to place the sample into the center of the measurement region of the SRM, alternating field demagnetization coils to produce precise demagnetization of the sample at any desired field strength up to approximately 300 mT, ARM coils used in conjunction with the demagnetization coils, IRM coils to produce large induced moments in the sample, and thermal demagnetization furnaces. Each of these measurement techniques is described in other sections of this encyclopedia.

Many of the SRM systems in use today incorporate the AF demagnetization, ARM and IRM in-line with the SRM and all computer controlled so that very detailed studies of samples can be done without changing samples. The thermal demagnetization is most often done in a separate furnace where up to 100 samples are heated and cooled, then measured with the SRM. This thermal demagnetization is repeated for sequential temperature steps.

The use of the SRM for the measurement of long cores was first envisioned by Fuller and shown to be almost as accurate as cutting a core into discrete samples and measuring each sample independently (Goree and Fuller, 1976). This technique was incorporated in the first long core system specifically designed for the Ocean Drilling Program (ODP, 1985). The ODP system, shown in Figure R20, was the first use

Figure R20 Ocean Drilling Program ship and SRM.

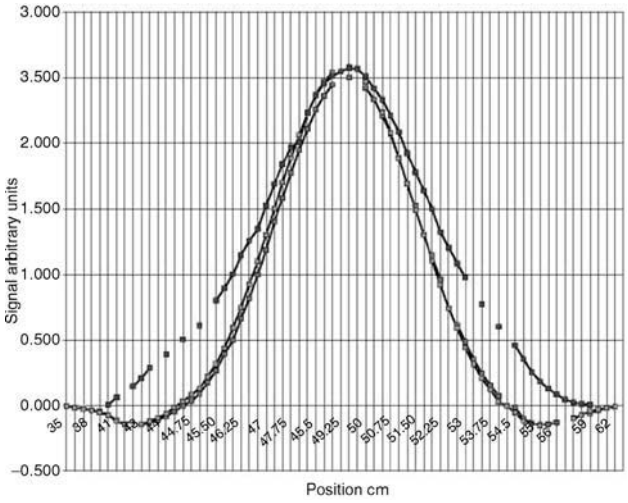

Figure R21 Sensitivity profile for high-resolution pickup coils.

of an SRM on an ocean going ship. This SRM was used continuously by ODP from 1985 until 1992 when it was replaced with an improved design SRM that used DC SQUIDs for better sensitivity. This SRM is still in use on the ODP ship as of 2005. It has been estimated that ODP scientists with the two SRMs have measured 200 000 m of ocean core. Most of the measurements were done on semicircular half cores 150-cm long, and the cores were often passed through the magnetometer many times with sequential AF demagnetization. As of 2005 there have been ten long core SRMs installed.

Carlo Laj and colleagues at GIF Sur Yevette, France became interested in measuring long sediment samples with better axial resolution of the magnetic moment. Tauxe *et al*. (1983) suggested a U-channel sample configuration to obtain a clean section of sediment cores. These samples were 2 cm by 2 cm cross-section by 150-cm long cut from near the center of a circular core. The first U-channel SRM was delivered to GIF in 1991 (Weeks *et al*., 1993). The pickup coil construction for U-channel systems was optimized for sampling a smaller volume of the sample and is called a high-resolution (HR) pickup coil. (Figure R21 shows sensitivity profiles for HR pickup coils.) A second U-channel system was installed at IPGP, Paris in 1992 to measure discrete samples as well as U-channels (Nagy and Valet, 1993). Many laboratories have adopted the use of the high-resolution pickup coil system to measure both U-channels and discrete samples since 1992. There have been seventy-two 2G SRMs built

since the GIF system was delivered in 1991 and 14 of these have used the high-resolution U-channel design.

If a 150-cm long core or U-channel is measured every cm of its length, with AF, ARM, and IRM sequences, it may take on the order of 10 h to complete a full measurement cycle where thousands of individual measurements are made. A study with this detail using an astatic magnetometer of the 1960s would have taken years of measurement time.

Superconducting quantum interference device

The SQUID is a very small device with a magnetic field sensitive area of the order of 10^{-6} m^2 (Deaver and Goree, 1967) and is the heart of an SRM. The SQUID is basically a superconducting loop with a diameter of less than 1 mm. The optimum energy sensitivity of an RF SQUID is obtained when the energy of a quantum of flux in the SQUID, $\emptyset_0^2/2L$ is larger than the thermal energy, kT, where $\emptyset_0$ is the flux quantum (2.07×10^{-15} weber), L is the SQUID loop inductance, k is the Boltzmann constant, and T is the absolute temperature of the SQUID (Zimmerman and Campbell, 1975). The optimum energy sensitivity for a DC SQUID scales as $T\,(LC)^{1/2}$ (Kleiner *et al*., 2004). Thus, the SQUID must have a very small capacitance, C, and a very small inductance, L. The SQUID capacitance is set by the junction technology and is about 1 pF for thin film niobium junctions. The inductance is about 100 pH, which gives a SQUID loop diameter of less than 1 mm. This very small SQUID area requires that most samples to be measured must be coupled to the SQUID using a superconducting flux transformer that will be discussed in the next section, rather than being placed within the SQUID. The SQUID responds to changes in the magnetic flux that links the body of the SQUID. A unique quantum mechanical property of a SQUID is that the magnetic flux linking the SQUID area is quantized in units of $h/2e$, where h is Planck's constant and e is the charge of an electron. This fundamental property of superconductors gives the SQUID a digital output in units of the flux quanta $\emptyset_0$. In an SRM each measurement axis is calibrated by determining the magnetic moment applied at the center of the pickup coil that will produce one flux quanta change at the SQUID. A typical calibration number for an SRM with 4.2-cm diameter room temperature access is 5×10^{-8} A m^2 per flux quanta. The noise level of a SQUID is often measured in terms of the fraction of single flux quanta that can be resolved. This can approach one part in 10^6 for DC SQUID instruments.

The first SRMs used radio frequency driven single junction SQUIDs (Kleiner *et al*., 2004) beginning with a cylindrical SQUID approximately 1-mm diameter. Later this type was replaced with a toroidal niobium body SQUID. These SQUIDs were driven at radio frequencies of about 20 MHz. The noise level of the RF SQUID was typically 10^{-4} flux quanta and, in the early instruments this noise was approximately equal to the noise from the magnetometer produced by vibration of magnetic impurities within the pickup coil region and Johnson noise in the thermal insulation. After about 10 years of SRM development the instrument noise was reduced to less than the RF SQUID noise.

A major improvement in the SRM sensitivity came with the use of DC SQUIDs in an SRM in 1994. The DC SQUID uses two Josephson junctions connected in parallel (Kleiner *et al*., 2004). It is operated by applying a DC voltage across the two junctions, which then oscillate at the Josephson frequency of 500 MHz μV^{-1}. The applied voltage is normally tens of microvolts so the SQUID frequency is about 10 GHz. This very high operating frequency results in a greatly improved SQUID noise level. A typical DC SQUID has an intrinsic noise level of a few by 10^{-6} flux quanta. This is about 100 times lower than the RF SQUIDs used in the earlier SRMs. After many changes in the internal construction of the SRM a usable sensitivity of less 10^{-5} flux quanta has been obtained. This gives a magnetic moment noise level of about 3×10^{-13} A m^2 dipole moment for a 4.2-cm access DC SQUID SRM compared to about 8×10^{-12} A m^2 for the RF SQUID SRM or an improvement of over 20 to 1. Further improvements in the DC SQUID SRM sensitivity can be expected as the noise from the superinsulation is reduced.

Pickup coils and flux transformers

The desire to measure large samples with relatively uniform sensitivity over the sample volume can be achieved by using the zero resistance property of a superconductor. A two axis superconducting magnetic flux transformer is used in the SRM as shown in Figure R22 (Goree and Fuller, 1976). The SRM normally uses three orthogonal superconducting pickup coils cocentered about the sample position. The axial pickup coils are typically constructed in a Helmholtz configuration (Helmholtz, 1849), and the transverse pickup coils are saddle-shaped coils. The large superconducting pickup coil is connected to the SQUID input coil. Efficient energy transfer from this large coil to the small SQUID is obtained if the inductance of the pickup coil is equal to the inductance of the SQUID input coil. This inductive matching transfers one-half of the magnetic field energy applied to the pickup coil to the SQUID input coil (Deaver and Goree, 1967).

Superconducting shields

Another crucial element of an SRM is the superconducting magnetic shield. The magnetic field sensitivity of an SRM is of the order of 10^{-14} T where the earth's magnetic field is approximately 5×10^{-4} T. In order to use the extreme sensitivity of the SQUID system, very effective magnetic shielding is a necessity. A superconducting shield is the best magnetic shield known. In order to provide sample access inside the shield the typical SRM uses a superconducting shield that is open at one or both ends. If an external magnetic field is applied to the open end of a superconducting cylinder the net field at any cross-section of the cylinder will be zero, but the distribution of the field change will be such that the field along the cylinder axis is

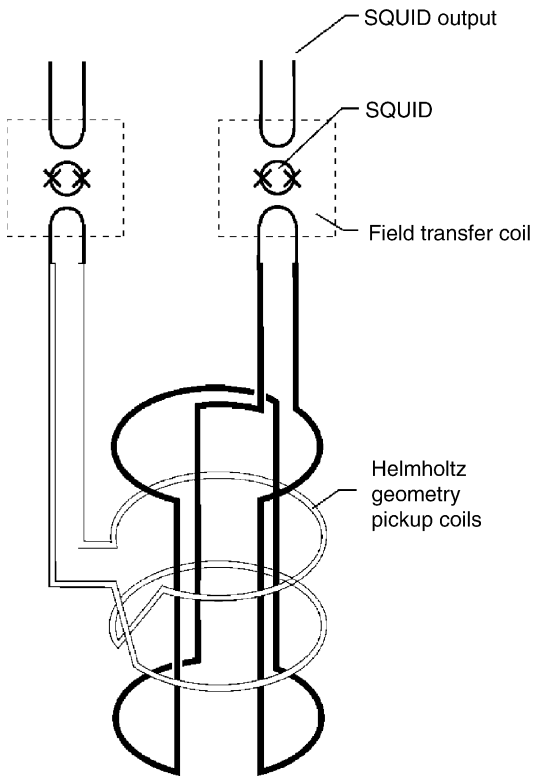

Figure R22 Two axis pickup coils.

in the same direction as the applied field and the field near the inner walls of the cylinder will oppose the applied field. In the design of a magnetic shield for the SRM the field change measured along the shield axis is normally used to determine the required shield length. The on-axis attenuation of axially applied fields is given by $31^{(x/r)}$ where x is the on-axis distance into the cylinder from an open end and r is the radius of the superconducting shield. The on-axis attenuation of fields applied transverse to the shield axis is given by $36^{(x/2r)}$ (Deaver and Goree, 1967). A typical design attenuation for transverse fields is 10^6 and this gives a minimum shield length of 7.7 times shield radii. For this shield length and transverse attenuation of 10^6 the axial attenuation will be $31^{(7.7r)/r} = 3.0 \times 10^{11}$. Thus, the axial attenuation of a cylindrical shield is orders of magnitude better than its transverse attenuation, and it is important to place the SRM where the ambient magnetic transverse field noise is a minimum.

Cryogenics

Another important performance variable in an SRM is the cryogenic environment. The SRM normally uses liquid helium as the thermal environment. A few SRMs have used liquid nitrogen as a secondary coolant, but most have used superinsulated dewar construction (Kropschot *et al*., 1968). In a superinsulated dewar the liquid helium reservoir and SQUID volume are enclosed in a vacuum region surrounded by many layers of aluminized mylar placed within this vacuum. Thermally conducting shields are also placed within this region and are cooled by utilizing the heat capacity of the evolving helium gas. The first SRMs used about 31 of liquid helium per day. Since the initial development of the SRM cryocoolers have been incorporated into the thermal design. The cryocooler is used to provide external cooling to the thermal shields placed within the superinsulation. A typical two stage cryocooler as used with the 2G Enterprises SRM will absorb about 0.5 W of heat at 15 K and 15 W at 80 K (CTI model 350, 2004). The extra cooling provided by the cryocooler will reduce the helium loss rate to below 0.11 day^{-1} in a properly designed dewar. This greatly reduced loss rate has made it practical to use SRMs in laboratories where liquid helium is difficult to obtain and/or is very expensive.

It is also possible to use cryocoolers that will either reduce the helium loss rate to essentially zero, or produce the required low temperature without a reservoir of liquid helium. Cryocoolers that will produce 4K temperatures and/or liquid helium have been available for many years but the cost and poor long-term reliability have made them unacceptable for use with SRMs. Recent developments with pulse tube cryocoolers appear to change this situation. The author, in October 2004, began the development of a new magnetometer that would not use any liquid helium. The first SRM using this new pulse tube cryocooler technology (Cryomech, Inc., 2005) was completed and delivered to Dr. J. Hus at Dourbes, Belgium in May 2005 (Institut Royal Metrologique, Belgium). SQUID and superconducting shield temperatures of approximately 4.0 K were obtained from room temperature to operation in about 3 days and the magnetic measurement performance is identical to that achieved with the liquid helium cooled systems. The pulse tube cryocooler has no moving mechanical parts at low temperatures and is predicted to have a very long mean time between failure, probably in excess of 15 years for the cold head, 10 years for the easily replaced drive motor, and about 10 years for the compressor. The projected excellent reliability of the pulse tube cryocooler has made it practical to use with this new SRM.

High temperature superconductors

The discovery of materials that become superconducting at "high" temperatures in 1986 (Bednorz and Muller 1986) caused much excitement in all fields of superconductivity. If instruments could be built with these new materials and operate at 70–90 K the fabrication and operating cost could be dramatically reduced. Unfortunately, the high temperature materials that have been discovered to date (2004) are very brittle and it has been difficult to make high temperature superconducting wires and SQUIDs. In particular, wires have not been produced where superconducting pickup coils and transformers can be constructed (Kleiner *et al*., 2004).

William S. Goree

Bibliography

2G Enterprises, Goree, W.S., at William S. Goree, Inc., 2040 Sunset Drive, Pacific Grove, CA, 93950 (wgoree@wsgi.us), and Goodman, W.L., at Applied Physics Systems, Inc., 1245 Space Park Way, Mountain View, CA 94043 (goodman@appliedphysics.com).

Bednorz, J.G., and Muller, K.A., 1986. Z. Phys. B. **64**: p. 189.

Collinson, D.W., 1983. *Methods in Rock and Paleomagnetism: Techniques and Instrumentation.* London: Chapman and Hall, 503 pp.

Cox, A., Doell, R.R., and Dalrymple, G.B., 1964. Reversals of the earth's magnetic field. *Science*, **144**: 1537–1543.

Cryomech, Inc., 2005. 113 Falso Drive, Syracuse, NY 13211 (http://www.cryomech.com).

CTI, 2004. Cryogenic Technology, Inc., a division of Helix Technology (http://www.helixtechnology.com).

Deaver, B., and Goree, W.S., 1967. Some techniques for sensitive magnetic measurements using superconducting circuits and magnetic shields. *Review of Scientific Instruments*, **38**: 311–318.

Fuller, M., 1987. Experimental methods in rock magnetism and paleomagnetism. *Methods of Experimental Physics*, **24**: 303–471.

Galbrun, B., At CEA, Grenoble, France.

Good, J., Cryogenic Limited (http://www.cryogenic.co.uk).

Goree, W.S., and Fuller, M.D., 1976. Magnetometers using RF-driven SQUIDs and their applications in rock magnetism and paleomagnetism. *Reviews of Geophysics and Space Physics*, **14**: 591–608.

Helmholtz, H.V., 1849. *Vortrag in der Sitzung*, Volume 16, III. Berlin: Physikalische Gesellschaft; Loeb, L.B., 1947. *Fundamentals of Electricity and Magnetism*, 3rd edition. New York: John Wiley & Sons.

Kleiner, R., Koelle, D., Ludwig, F., and Clarke, J., 2004. *Superconducting Quantum Interference Devices: State-of-the-Art and Applications.* Proceedings of the IEEE, Special Issue on Applications of Superconductivity, Volume 92, October 2004, pp. 1534–1548.

Kropschot, R.H., *et al.,*1968. Technology of liquid helium. *National Bureau of Standards Monograph*, **111**: 170.

Nagy, E.A., and Valet, J.P., 1993. New advances in paleomagnetic studies of sediment cores using U-channels. *Geophysics Research Letters*, **20**: 671–674.

ODP, 1985. Please see the ODP website: http://www.odp.edu/.

Tauxe, L., Labrecque, J.L., Dodson, R., and Fuller, M., 1983. "U" channels—a new technique for paleomagnetic analysis of hydraulic piston cores. *Eos, Transactions, American Geophysical Union*, **64**: 219.

Vrba, J., CTF Systems, Inc., 9 Burbidge Street, Coquitlam, BC, Canada Y3K7B2 (corp@vsmmedtech.com).

Weeks, R., Laj, C., Edignoux, L., Fuller, M., Roberts, A., Manganne, R., Blanchard, E., and Goree, W.S., 1993. Improvements in long-core measurement techniques: applications in paleomagnetism and paleoceanography. *Geophysical Journal International*, **114**: 651–662.

Zimmerman, J.E., and Campbell, W., 1975. Test of cryogenic Squid for geomagnetic field measurements. *Geophysics*, **40**: 269–284.

RUNCORN, S. KEITH (1922–1995)

I first met S.K. Runcorn in June of 1955. I had just graduated from Columbia College with a degree in Geology. He reached me at my grandparent's home on a Saturday morning and asked if I would like to be his field assistant working in Arizona for the summer and by the way I had to leave with him on Monday morning. I thought it

was a joke but the longer we talked the more it seemed to be a real offer. So after a lot of discussion in the family I decided to take the risk on Runcorn so off we went on Monday to the wild west. Runcorn was supremely self-confident and somehow always expected things to turn out the way he wanted them to. By the end of the summer I was on my way to Cambridge England instead of Wyoming where I had expected to do my graduate studies. We first met when Keith was 33-years old having been born in 1922 in Southport Lancashire. He loved to swim and played rugby until he was past 40. He had a great interest in religion and during a trip to France, Italy, and Switzerland, which we took in late 1955, we made a tour of the great Cathedrals of France and northern Italy. In his later years he was to serve on the Vatican Council even though he was a lifelong member of the Church of England.

Without a doubt however his great love was science. His undergraduate education was obtained at Cambridge University where he was a member of Gonville and Caius College. He studied engineering, receiving his degree in 1943 and spent the rest of the war researching at the Royal Radar Establishment. In 1946 he was appointed to a lectureship in the Physics Department at Manchester University were P.M.S. Blackett was Department Chairman. Research in the Physics Department was dominated by cosmic ray research. However, Blackett was becoming interested in the generation of Earth's magnetic field and proposed a theory that rotating matter would generate a magnetic field and suggested that Runcorn get involved in this research. The competing theory was proposed by Elsasser and expanded by Bullard that the Earth's magnetic field arises from electric currents in the Earth's core. The simple test to differentiate between the two is to measure the field at the surface and at depth in the earth, if the field increases then the field is generated within the Earth. This experiment was carried out by Runcorn and others in the coalmines of Lancashire and Yorkshire. The field was shown to increase with depth showing that the field originated within the earth. This study served as Runcorn's PhD thesis.

Blackett had produced a very sensitive astatic magnetometer in his attempt to measure the magnetic field of a rotating gold ball, this failed but the magnetometer was put to work trying to find a record of secular variation in sediments and Runcorn became interested in this problem. Runcorn accepted a position at the department of Geodesy and Geophysics at Cambridge at about the same time (1950) that Blackett moved to Imperial College London, paleomagnetic research began at both institutions, which of course became a competition. When Runcorn arrived at Cambridge he found that paleomagnetic research had already begun on lavas from Iceland by Jan Hospers who found superimposed lavas of normal and reverse polarity, which were aligned along the axis of Earth's rotation however there was no laboratory. Runcorn set about to construct a new Paleomagnetic laboratory with the help of his students, K.M. Creer, E. Irving, D.W. Collinson, and J.H. Parry. The emphasis was still on secular variation but it soon became apparent that directions obtained by Irving in the pre-Cambrian and by Creer in Triassic red sediments were widely divergent from the present field and it became apparent that red sediments and igneous rocks gave internally consistent paleomagnetic results. The group used statistics developed by Fisher and the first apparent polar wander curve was produced by 1954. These results were interpreted as true polar wander an idea that was proposed by T. Gold. The early results from Runcorn's group were mostly from British rocks. However by 1954 Runcorn was traveling to the United States to collect rock samples and the first results had been obtained. By 1954 the original group began to disperse; Irving to Australia and Creer to the British Geological Survey.

Runcorn did not limit his research to paleomagnetism and he built a research group at Cambridge that studied various aspects of magnetic field behavior, e.g., R. Hide on convection in rotating fluids, P.H. Roberts on magnetohydrodynamics, F. Lowes on detecting earth currents which he believed might be leaking from the core. After the departure of Irving and Creer the paleomagnetic group at Cambridge consisted of J.C. Belshe, A.E.M. Nairn, D.W. Collinson, and J. Perry. This group was joined in the autumn of 1955 by N.D. Opdyke.

Runcorn was offered the position of Professor of Physics in the Department of Physics at the College of Newcastle on Tyne, which at the time was King's College of Durham University. He transferred the paleomagnetics laboratory to Newcastle and it was up and running in 1956. At the time of the move to Newcastle he was still maintaining that the data from North America and Europe could still be explained by Polar Wander alone. However the data was becoming better and a separation of the polar wander paths of Europe and North America persisted with the North American curve falling systematically to the West of the European curve. In the spring of 1956 he decided that the data could not be explained solely by Polar Wandering and he embraced Continental Drift. It is also true that new data was coming in from Australia that certainly could not be explained by Polar Wander alone. He became a fervent supporter of Continental Drift and lectured widely on the subject in Europe and North America where the Earth Science community was hostile to the idea. He and all paleomagnetists would see these ideas vindicated in the late 1960s by the success of the Plate Tectonic Theory. Runcorn adopted a strategy to convince the scientific community that crustal mobility was real. Ken Creer had rejoined him at Newcastle and was given the task of producing a polar wander curve for South America and Alan Nairn was sent to Africa were Anton Hales and Ian Gough were already working. Ted Irving had gone to Australia where his results were beginning to appear in print. The last of the easily accessible Gondwana continents was India where Blackett's group from Imperial College was working hard. It is interesting that Blackett was a supporter of Continental Drift in the early 1950s but did not say so in print until 1960. North American paleomagnetists were very skeptical of Continental Drift, in particular John Graham was a strong opponent of Continental Drift and he and Runcorn had some rather heated public debates, which on Graham's part became rather personal. Cox and Doell were not convinced that paleomagnetic data supported Continental Drift as late as 1960. Runcorn was always cool under verbal attack and I cannot ever recall him responding in kind. He was always interested by the idea of convection in the mantle and proposed that solid-state creep under stress from thermal and gravitational effects was responsible for the motion of continents.

He stopped doing active research in paleomagnetism in the mid-1960s and turned his attention to other scientific problems. He became fascinated by the origin and evolution of the Moon and the possibility of convection during the early history of the moon. He took advantage of the fact that the USA was going to the moon, which meant that funds would become available for lunar research. Moon rocks were returned from the moon in 1969 and in subsequent years till the end of the Apollo program. The magnetic properties of these rocks were studied at Newcastle and in other laboratories and all were found to be magnetic. Runcorn concluded that the Moon must have had a magnetic field early in its history and that this field must have been generated by magnetohydrodynamic motions in the Moon's core. Satellites orbiting the moon detected small magnetic anomalies, which Runcorn attributed to magnetizations being acquired at different times during the early history of the moon prior to 3.9-Ga years ago and resulting from the moon having a dipole field. The different pole positions he attributed to polar wander on the moon, which he suggested was caused by impacts on the Moon's surface. His last paper published in 1996 was titled "The Formation of the Lunar core."

Runcorn had a inquiring mind and during his career he published on many different subjects for example wind directions determined from eolian sandstone, the changing length of the day through time as recorded in coral growth, earth currents using abandoned cable in the Pacific, earthquakes and polar motion, excitation of the Chandler wobble, and convection in the Planets.

Runcorn was regarded highly by the scientific Community and this high regard resulted in many honors. He was elected a fellow of the Royal Society in 1965, the Indian National Academy of Science (1980), and he was an honorary member of the Royal Netherlands Academy of Arts and Sciences (1985), The Royal Norwegian Academy of Science and letters (1985), the Bavarian Academy of Science (1990), and the Royal Society of New South Wales (1993). He won

a series of awards and medals beginning with the Napier Shaw prize of the Royal Meteorological Society (1959), the Charles Chree prize from the Institute of Physics (1969), the Vetlesen prize of Columbia University (1971), the John Adams Fleming Medal from the AGU (1983), the Gold Medal From the RAS (1984), and the Wegener Medal from the EGU (1987). He was appointed to Papal Academy of Sciences and helped to get Galileo reinstated by the Catholic Church.

Runcorn retired as the Professor of Physics at Newcastle in 1988 but he never stopped working. He was appointed to the Chapman Chair of Physical Sciences at the University of Alaska at Fairbanks, spending three months a year in Alaska teaching and doing research. He was found dead in his hotel room in San Diego on 5th December 1995 being the victim of a violent attack. He is mourned by many to whom he was a friend and mentor. He was a unique individual who was married to science and whose home was the Universe.

Neil Opdyke

RUNCORN'S THEOREM

This remarkable theorem is concerned with the exterior magnetic field generated by magnetized materials at the surface of a planet. Usually magnetized materials above their Curie temperature lead to patterns of *magnetic anomalies* (*q.v.*); however, under idealized circumstances it transpires that some arrangements of magnetization lead to no external magnetic field, because of extremely subtle and fortuitous cancellation of the magnetic fields generated by one area of magnetization by the magnetic fields generated by another area of magnetization. The proof of this fact is quite complex, and the reader uninterested in the details should skip to the last two paragraphs to discover the application of this theorem.

We fix attention on the exterior magnetic field $\mathbf{B}(\mathbf{r}_j)$ (at observation point $\mathbf{r}_j$) generated by a magnetization distribution $\mathbf{M}(\mathbf{r})$ enclosed in a spherical shell whose volume we denote by V and surfaces by ∂V. The field $\mathbf{B}(\mathbf{r}_j)$ can be derived from a potential ϕ_m as

$$\mathbf{B}(\mathbf{r}_j) = -\nabla\phi_m(\mathbf{r}_j),$$

where ϕ_m is given by

$$\phi_m(\mathbf{r}_j) = \frac{\mu_0}{4\pi}\int_V \mathbf{G}(\mathbf{r},\mathbf{r}_j)\cdot\mathbf{M}(\mathbf{r})\mathrm{d}^3\mathbf{r}, \qquad \text{(Eq. 1)}$$

where the vector Green's function $\mathbf{G}(\mathbf{r},\mathbf{r}_j)$ is given by

$$\mathbf{G}(\mathbf{r},\mathbf{r}_j) = \nabla\frac{1}{|\mathbf{r}_j-\mathbf{r}|}. \qquad \text{(Eq. 2)}$$

The potential and thus the magnetic field is in general nonzero for arbitrary $\mathbf{M}(\mathbf{r})$. There are, however, a few distributions of $\mathbf{M}(\mathbf{r})$ (termed *annihilators*) that generate no exterior, a simple example is the arrangement $\mathbf{M}(\mathbf{r}) = A(r)\hat{\mathbf{r}}$ for arbitrary function $A(r)$, a purely radial magnetization. This spherical arrangement is the equivalent of the infinite plane layer with constant magnetization in a Cartesian geometry, which also generates no external field. In the spherical case it generates no magnetic field because the radial part of the vector Green's function contains no spherical harmonic of degree zero (see (7) below), whereas the magnetization $\mathbf{M}(\mathbf{r}) = A(r)\hat{\mathbf{r}}$ contains only degree zero; consequently the orthogonality of *spherical harmonics* (*q.v.*) leads to a zero result.

In 1975 Keith Runcorn proved that a more complex arrangement of magnetization was also an annihilator, namely that arising when a homogeneous material is magnetized by an arbitrary internal source. The theorem applies equally well to the case of remanent or induced magnetization, but we treat the case of induced magnetization here. Assuming that a linear relation exists between magnetization and applied magnetic field via a constant α, we have an equation of the form

$$\mathbf{M}(\mathbf{r}) = \alpha\mathbf{B}(\mathbf{r})$$

(in SI the constant $\alpha = \chi/\mu_0$; see Crustal magnetic field). It is the case that the inducing field is itself a potential field satisfying Laplace's equation, so we can write $\mathbf{B} = -\nabla V_\mathrm{i}$ where V_i is the internal potential (see Main field modeling); then the integral (1) reads

$$\phi_m(\mathbf{r}_j) = -\alpha\frac{\mu_0}{4\pi}\int_V \nabla\frac{1}{|\mathbf{r}_j-\mathbf{r}|}\cdot\nabla V_\mathrm{i}\mathrm{d}^3\mathbf{r}, \qquad \text{(Eq. 3)}$$

where the "self-magnetization" due to terms of order α^2 have been dropped.

We expand V_i in terms of fully normalized spherical harmonics with coefficients β_l^m, analogous to the conventional Gauss coefficients $\{g_l^m; h_l^m\}$

$$V_\mathrm{i} = c\sum_{l=1}^{\infty}\sum_{m=-l}^{l}\left(\frac{a}{r}\right)^{l+1}\beta_l^m Y_l^m(\theta,\phi), \qquad \text{(Eq. 4)}$$

where c is the core radius; by assuming that the mantle is an insulator, V_i is harmonic everywhere outside of c. The spherical harmonics satisfy an orthogonality relation when integrated over the unit sphere Ω on which $|r| = 1$ as follows:

$$4\pi\int_\Omega Y_l^m Y_p^q \mathrm{d}\Omega = \delta_{lp}\delta_{mq}. \qquad \text{(Eq. 5)}$$

For constant susceptibility, (3) can be written as

$$\phi_m(\mathbf{r}_j) = -\alpha\frac{\mu_0}{4\pi}\int_{\partial V}\hat{\mathbf{n}}\cdot\nabla\frac{1}{|\mathbf{r}_j-\mathbf{r}|}\mathbf{V}_\mathrm{i}(\mathbf{r})\mathrm{d}^2\mathbf{r} \qquad \text{(Eq. 6)}$$

by an application of Gauss' Theorem, where $\hat{\mathbf{n}}$ is a unit normal and ∂V represents both the inner and outer surfaces of the shell. We use the expansion of the reciprocal distance in spherical harmonics for $|\mathbf{r}_j| > |\mathbf{r}|$

$$|\mathbf{r}_j-\mathbf{r}| = \frac{1}{r_j}\sum_{l=0}^{\infty}\sum_{m=-l}^{l}\frac{1}{2l+1}\left(\frac{r}{r_j}\right)^l Y_l^m(\theta,\phi)Y_l^m(\theta_j,\phi_j) \qquad \text{(Eq. 7)}$$

to obtain

$$\phi_m(\mathbf{r}_j) = -\alpha\frac{\mu_0}{4\pi}\int_{\partial V}\sum_{l,m}\frac{l}{2l+1}\left(\frac{r}{r_j}\right)^{l+1} Y_l^m(\theta,\phi)Y_l^m(\theta_j,\phi_j) \times c\sum_{p,q}\left(\frac{c}{r}\right)^{p+1}\beta_p^q Y_p^q(\theta,\phi)\mathrm{d}\Omega \qquad \text{(Eq. 8)}$$

We invoke equation(s) and find that the orthogonality of the Y_l^m couples l and p in the sums, leading to

$$\phi_m(\mathbf{r}_j) = -\alpha\mu_0\int_{\partial V}\sum_{l,m}c\beta_l^m\frac{l}{2l+1}\left(\frac{c}{r_j}\right)^{l+1} Y_l^m(\theta_j,\phi_j)\mathrm{d}\Omega. \qquad \text{(Eq. 9)}$$

Since the integrand consists of two spherical surfaces with opposing outward normals, then each surface integral gives a contribution of the same absolute value but of opposite sign, and therefore the external potential generated is zero. This is Runcorn's (1975a,b) theorem. Note that the theorem also allows α to be a function of r simply by noting that the theorem applies equally well to infinitesimally thin shells; each shell generates no field even when α is different in each one.

The importance of this theorem was in explaining the absence of any appreciable exterior field outside Earth's moon, despite the presence of apparently significantly magnetized rocks on the Moon's surface. Runcorn (1975a,b) hypothesized that the mantle rocks had been magnetized by an internally generated dynamo field (now switched off) as they cooled through their Curie temperature; provided the Curie isotherm is everywhere spherical and the remanent susceptibility is everywhere only a function of radius, this even allows a time-dependent internal source field.

For a higher order analysis in α and the treatment of an ellipsoidal Earth, see Jackson *et al*. (1999) and Lesur and Jackson (2000). Further description of the general form of annihilators can be found in Arkani-Hamed and Dyment (1996) and Maus and Haak (2003).

A. Jackson

Bibliography

Arkani-Hamed, J., and Dyment, J., 1996. Magnetic potential and magnetization contrasts of Earth's lithosphere. *Journal of Geophysical Research*, **101**(B5): 11401–11426 (doi: 10.1029/95JB03537).

Jackson, A., Winch, D.E., and Lesur, V., 1999. Geomagnetic effects of the Earth's ellipticity. *Geophysical Journal International*, **138**: 285–289.

Lesur, V., and Jackson, A., 2000. Exact nonlinear solutions for internally induced magnetisation in a shell. *Geophysical Journal International*, **140**: 453–459.

Maus, S., and Haak, V., 2003. Magnetic field annihilators: invisible magnetisation at the magnetic equator. *Geophysical Journal International*, **155**: 509–513.

Runcorn, S.K., 1975a. An ancient lunar magnetic dipole field. *Nature*, **253**: 701–703.

Runcorn, S.K., 1975b. On the interpretation of lunar magnetism. *Physics of the Earth and Planetary Interiors*, **10**: 327–335.

Cross-references

Crustal Magnetic Field
Harmonics, Spherical
Magnetic Anomalies, Long Wavelength
Main Field Modeling